

学位論文

**Radio Properties of
Broad Absorption Line Quasars**
(広い高速吸収線を示すクエーサーの電波性質)

平成25年12月 博士（理学）申請

東京大学大学院理学系研究科

天文学専攻

林 隆之

Abstract

Quasars with absorption troughs of broad resonance line at rest ultraviolet are called broad absorption line (BAL) quasars. Because of its blue-shifted high velocity of $\sim 0.1c$, an absorber of BAL is considered to be wind from an accretion disk. Recently, it has been extensively discussed that the disk wind plays a major role in regulating cosmological coevolution of galaxies and supermassive black holes. To establish the picture of the coevolution, understanding of BAL quasars is crucial. Now, $\sim 10\text{--}30\%$ of quasars in the Sloan Digital Sky Survey (SDSS) possess BAL, suggesting that it is one of general properties found in quasars. However, despite its importance and generality, a basic question of BAL quasars has still remained; what does the observed fraction suggest?

To account for the BAL fraction, several hypotheses have been proposed. The most widely discussed one is an orientation scheme. There, the disk wind is possessed by all quasars, and detection of BAL depends on inclination of the sources. Previous studies suggested that the orientation effect should play a role in BAL phenomena at least in part. In contrast, there are also radio properties incompatible with the orientation scheme. Therefore, the orientation effect is considered to work together with another factor. One of the candidates is an evolution scheme which ascribes the BAL fraction to duration of time when quasars possess the disk wind, and where BAL is observed in a relatively early phase before quasars' emergence from a thick shroud.

At present, in spite of the above arguments, bases for each hypothesis are still not solid. Furthermore, another hypothesis alternative to the evolution scenario is also possible. To give insight into the interpretation of the BAL fraction, in this thesis we investigated radio morphology and spectrum of BAL quasars from milli-arcsecond (mas) to arcsecond scales. First, because relativistic non-thermal jet detected at radio is affected by Doppler beaming effect, observed quantity at radio include information about viewing angles for the sources.

Thus, radio observations are powerful means to validate the evidence for the orientation scheme. Second, radio morphology and spectrum represent the source environment. Utilizing this, we can test the evolution scheme. Finally, because both the jet and disk wind are driven by the disk, explorations of the jet at radio can also make a contribution to test an intrinsic difference in the central engines between BAL and non-BAL quasars.

Chapter 3 deals with radio morphology and spectrum of a BAL quasar, J1159+0112, at mas-scale resolution. The source shows gigahertz peaked spectrum (GPS) which is a typical characteristic of compact radio sources affected by strong absorption. However, such a source can also be contaminated by blazars in a flaring state. To discriminate the genuine GPS sources from the blazars, we made observations with very long baseline interferometry. As a result, the source shows a two-sided structure across ~ 1 kpc and no significant polarization in its central component. These properties are typical of the genuine GPS sources. We revealed that the genuine GPS sources can be associated with BAL quasars. This can be a basis for testing the evolution scheme presented in the following chapter. In addition, we give a constraint on the inclination of the source, which is in agreement with prediction by the orientation scheme.

Following the findings of the genuine GPS source, in Chapter 4 we performed survey observations of BAL and non-BAL quasars at 322 MHz. Based on the evolution scheme, BAL quasars are expected to reside in a dense environment and thus suffer from strong absorption at the low frequency. Actually, previous radio observations with arcsecond-scale resolution suggested many peaked spectral sources are associated with BAL quasars. As confirmed in Chapter 3, actually BAL quasars can host the genuine GPS sources. With this observation, we found a large number of the sources affected by absorption that is inferred from highly inverted spectral index. However, a statistical test did not present evidence for the stronger absorption of BAL quasars than non-BAL quasars. Thus, galactic-scale environment is comparable between the two quasar subgroups. This is contrary evidence of the confinement of BAL quasars and then the evolution scheme.

In Chapter 5, arcsecond-scale radio morphology of BAL quasars is investigated using FR II quasars catalog constructed for this study. First, we confirmed that BAL quasars with large-sized FR II morphology are 2–3 times less common than those without the FR II morphology. This suggests incompleteness of the simple orientation scheme. Next, we made statistical comparisons of physical parameters between BAL and non-BAL quasars in the sample. Here, no significant difference is found in bent and asymmetry of the sources, suggesting the two subgroup of quasars live in a similar environment. This supports invalidity of the evolution scheme. Moreover, the distributions of projected linear size and lobe luminosity are indistinguishable. Therefore, BAL quasars can be similarly active in non-

BAL quasars in terms of strength and period of the radio activity. Because the emergence of such an activity is less common in BAL quasars, duty cycle of BAL quasars could be distinct from non-BAL quasars. Although further confirmation is required, difference in the black hole mass and/or Eddington ratio could control the phenomena.

In summary, as suggested by previous studies, the orientation effect can play a role in the BAL phenomena but is not complete. On another front, we found counter-evidence for the evolution scheme which is the similar low-frequency absorption and asymmetry between the two quasars subgroup. One of the considerable origin alternative to the evolution scheme is an intrinsic difference in the central engines. The observed BAL fraction could be explained by a combination of the orientation and the intrinsic difference.

Acknowledgement

First of all, I have to give my great thanks to Dr. Akihiro Doi and Dr. Hiroshi Nagai. Dr. Akihiro Doi suggested dealing with such an attractive issue, that is radio-loud BAL quasars. It is not just my pleasure but great honor to work under him. Also, I owed my ph.D. life to Dr. Hiroshi Nagai. His mentorship has improved my thought. It is very generous of them to spend much time to make discussions with me. Spectral analysis of SDSS data in the thesis is made by Dr. Hiroaki Sameshima. Without his contribution, I could not perform statistical analysis in Chapter 5. Many thanks for Prof. Hideyuki Kobayashi, my supervisor, who approved my application to research at the Mizusawa VLBI Observatory from my undergraduate experiment to the end.

I would like to thank colleagues in National Astronomical Observatory of Japan (NAOJ), and The University of Tokyo. There, I have improved myself by learning from excellent graduate students. In particular, Dr. Kazuhiro Hada, Dr. Shoko Koyama, and Kazunori Akiyama working on non-thermal emissions with VLBI are stimulating for me. Sometimes advice from staff at Mizusawa VLBI Observatory, NAOJ help me resolving technical issues. Especially I give my acknowledge to Dr. Katsunori Shibata, Dr. Mareki Honma, and Dr. Yoshiaki Hagiwara. It was a pleasure for me to make discussions about accretion disks with Dr. Ken Ohsuga, Mariko Nomura and members of a black hole seminar at Division of Theoretical Astronomy, NAOJ.

I would also like to express my gratitude to overseas friends; Dr. G. Bruni, Dr. K.-H. Mack, Dr. F. M. Montenegro-Montes at National Institute for Astrophysics (Bologna, Italy) and Dr. Magdalena Kunert-Bajraszewska, Dr. Marcin P. Gawroński at Torun Center for Astronomy (Torun, Poland). During stay at Bologna and Torun, I discovered that global interaction plays a role in advance of science. This could be one the most important things that I have learned during my ph.D. As far as I know, radio study of BAL quasar is not

so popular in astronomy because of difficulty in studying such high- z sources. Despite this situation, it is pleasant for me to meet many friends in the world.

Finally, I give my acknowledge to people in Tetsuryoku-kai, Keio Chutobu Junior High School, and Chuo University Senior High School. Receptive attitude of the colleagues is of help for my ph.D. Furthermore, teaching science to and having a talk with the students (and of course salary obtained by the lecture) are continuous sources of motivation for my research.

In this thesis, I utilized the data obtained with GMRT, VLA, and VLBA. I thank the staff of the GMRT that made our observations possible. GMRT is run by the National Centre for Radio Astrophysics of the Tata Institute of Fundamental Research. The VLBA is a facility of NRAO, operated by Associated University Inc. under cooperative agreement with the National Science Foundation (NSF). This research has made use of the VLA polarization monitoring program as well as data from the University of Michigan Radio Astronomy Observatory. The latter has been supported by the University of Michigan and by a series of grants from the NSF, most recently AST-0607523. This work was partially supported by a Grant-in-Aid for Scientific Research (C; 21540250, A. D., and B; 24340042, A. D.) from the Japanese Ministry of Education, Culture, Sports, Science and Technology.

Contents

1	Introduction to the Thesis	1
2	Review	5
2.1	The Unified Model of Active Galactic Nuclei	5
2.2	Radio Sources Associated with AGN	7
2.3	Broad Absorption Line Quasars	9
2.4	Radio Studies of BAL Quasars	11
3	Multi-frequency VLBI Imaging of a BAL Quasar J1159+0112	15
3.1	Introduction	15
3.2	Target	16
3.3	VLBI Observations	17
3.3.1	VLBA Polarimetric Observations at 1.7, 4.9, and 8.3 GHz	17
3.3.2	Global-VLBI Observations at 2.3 GHz	18
3.3.3	VLBA Observations at 15.4 and 23.8 GHz	18
3.4	Data Reduction	19
3.4.1	<i>A priori</i> Calibration and Imaging Process	19
3.4.2	Calibration of Polarization	19
3.5	Result	21
3.5.1	Morphology	21
3.5.2	Polarization	21
3.5.3	Flux Variability	24
3.6	Discussion	24
3.6.1	Viewing Angle and Advancing Speed of Jets	24
3.6.2	Constraints on the AGN Wind	25
3.6.3	Classification of Radio Sources	26
3.6.4	Interpretations of the Radio Morphology	26
3.7	Conclusions	28

4	Low-frequency Survey Observations of BAL quasars	29
4.1	Introduction	29
4.2	Target Selection	30
4.3	GMRT Observations	35
4.4	Data Reduction	35
4.5	Result	38
4.5.1	Flux Density	38
4.5.2	Spectral Index	38
4.6	Discussion	43
4.6.1	Absorption at the Low Frequency	43
4.6.2	Relation of the Absorption to the Evolution Scheme	44
4.6.3	Suggestion for the Orientation Scheme	45
4.6.4	Source with Optically Thin Emission	45
4.7	Conclusions	46
5	Rarity of BAL Quasars with Large-sized FR II Morphology	47
5.1	Introduction	47
5.2	Sample Selection	49
5.2.1	Identification of FR II Quasars	49
5.2.2	Identification of BAL Quasars	51
5.3	Result	51
5.3.1	Fraction of BAL quasars	51
5.3.2	Radio Properties of FR II–BAL Quasars	56
5.3.3	Optical Properties of FR II–BAL Quasars	59
5.4	Discussion	60
5.4.1	How Rare are FR II–BAL Quasars?	60
5.4.2	The Origin of the Rarity of FR II–BAL Quasars	62
5.5	Conclusions	70
6	Conclusions	71
6.1	Summaries	71
6.2	Future Prospects	74
	Appendix A Radio-interferometer Polarimetry	77
A.1	Stokes Parameters	77
A.2	Stokes Parameters and Visibilities	79
A.3	<i>D</i> -term Approximation	79
	Appendix B FR II quasars catalog	81
	Appendix C Radio Properties and Definition of BAL	95
C.1	Definition of BAL	95
C.2	Radio Morphology and Definition of BAL	95
	References	99
	Correspondence	105

List of Figures

2.1	A schematic picture of the unified scheme of AGN.	6
2.2	An image of a typical extra-galactic radio source associated with AGN.	8
2.3	The anticorrelation between the peak frequency and projected linear size of GPS/CSS sources.	9
2.4	A result of numerical simulation of an accretion disk with the line-driven wind.	10
2.5	A schematic diagram of the disk wind model of BAL quasars.	12
2.6	A result of spectropolarimetric observation of the C IV region for PHL 5200 and its interpretation.	13
2.7	An infra-red color-color diagram of quasars and mergers.	14
3.1	Electric vector position angle of the calibrator sources.	20
3.2	The VLBA images of J1159+0112 at 1.7, 2.3, 4.9, and 8.3 GHz.	22
3.3	The VLBA images of J1159+0112 at 15.4 and 23.8 GHz.	23
3.4	Spectral energy distribution of J1159+0112.	24
3.5	Schematic picture of positional relationship between disk wind and jet.	25
3.6	Constraints on viewing angles and bulk velocity of jet.	26
4.1	The 1.4-GHz images of BAL quasars resolved by the FIRST survey.	32
4.2	The 1.4-GHz images of non-BAL quasars resolved by the FIRST survey.	32
4.3	Result of the Monte-Carlo simulation to determine the sample size.	35
4.4	The properties of BAL and non-BAL sample.	36
4.5	Flux density distribution at 1.4 GHz from the FIRST and NVSS.	37
4.6	Typical u - v coverages of the observations.	37
4.7	Flux densities distribution of our targets at 1.4 GHz and 322 MHz.	38
4.8	Radio spectra of the BAL sample.	39
4.8	Radio spectra of the BAL sample (<i>continued</i>).	40
4.9	The 322-MHz images of the sources resolved by GMRT.	41
4.10	The 322-MHz image of the source unresolved by GMRT but resolved by the FIRST survey.	41
4.11	Spectral index between 1.4 GHz and 322 MHz as a function of 1.4-GHz flux density.	42

4.12	Distributions of spectral index between 1.4 GHz and 322 MHz.	42
4.13	A Kaplan-Meier survival curve of the spectral index between 1.4 GHz and 322 MHz.	43
4.14	Comparison of the obtained spectral index with previous high-frequency study.	44
5.1	Distribution of lobe opening angles and diameter of FR2 quasar candidates.	50
5.2	SDSS spectra and FIRST images of the FR II BAL quasars.	52
5.2	SDSS spectra and FIRST images of the FR II BAL quasars (<i>continued</i>).	53
5.2	SDSS spectra and FIRST images of the FR II BAL quasars (<i>continued</i>).	54
5.2	SDSS spectra and FIRST images of the FR II BAL quasars (<i>continued</i>).	55
5.3	Projected linear size, opening angle, and lobe luminosity distributions of the FR II sample.	60
5.4	Definition of component's name and corresponding geometry under the ideal condition.	61
5.5	Arm-length and flux density ratios distributions of the FR II sample.	62
5.6	Bolometric luminosity, black hole mass, and Eddington ratio distributions of the FR II sample.	63
5.7	Schematic picture of the geometry assumed for the orientation scheme.	66
5.8	Expected angular distribution of the FR II sample and the rarity of FR II BAL quasars.	67
5.9	Expected projected linear size distribution of the FR II sample.	68
5.10	Arm-length and flux-density ratio distribution of FR II quasars.	68
A.1	Oscillating plane of the electric vector.	78
B.1	1.4-GHz FIRST images of FR II quasars.	81
B.1	1.4-GHz FIRST images of FR II quasars (<i>continued</i>).	82
B.1	1.4-GHz FIRST images of FR II quasars (<i>continued</i>).	83
B.1	1.4-GHz FIRST images of FR II quasars (<i>continued</i>).	84
B.1	1.4-GHz FIRST images of FR II quasars (<i>continued</i>).	85
B.1	1.4-GHz FIRST images of FR II quasars (<i>continued</i>).	86
B.1	1.4-GHz FIRST images of FR II quasars (<i>continued</i>).	87
B.1	1.4-GHz FIRST images of FR II quasars (<i>continued</i>).	88
B.1	1.4-GHz FIRST images of FR II quasars (<i>continued</i>).	89
B.2	1.4-GHz FIRST images of non-FR II quasars excluded by visual inspection.	89

List of Tables

3.1	Basic Parameters of J1159+0112.	17
3.2	Observation Summary.	18
3.3	Flux densities of each component.	23
3.4	Polarization properties of the component D.	23
4.1	The BAL Quasar Sample.	33
4.2	The non-BAL Quasar Sample.	34
5.1	Optical Properties of FR II–BAL Quasars.	57
5.2	Radio Properties of FR II–BAL Quasars.	58
5.3	Fraction of BAL quasars from SDSS DR7.	59
5.4	Result of Statistical Comparison in the FR II Sample.	64
B.1	Radio Properties of FR II Quasars.	90
B.1	Radio Properties of FR II Quasars.	91
B.1	Radio Properties of FR II Quasars.	92
B.1	Radio Properties of FR II Quasars.	93
B.1	Radio Properties of FR II Quasars.	94
C.1	Fraction of BAL quasars in SDSS DR7.	96
C.2	Fraction of BAL quasars in SDSS DR6.	97
C.3	Fraction of BAL quasars in SDSS DR5.	97
C.4	Fraction of BAL quasars in SDSS DR3.	97

Introduction to the Thesis | 1

Quasars with absorption troughs of broad resonance line at rest ultraviolet are called broad absorption line (BAL) quasars. Because of its blue-shifted high velocity of $\sim 0.1c$, an absorber of BAL is considered to be active galactic nucleus (AGN) wind from an accretion disk. Recently, it has been extensively discussed that the disk wind plays a major role in regulating cosmological coevolution of galaxies and supermassive black holes (e.g. Ciotti et al., 2009). To establish the picture of the coevolution, understanding of BAL quasars is crucial. Now, $\sim 10\text{--}30\%$ of quasars in the Sloan Digital Sky Survey (SDSS; York et al., 2000) possess BAL (Trump et al., 2006; Scaringi et al., 2009; Gibson et al., 2009), suggesting that it is one of general properties found in quasars. However, despite its importance and generality, a basic question of BAL quasars has still remained; what does the observed fraction suggest?

To answer the above fundamental question, several hypotheses have been proposed. The most widely discussed one is an orientation scheme (e.g., Goodrich & Miller, 1995; Cohen et al., 1995). There, all quasars possess the disk wind and detection of BAL is attributed to viewing angles for the sources (Elvis, 2000). To test this scenario, one of direct ways is radio observation that aims for relativistic non-thermal jet. Because the non-thermal jet is affected by Doppler beaming effect, its observable variables include information about inclination of the sources (Blandford & Konigl, 1979; Urry & Padovani, 1995). For instance, lower flux density and steeper spectral index of BAL quasars are consistent with the relatively edge-on viewing (Shankar et al., 2008; DiPompeo et al., 2011). Combined with results from numerical simulation which demonstrate collimated disk wind (Proga et al., 1998, 2000; Nomura et al., 2013), the orientation effect should play a role in BAL phenomena at least in part.

In contrast to the preceding argument, there are also radio properties incompatible with the orientation scheme. If BAL quasars are edge-on viewed AGN, they are expected to show

larger projected linear size than non-BAL quasars. However, compact radio sources are more often associated with BAL quasars (Becker et al., 2000; Gregg et al., 2006; Shankar et al., 2008). In addition, Zhou et al. (2006) and Ghosh & Punsly (2007) found a number of BAL quasars showing rapid radio-flux variation which indicates the Doppler beaming effect on pole-on viewed jets (Blandford & Konigl, 1979; Urry & Padovani, 1995). Therefore, at the moment, the orientation effect is considered to work together with another factor. One of the candidates is an evolution scheme. There, BAL might be observed in a relatively early phase before its emergence from a thick shroud (Briggs et al., 1984; Voit et al., 1993; Reichard et al., 2003; Lípari & Terlevich, 2006). Non-thermal jet in BAL quasars might be frustrated by the dense environment (Becker et al., 2000; Gregg et al., 2006). Multi-frequency radio observations with arcsecond-scale resolution have suggested this picture. BAL quasars host compact radio sources showing peaked spectrum with frequency (Montenegro-Montes et al., 2008a), which are candidates for the frustrated objects embedded in a dense environment (van Breugel et al., 1984; O’Dea et al., 1991). Thus far, radio studies have made a great contribution to support the evolution scheme.

Despite the above considerations, bases for the evolution scheme are still not established firmly. First, the peaked spectral sources found by Montenegro-Montes et al. (2008a) could not be compact objects suffering from strong absorption, but it might be flaring blazars. Second, because most of previous works devoted to the study in the gigahertz regime (Montenegro-Montes et al., 2008a; DiPompeo et al., 2011; Bruni et al., 2012), the low-frequency absorption has not been understood well and also the comparison with non-BAL quasars is not enough. Moreover, the absorbed compact objects are not necessarily frustrated sources. They can also be young radio sources which are progenitors of intergalactic scale radio sources (Phillips & Mutel, 1982; O’Dea & Baum, 1997). Thus, the evolution scenario where BAL quasars are enclosed by the thick shroud might not be true. Alternative hypothesis could present.

In this thesis, we will focus on radio morphology and spectrum of BAL quasars from milli-arcsecond (mas) to arcsecond angular scales. Investigation of these radio properties presents clues to diagnosing the evolution scheme. At the same time, test for the orientation scheme is also provided. The outline of the thesis is as follows:

- In Chapter 2, we will give a brief overview of the field; general review of AGN, non-thermal radio sources, and BAL quasars.
- In Chapter 3, we investigate radio morphology and spectrum of a BAL quasar with mas scale resolution (Hayashi et al., 2013). The target, J1159+0112, shows peaked spectrum at GHz frequency, but its origin has not been well-understood. Multi-frequency polarimetric imaging observations identify the source classification; whether the source

is a compact object affected by strong absorption or a flaring state of blazars. This can be a basis for test of the evolution scheme presented in the following chapter. In addition, the high-resolution observations also provide direct measurement of the source inclination. This also would be a test for the orientation scheme.

- In Chapter 4, we present radio spectrum of BAL quasars with arcsecond-scale resolution which obtained by GMRT survey observations at 322 MHz. This is the first systematic survey observations at the low frequency. In the evolution scheme, BAL quasars are considered to live in a dense environment where strong absorption is expected. A comparison of spectral index between BAL and non-BAL quasars at the frequency can test the difference in the absorption and then the evolution scheme.
- Chapter 5 deals with morphological study of BAL quasars with arcsecond-scale resolution. Utilizing SDSS, we constructed a catalog of quasars with large-sized radio sources. We estimated a frequency of appearance of BAL feature in the sample, which has been one of the foundations of the evolution scheme but still has an large ambiguity. In addition, statistical properties of the BAL quasars are provided for the first time. Those give us a clue to the origin of the compactness of BAL quasars. There, implication of an alternative hypothesis to the evolution scenario will be presented.
- Finally, conclusions of the thesis and future perspectives of the field are given in Chapter 6. Discussion focused on the interpretation of the BAL fraction is summarized there.

Throughout this thesis, sign of spectral index, α , is defined by $\alpha = \Delta \ln S_\nu / \Delta \ln \nu$, where S_ν is flux density at frequency, ν .

2.1 The Unified Model of Active Galactic Nuclei

Active galactic nuclei (AGN) show energetic phenomena in the central region of galaxies. The two largest classes of AGN are Seyfert galaxies and quasars whose classification is based on absolute B magnitude, M_B : sources with $M_B < -23$ are quasars, otherwise Seyfert galaxies. Luminosity of AGN is not explained by radiation from stars but is originated in gravitational potential. A massive object fueled by accretion processes is supposed to be in the center, whose existence has been demonstrated by kinematics of gas (e.g., high-velocity rotating water vapor masers; Miyoshi et al. 1995, and reverberation mapping of broad emission lines; Blandford & McKee 1982; Korista et al. 1995). Furthermore, such a massive object is considered to be a super-massive black hole. Recently, an experiment to aim direct detection of the black hole in Galaxy has been conducted with sub-mm very long baseline interferometry (VLBI). The compact object in the center is presumed (Doeleman et al., 2008).

A theoretical model to release gravitational energy from accreting matter is an accretion disk. There are several disk models. In a standard model introduced by Shakura & Sunyaev (1973), energy of the particles are dissipated locally and converted to the radiation by viscous torque. This standard disk is geometrically thin but optically thick. In case of the standard disk, therefore, the radiation is approximated by multi-temperature blackbody radiation. On another front, in case of high accretion rate, the disk becomes geometrically thick by radiation pressure. This kind of disk is called slim disk (Abramowicz et al., 1988). In contrast, radiatively inefficient accretion flow model (RIAF; Ichimaru, 1977; Narayan & Yi, 1994) is valid if accretion rate is low. In this case, because of low density, the disk becomes optically thin and thus non-thermal emission arises. Additionally, pressure of the non-

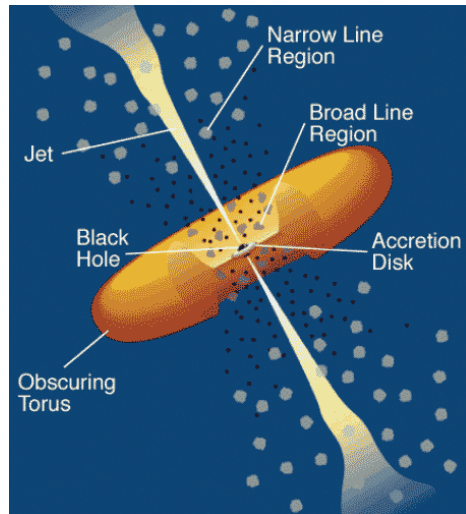


Figure 2.1 A schematic picture of the unified scheme of AGN from Urry & Padovani (1995). Broad line region obscured by a dust torus cannot be observed when we observe the source from its edge-on view.

thermal gas makes the disk geometrically thick. In summary, state of the disk is controlled by accretion rate, whose numerical demonstration was given by Ohsuga et al. (2009).

Each AGN group is further classified in several subclasses. The two major subclasses are type-I and type-II AGN. The latter has permitted and forbidden lines in their spectrum whose line widths are typically $< 1,000 \text{ km s}^{-1}$ (narrow emission lines). The former exhibits permitted lines with widths of $> 1,000 \text{ km s}^{-1}$ (broad emission lines) and the same characteristics with type-II AGN (Antonucci, 1993). At first, these two types of AGN were thought to be intrinsically different type of sources. However, when we conducted a spectropolarimetry to a type-II Seyfert galaxy, the broad-line features emerged in its polarization spectrum (e.g., NGC 1068 in Antonucci & Miller, 1985). Broad line emitter could be obscured by a dust torus, and the detection of the polarized emission line is considered to be ascribed to scattering effect. Figure 2.1 shows a schematic picture of the model (Urry & Padovani, 1995), where type-I and type-II AGN are considered to be intrinsically identical sources. There, unpolarized broad lines emerge when we observe the sources from face-on view. Thus far, such an attempt to construct the unified model of AGN has been made by many authors. Most of differences in AGN are in general thought to be originated in viewing angles for the sources (Antonucci, 1993). Intrinsic differences between different AGN subgroups could be less than observed.

In contrast to the above argument, a fundamental difference other than the inclination of the sources also could exist. For example, one of the distinctions is found in radio loudness that is ratio of flux density at radio frequency to that at optical wavelength. K -corrected

radio loudness is defined by

$$R^* = \frac{f_{5\text{GHz}}}{f_{5000\text{\AA}}}, \quad (2.1)$$

where $f_{5\text{GHz}}$ and $f_{5000\text{\AA}}$ are flux densities at 5 GHz and 5000 Å (rest frame), respectively (Sramek & Weedman, 1980). Conventionally, sources with $\log R^* \gtrsim 1$ are classified as radio-loud sources, otherwise radio-quiet sources (e.g., Stocke et al., 1992). Approximately 10% of the sources are radio-loud. Here, radio emission from AGN is originated in synchrotron radiation from non-thermal plasma. In many cases, the emission comes from collimated jet with relativistic velocity (see Figure 2.1). Some part of the difference in the radio loudness is explained by Doppler beaming effect (Blandford & Konigl, 1979) that depends on inclination of the jet axis with respect to the line of sight. In contrast, there is also an intrinsic distinction; some AGN do not have radio emission intrinsically.

2.2 Radio Sources Associated with AGN

Collimated jet emanating from the central engine forms one of the most grand-scale structures in the universe. Figure 2.2 shows a radio image of a typical extra-galactic radio source, Cygnus A. At each end of the sources there are symmetrical extended lobes, in which a bright hot spot is found. The lobes and the hot spots are connected with a core by collimated jets. Here, the core is supposed to be a base of the jet where the central engine is contained. Through the jet, energy is carried from the core to the hot spots and lobes (Blandford & Rees, 1974; Scheuer, 1974). Now, linear size of the sources is known to become several megaparsec (Mpc) at most (e.g., Machalski et al., 2008). These inter-galactic scale sources whose linear size is more than ~ 15 kpc are called large symmetric objects (LSOs; Readhead 1995). In contrast, there are also galactic scale sources whose morphology resembles that of the large-sized ones. These sources are called compact symmetrical objects (CSOs) or medium symmetric objects (MSOs) whose boundary is linear size of ~ 1 kpc (Wilkinson et al., 1994; Fanti et al., 1995).

CSOs and MSOs have been considered to be progenitors of LSOs (Phillips & Mutel, 1982; Carvalho, 1985; Fanti et al., 1995; Readhead et al., 1996). In this respect, CSOs and MSOs are "young radio sources" (O'Dea et al., 1991; Snellen et al., 2000). One of the evidence for this picture of the evolution is found in its radio spectrum. In most cases, CSOs show gigahertz-peaked spectrum (GPS; Gopal-Krishna et al. 1983; Spoelstra et al. 1985), whose turnover is found at $\gtrsim 500$ MHz. On the other hand MSOs are included in a category of compact steep spectrum (CSS; Fanti et al. 1985) sources having its spectral peak at $\lesssim 500$ MHz (following the definition in O'Dea, 1998). Synchrotron self-absorption and free-free absorption are possible origins of the low-frequency cutoff, where both absorption have been observationally confirmed in different sources; for examples Orienti & Dallacasa

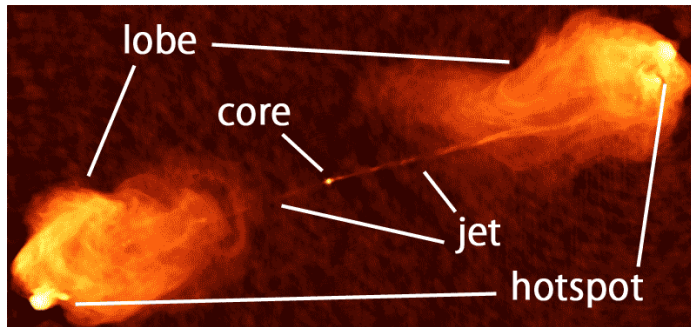


Figure 2.2 An image of a typical extra-galactic radio source associated with AGN, Cygnus A, from NRAO/AUI. Linear size of the source is ~ 100 kpc.

(2008) for the former, and Kamenno et al. (2000, 2003) for the latter. Now, as shown in Figure 2.3, there is an anticorrelation between the linear size and turnover frequency (Fanti et al., 1990; O’Dea & Baum, 1997). This relation suggests that properties of GPS/CSS sources are contiguous, and that an object is decrease its peak frequency with increasing linear size. Then, the evolution model based on synchrotron self-absorption (Begelman, 1996; Snellen et al., 2000) or free-free absorption (Bicknell et al., 1997) was proposed. In the model, the evolution track of ”CSOs (with GPS) \rightarrow MSOs (with CSS) \rightarrow LSOs” is suggested. The evolution is finally validated by measurements of the source age; spectral age obtained with multi-frequency observations (Carilli et al., 1991; Murgia et al., 1999) and kinematic age obtained by measuring proper motion of the lobes (Tzioumis et al., 1989; Conway, 2002; Gugliucci et al., 2005), where consistency between these two measurements was confirmed by Nagai et al. (2006).

Now, most of CSOs are not considered to evolve to LSOs. Based on the flux-density limited sample in Readhead et al. (1996), $\sim 10\%$ of objects are CSOs whose linear size is less than ~ 1 kpc. Considering that lobe advance speed of $0.01\text{--}0.1c$ does not change with the linear size ranged in $1\text{ pc--}1\text{ Mpc}$ (Kawakatu et al., 2008), it can be said that the universe is overpopulated by the compact sources (O’Dea et al., 1991; O’Dea & Baum, 1997). To account for the overpopulation, recurrent jet activity is considered (Reynolds & Begelman, 1997). There, most of the CSOs would terminate its jet activity during the course of the evolution (e.g., Parma et al., 2007; Orienti et al., 2010). During a lifetime of the AGN, several sequences of the jet activities can happen (Reynolds & Begelman, 1997; Conway, 2002). The most distinguished example is a so called ”double-double radio galaxy” which exhibits a pair of double-lobed radio sources, having a coinciding radio core and aligned in a line (Schoenmakers et al., 2000; Konar et al., 2006; Marecki et al., 2006).

In contrast to the above discussions, the compact sources suffering from strong absorption are also considered to be frustrated sources confined by the ambient medium (van

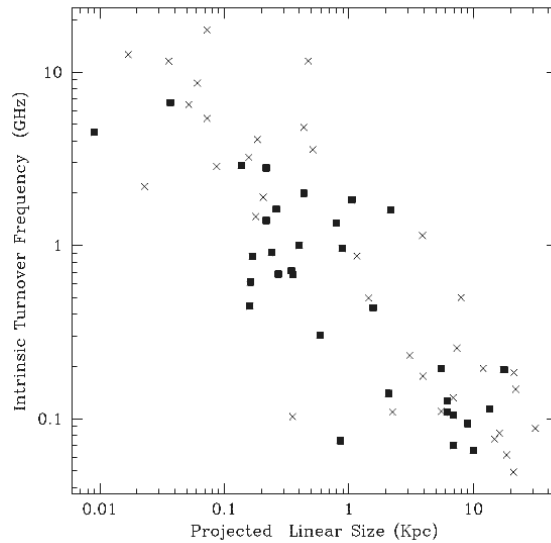


Figure 2.3 The anticorrelation between the peak frequency at rest and projected linear size of GPS/CSS sources obtained from O’Dea (1998). Quasars and galaxies are indicated by crosses and filled squares, respectively. An object is considered to evolve from the top left (small-sized source peaked at high-frequency) to the bottom right (large-sized source peaked at low frequency).

Breugel et al., 1984; O’Dea et al., 1991). These sources are thought to live in a dense environment and cannot evolve to large-sized one.

2.3 Broad Absorption Line Quasars

Quasars showing broad absorption troughs of resonance lines in their rest ultraviolet spectra are called broad absorption line (BAL) quasars (e.g., Weymann et al., 1991). The first known BAL quasar is PHL 5200 (Lynds, 1967). At first, because of difficulty in identifying BAL before widespread use of objective-prism spectroscopy, very few examples of BAL quasars were found (Peterson, 1997), but in step with the advances in technology the number of the samples has increased. Most great contribution is a result from Sloan Digital Sky Survey (SDSS; York et al. 2000). A large number of spectroscopic data allowed us to find a significant number of BAL quasars (Reichard et al., 2003).

Conventionally, BAL is identified with balnicity index (BI; Weymann et al. 1991) defined as

$$BI = \int_{3000}^{25000} \left[1 - \frac{f(v)}{0.9} \right] C(v) dv, \quad (2.2)$$

where $f(v)$ is normalized flux density at blue-shifted Doppler velocity, v , in units of km s^{-1} referenced to the rest frame. The variable $C(v)$ has $C(v) = 1$ whenever contiguous troughs of $f(v) < 0.9$ exist among the minimum width of 2000 km s^{-1} and otherwise $C(v) = 0$. Here, the trough with $BI > 0$ is defined as BAL. Another metric is also proposed. Hall et al.

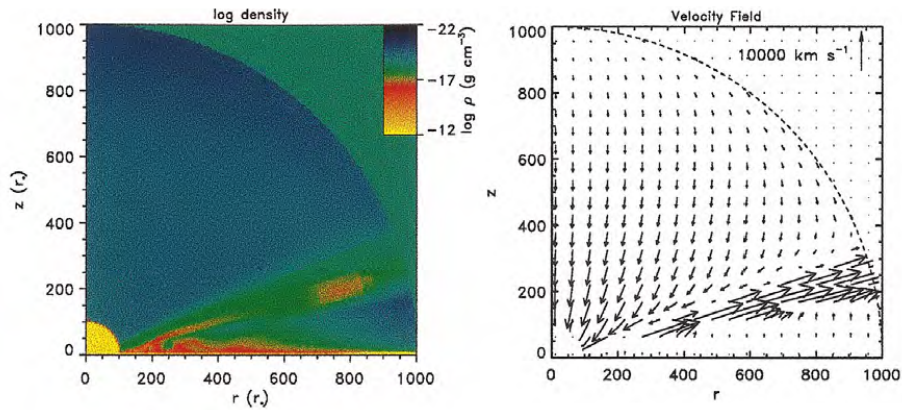


Figure 2.4 A result of numerical simulation of an accretion disk in Proga et al. (2000). The left and right maps exhibit density and velocity field, respectively. High-velocity wind nearly parallel to the disk is confirmed at each panel.

(2002) introduced absorption index (AI) which is later modified by Trump et al. (2006). The definition is

$$\text{AI} = \int_0^{29000} \left[1 - f(v)\right] C'(v) dv, \quad (2.3)$$

where the variable $C'(v)$ has $C'(v) = 1$ whenever contiguous troughs of $f(v) < 0.9$ exist among the minimum width of 1000 km s^{-1} and otherwise $C'(v) = 0$. By definition, AI is less strict criterion than BI to judge whether absorption trough is BAL or not. In addition, Gibson et al. (2009) introduced modified balnicity index, BI_0 , defined as

$$\text{BI}_0 = \int_0^{25000} \left[1 - \frac{f(v)}{0.9}\right] C(v) dv, \quad (2.4)$$

which is stricter than AI but less strict than BI. We note that all of these metric are not based on the physics but just a phenomenological one.

BAL quasars are classified into two categories, HiBAL and LoBAL quasars, depending on whether they show both high-ionization (e.g., C IV, Si IV, N V, and, P V) and low-ionization troughs (e.g., Mg II, Fe II, and Al III), or only low-ionization troughs. Now, to account for its high velocities (several thousands km s^{-1} to $\sim 0.1c$ typically), ionized wind from an accretion disk accelerated by radiation pressure in lines (line-driven wind; Drew & Boksenberg, 1984; Shlosman et al., 1985; Vitello & Shlosman, 1988) is the most plausible candidate for the absorber of BAL. Observationally, luminosity dependence of the maximum velocity of BAL features (Laor & Brandt, 2002; Ganguly et al., 2007) supports the picture of the line-driven wind, where no high-velocity absorption was found in quasars with low luminosity at near ultraviolet. Later, the wind was analytically designed by Murray et al. (1995), and as shown in Figure 2.4 numerically demonstrated by Proga et al. (1998, 2000).

Recently, it has been extensively discussed that AGN feedback plays a major role in regulating the cosmological coevolution of galaxies and super-massive black holes (e.g. Ciotti et al., 2009). AGN are expected to suppress star formation of the host galaxies by its radiation and outflow. Otherwise, a galaxy luminosity function with a sharper high-mass cutoff cannot be explained (Croton et al., 2006). Also a correlation between bulge and black hole mass, so called "the Magorrian relation" (Magorrian et al., 1998), is considered to be originated in the AGN feedback (e.g., King, 2003). Now, the disk wind provides a significant amount of kinematic energy to the host galaxies (at most a few percent of the bolometric luminosity of quasars; e.g., Borguet et al., 2013). Therefore, to establish the picture of the coevolution, understanding of BAL quasars is crucial.

Fraction of quasars showing BAL is estimated as $\sim 10\text{--}30\%$ in SDSS (Trump et al., 2006; Gibson et al., 2009; Scaringi et al., 2009; Allen et al., 2011; Shen et al., 2011) whose scattering comes from the difference in the definitions. Thus, BAL is a common feature widely shown in quasars. However, despite the importance and the generality of BAL, the basic question has still not been solved: What does the fraction suggest? To answer this question, two main scenarios have been proposed; an orientation scheme and an evolution scheme.

In the orientation scheme, all quasars possess the disk wind and whether or not BAL is observed can be attributed to viewing angles for the sources. The disk wind is produced by radiation pressure nearly parallel to the disk (Elvis, 2000), based on support in optical spectropolarimetry (Goodrich & Miller, 1995; Cohen et al., 1995, also see Figure 2.6). A schematic diagram is given in Figure 2.5. In the model, BAL troughs can only be seen in quasars whose edge-on disk wind points towards the observer. On the other hand, the evolution scheme ascribes the ratio of BAL to non-BAL quasars to the duration of time when quasars possess the disk wind (Becker et al., 2000). There, BAL quasars are in a relatively early phase before its emergence from a thick shroud. L ipari & Terlevich (2006) found that, on a color-color diagram at infra red, BAL quasars are positioned between the power-law and blackbody regions as shown in Figure 2.7. These sources could be in a transitional phase from merger-produced star-burst galaxies to quasars (Voit et al., 1993).

2.4 Radio Studies of BAL Quasars

Radio studies of BAL quasars are quite meaningful. First, because non-thermal jet is affected by Doppler beaming effect, observable variables of the jet include information about viewing angles for the sources (Blandford & Konigl, 1979; Urry & Padovani, 1995). Thus, radio observations are powerful means to validate the evidence for the orientation scheme. Second, radio morphology and spectrum represent the source environment (Blanton et al., 2000, 2001; Dallacasa et al., 2013). Utilizing this, we can test the evolution scheme. Finally,

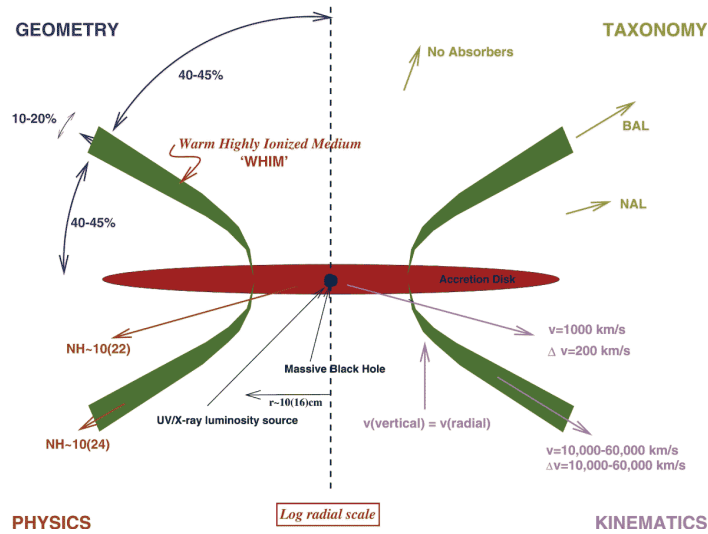


Figure 2.5 A schematic diagram of the disk wind model of BAL quasars from Elvis (2000). In the model, BAL troughs can only be seen in quasars whose edge-on disk wind points towards the observer.

because both non-thermal jet and disk wind are driven by the central engine, explorations of the jet at radio can provide an information about the state of the accretion disk having the wind. From this point of view, radio studies can make a contribution to test the intrinsic differences between BAL and non-BAL quasars.

At the dawn of the field, BAL quasars were only found in radio-quiet sources. Therefore, the BAL phenomenon was, at the time, thought to be a key to understand the difference between radio-loud and radio-quiet quasars (Stocke et al., 1992). However, in step with enhancement of wide-field survey programs, the cognizance has changed. The first radio-loud BAL quasars were found by Becker et al. (1997). The sources are targets of the FIRST Bright Quasar Survey (Gregg et al., 1996) which aims optical counterparts of the radio sources detected by the Faint Images of the Radio Sky at Twenty centimeters survey (FIRST survey; Becker et al. 1995). In the now, BAL quasars are known to be radio-loud in about the same way as non-BAL quasars. The fraction of BAL quasars in the FIRST detected sample is similar to that not detected (e.g., Shankar et al., 2008). Becker et al. (2000, 2001) reported a large number of moderately radio-loud BAL quasars. Because most of the BAL quasars show point-like structure and inverted spectrum at arcsecond scale, they argued against the orientation scheme and suggested the evolution scheme; the compact source might be frustrated by the dense medium that obscures the BAL quasars. This was supported by a multi-frequency observation. Montenegro-Montes et al. (2008a) reported that the compact BAL quasars in Becker et al. (2000, 2001) show radio spectrum as found in gigahertz-peaked spectrum (GPS) or compact steep spectrum (CSS) radio sources that are candidates for compact radio sources suffering from strong absorption.

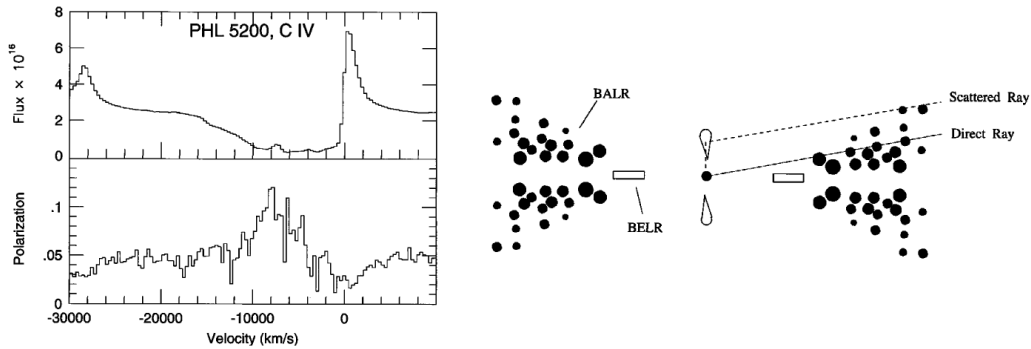


Figure 2.6 (left) A result of spectropolarimetric observation of the C IV region for PHL 5200 from Cohen et al. (1995). Total flux density and degree of linear polarization are shown on the top and bottom, respectively. At the absorbed region, high degree of polarization is confirmed. (right) Interpretation of the polarization properties. The diagram is also taken from Cohen et al. (1995). In case of edge-on view, the scattered ray is farther from the equatorial plane than is the direct one. Hence, the direct ray is more absorbed than is the scattered one.

Further investigations at radio were developed by grace of SDSS. Thus far, utilizing SDSS statistical studies with a larger sample have been made by many authors. Gregg et al. (2006) presented a morphological study of BAL quasars. They found that the number of Fanaroff-Riley type-II (FR II; Fanaroff & Riley 1974) radio sources in BAL quasars is roughly ten times less common than that in the total SDSS sample. Quasars might show their BAL when they are young before they have large-scale jets. Moreover, Zhou et al. (2006) and Ghosh & Punjly (2007) found a number of BAL quasars showing rapid radio-flux variation which indicates the Doppler beaming effect on pole-on viewed jets (Blandford & Konigl, 1979; Urry & Padovani, 1995). All of the results are inconsistent with the edge-on view of BAL quasars. Thus, the simple orientation scheme was considered to be unreasonable and the evolution scheme was preferred there.

In contrast to the above argument, the evolution scheme is not a panacea for explaining the entire radio phenomena of BAL quasars. Although Montenegro-Montes et al. (2008a) found the peaked spectra in BAL quasars, a comparison with non-BAL quasars was not carried out there. Bruni et al. (2012) who performed the comparison suggested that the fractions of GPS/CSS sources are indistinguishable between BAL and non-BAL quasars. Thus, the basis for the evolution scheme is still not solid. Moreover, statistically BAL quasars show a steeper radio spectrum than non-BAL quasars (DiPompeo et al., 2011; Bruni et al., 2012). The difference could not be derived from absorption or spectral aging, but an effect of the viewing angles is a strong candidate (DiPompeo et al., 2011). In addition, Shankar et al. (2008) mentioned that dependence of the BAL quasars fraction on radio luminosity can be explained by the edge-on viewing angles of the sources. Thus, the orientation scheme of BAL quasars also can be valid. Consequently, the orientation effect

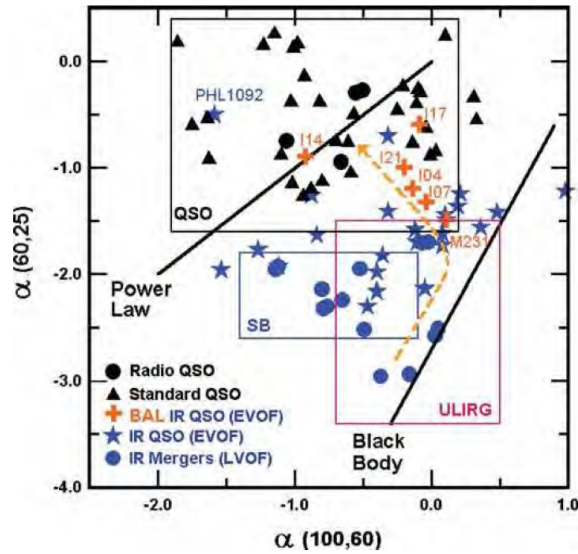


Figure 2.7 An infra-red color-color diagram of quasars and merging galaxies from Lıpari & Terlevich (2006). The dashed line depicts a probable evolutionary path described in Lıpari & Terlevich (2006): from mergers to quasars. BAL quasars are found in the transition area between the blackbody and power-law regions.

is, at present, considered to work together with another factor.

There have been also several studies of BAL quasars using VLBI (Jiang & Wang, 2003; Montenegro-Montes et al., 2008b; Liu et al., 2008; Doi et al., 2009; Reynolds et al., 2009; Kunert-Bajraszewska et al., 2010; Gawronski & Kunert-Bajraszewska, 2011; Yang et al., 2012; Bruni et al., 2013). Because of its high angular resolution, VLBI observations can measure the inclination of the jet axis with respect to the line of sight directly on the basis of the Doppler-beaming framework. The first systematic survey was made by Doi et al. (2009). They suggested non-thermal jets and the disk wind coexist simultaneously at least in radio-loud BAL quasars. Furthermore, there are some inverted-spectrum sources which are interpreted as young radio sources or Doppler-beamed sources having pole-on-viewed relativistic jet. The evolution scheme was inferred there. Imaging observations which present morphology of the sources were also provided by various authors. Both one-sided and two-sided jet structures have been found (Jiang & Wang, 2003; Montenegro-Montes et al., 2008b). In addition, a polarization study was conducted by Liu et al. (2008) who reported no difference in radio morphologies and polarization features between flat- and steep-spectrum sources. Thus far, only two sources were observed at more than three frequencies. These two sources show signatures of interaction with the interstellar medium (ISM). Kunert-Bajraszewska et al. (2010) reported disturbed morphology of J1048+3457. Reynolds et al. (2009) discussed ram pressure of the external medium on the Mrk 231 radio source. Despite these studies, general milli-arcsecond (mas) scale radio properties of BAL quasars are still unclear from the point of view of the orientation and evolution schemes.

Multi-frequency VLBI Imaging of a BAL Quasar J1159+0112

3

3.1 Introduction

In the orientation scheme of BAL quasars, BAL troughs can only be seen in quasars whose edge-on disk wind points towards the observer (Elvis, 2000). However, Zhou et al. (2006) found a number of radio-detected BAL quasars showing rapid radio-flux variation which indicates the Doppler beaming effect on pole-on viewed jets (Blandford & Konigl, 1979; Urry & Padovani, 1995). Widely distributed radio spectral indices of BAL quasars (Becker et al., 2000; Montenegro-Montes et al., 2008a; Doi et al., 2009; Fine et al., 2011; DiPompeo et al., 2011; Bruni et al., 2012) also suggest at least a portion of BAL quasars are blazar-type objects with a flat-spectrum radio core. Therefore, the simple orientation scheme might not explain entire BAL phenomena. To explain such properties incompatible with the orientation scheme, the evolution scheme has been proposed, where quasars show BAL before they emerge from merger-produced ultraluminous infrared galaxies (Voit et al., 1993). Because most BAL quasars detected by the FIRST survey are point-like sources, Becker et al. (2000) suggested that they are small, frustrated or young sources, similar to CSS sources. This picture is supported by multi-frequency radio observation made by Montenegro-Montes et al. (2008a). They found a large number of BAL quasars that show radio spectrum as found in GPS/CSS sources. Thus, the radio emission of BAL quasars could be frustrated to small scales by the ambient medium (Becker et al., 2000). Here, radio observations to find the evidence of the confinement is an important approach for understanding BAL quasars in terms of the evolution scheme.

In contrast to the above argument, genuine GPS/CSS sources which are young or frustrated radio sources dominated by symmetrical lobes are sometimes indistinguishable from blazars by radio observations with arcsecond scale resolution. While the genuine GPS/CSS

sources have an optically thin steep spectrum in the gigahertz regime, usually blazars have a flat or inverted spectrum up to high frequencies. However, during a flare blazars may show a convex spectrum similar to the genuine GPS sources (Torniainen et al., 2005, 2007). Thus, observations with limited frequency coverage cannot distinguish the genuine GPS/CSS sources from blazars. Even in these situations, blazars and the genuine GPS/CSS sources still display characteristics different from each other (Tinti et al., 2005; Orienti et al., 2007). Blazars appear as one-sided structures in mas resolutions, long-term variability (Torniainen et al., 2005, 2007; Hovatta et al., 2007, 2008), and a high degree of polarization. On the other hand, the genuine GPS/CSS sources have lobes with sub-relativistic speeds, which appear as two-sided structures in mas resolution, little variability, and little polarization. To distinguish blazars and the genuine GPS/CSS sources, high-resolution direct imaging is important. Therefore, observations with VLBI are efficient to test the evolution scheme. In addition, VLBI is also one of the most direct ways to test the orientation scheme because radio structures on mas scale include the information about the inclination of the sources.

Thus far, only two BAL quasars have been observed with VLBI at more than three frequencies (Reynolds et al., 2009; Kunert-Bajraszewska et al., 2010). Despite the importance of VLBI studies, general milli-arcsecond (mas) scale radio properties of BAL quasars are still unclear from the point of view of the orientation and evolution schemes.

In this chapter, we will report the result of multi-frequency polarimetric imaging observations using VLBI for a radio-loud BAL quasar, J1159+0112, which shows GPS on sub-arcsecond scale. We describe our sample in Section 3.2. The observation and data reduction are described in Sections 3.3 and 3.4, respectively. The results are presented in Section 3.5. We discuss the structures of parsec-scale radio jets and the disk wind, the orientation scheme, and the evolution scheme in Section 3.6. Finally, our conclusions are summarized in Section 3.7. Based on a cosmology consistent with WMAP results of $h = 0.71$, $\Omega_M = 0.27$, and $\Omega_\Lambda = 0.75$ (Spergel et al., 2003), the angular scale of 1 mas corresponds to 8.4 pc at distance of the target at $z \sim 2$.

■ 3.2 Target

We selected a sample for the VLBI observations from 20 sources detected in the first systematic VLBI observation at 8.4 GHz (Doi et al., 2009) using the Optically Connected Array for VLBI Exploration project (OCTAVE; Kawaguchi 2008) operated by the Japanese VLBI Network (JVN; Fujisawa 2008). The OCTAVE sample consisted of the BAL quasars in Trump et al. (2006) from the third data release (DR3; Abazajian et al. 2005) of Sloan Digital Sky Survey (SDSS; York et al., 2000) which hosted radio counterparts in the FIRST survey with peak flux densities of more than 100 mJy. We selected target sources that have (i) flux density of more than 100 mJy in the OCTAVE observation, (ii) expected polarized

Table 3.1. Basic Parameters of J1159+0112.

Parameters	Value	Reference
Object name	J1159+0112	
R.A. (J2000) from SDSS DR3	11 59 44.82	Abazajian et al. (2005)
DEC. (J2000) from SDSS DR3	+01 12 06.9	Abazajian et al. (2005)
R.A. (J2000) from the FIRST survey	11 59 44.832	Becker et al. (1995)
DEC. (J2000) from the FIRST survey	+01 12 06.87	Becker et al. (1995)
Redshift, z	2.000	Trump et al. (2006)
BAL classification	Hi	Trump et al. (2006)
Absorption index, AI (km s^{-1})	2887	Trump et al. (2006)
Balnicity index, BI (km s^{-1})	0	Trump et al. (2006)
FIRST 1.4-GHz peak flux density, $I_{1.4\text{GHz}}$ (mJy beam^{-1})	267	Becker et al. (1995)
FIRST 1.4-GHz integrated flux density, $S_{1.4\text{GHz}}$ (mJy)	268.5 ± 8.1	Becker et al. (1995)
NVSS 1.4-GHz integrated flux density, $S_{1.4\text{GHz}}$ (mJy)	275.6 ± 8.3	Condon et al. (1998)
Radio loudness, $\log R_*$	2.6	Doi et al. (2009)
Spectral index between 1.4 and 8.4 GHz	-0.3	Doi et al. (2009)
1.4-GHz radio luminosity ^a , $L_{1.4\text{GHz}}^{\text{FIRST}}$ ($\text{erg s}^{-1}\text{Hz}^{-1}$)	6.4×10^{33}	

^aAssuming spectral index of $\alpha = -0.7$

flux density^a of more than 1 mJy, and (iii) flat or inverted spectra ($\alpha > -0.5$) in Doi et al. (2009). There are four sources which satisfy the above criteria. In addition, we set condition that the source is also appeared in BAL quasars catalog constructed by (Gibson et al., 2009). This is because the catalog presented by Trump et al. (2006) could contain "overestimated BAL" (Ganguly et al., 2007; Knigge et al., 2008) which will be discussed in Appendix C. As a result, we selected J1159+0112. The basic information of the target is listed in Table 3.1. Montenegro-Montes et al. (2008a) reported radio spectrum of the source is similar to that found in GPS sources. For result of the rest of the three sources, please see Hayashi et al. (2013).

3.3 VLBI Observations

3.3.1 VLBA Polarimetric Observations at 1.7, 4.9, and 8.3 GHz

The multi-frequency polarimetric imaging was conducted at 1.7, 4.9, and 8.3 GHz using Very Long Baseline Array (VLBA) on 2010 June 25 (project code BD137). The observation was carried out over 10 hours. The source was observed at the three bands with 6–8 minutes scan at 3 different hour angles. This leads to the quasi-similar u - v coverages at each band. An aggregate bit rate of 128 Mbps was used; each band consisted of two 8-MHz wide, full-

^aExpected polarized flux density is defined as a product of degree of polarization provided by the NRAO VLA Sky Survey at 1.4 GHz (NVSS; Condon et al. 1998) and flux density obtained by the OCTAVE observation at 8.4 GHz.

Table 3.2. Observation Summary.

Frequency (GHz)	Bandwidth (MHz)	Polarization	Date	Antenna	Integration time (min)
1.7	16	RR, LL, RL, LR	2010 Jun. 25	VLBA ^a	23
2.3	64	RR	2011 Mar. 15	VLBA ^b , Effersberg, Medicina, Onsala, Yebes	5
	64	RR	2011 Mar. 16	VLBA ^c , Effersberg, Medicina, Onsala	10
4.9	16	RR, LL, RL, LR	2010 Jun. 25	VLBA	23
8.3	16	RR, LL, RL, LR	2010 Jun. 25	VLBA	23
15.4	128	LL	2013 Jan. 31	VLBA	47
23.8	128	LL	2013 Jan. 31	VLBA	24

^aLack of Hancock station due to radio frequency interference.

^bOnly Hancock, North Liverty, and Saint Croix stations are available. Lack of the others due to elevation limit.

^cLack of Mauna Kea station due to elevation limit.

polarization intermediate frequencies (IFs) centered at 1.663 and 1.671 GHz at 1.7-GHz band, 4.644 and 5.095 GHz at 5-GHz band, and 8.111 and 8.580 GHz at 8-GHz band. We integrated two IFs in each band to make Stokes I maps, while we produced the polarization map of each IF separately.

■ 3.3.2 Global-VLBI Observations at 2.3 GHz

The global-VLBI imaging was conducted at 2.3- and 8.4-GHz band on 2013 March 15 and 16 (project code GE034). Telescopes joined to the observations are listed in Table 3.2. The observations were originally made for use of providing a link between the radio celestial reference frame with a future one based on GAIA observations. The observing runs including J1159+0112 were carried out over 19 hours each. In total, J1159+0112 was observed at the two frequency simultaneously with 5 minutes scan at 3 different hour angles. This leads to the same u - v coverages at each frequency. An aggregate bit rate of 512 Mbps was used; each band consisted of four 8-MHz wide IFs with both RR and LL polarization. In this study, we only used the data at 2.3 GHz.

■ 3.3.3 VLBA Observations at 15.4 and 23.8 GHz

The multi-frequency imaging was conducted at 15.4 and 23.8 GHz using VLBA on 2013 January 31 (project code BH190). The observation was carried out over 3 hours. The source was observed at the two bands to lead to the quasi-similar u - v coverages. An aggregate bit rate of 512 Mbps was used at each band. eight 16-MHz wide IFs was used for LL polarization.

■ 3.4 Data Reduction

■ 3.4.1 *A priori* Calibration and Imaging Process

Data reduction was performed with a standard procedure using the Astronomical Image Processing System (AIPS; Greisen 2003) software developed at the National Radio Astronomy Observatory (NRAO). Amplitude calibration was performed using the measurements of system noise temperature during the observation and gains provided by each station. We also corrected the amplitude attenuation due to atmospheric opacity. Fringe fitting was performed after the Earth orientation parameters and ionospheric dispersive delay were corrected. Finally, bandpass calibration for both amplitude and phase was performed. As for the VLBA observations, the source was detected on all baselines at all frequencies except for the 1.7-GHz band at Hancock station where system temperature was not obtained properly due to radio frequency interference. As for the global-VLBI observation, we lacked some stations due to elevation limit (see Table 3.2).

Imaging processes were performed using the `difmap` software (Shepherd, 1997). As for the 2.3-GHz data, we combined all of the visibilities with `DBCON` in the AIPS before the imaging processes. We conducted self-calibration to derive the antenna-based amplitude corrections. The `difmap` does not solve for gain time variation for RR and LL visibilities separately. Hence, as for polarization observations made at 1.7, 4.9, and 8.3-GHz band, we constructed RR or LL model by the `difmap` and then performed self-calibration for Stokes I by the AIPS, which corrects gain time variation for RR and LL visibilities separately (Aaron, 1997). The error on the absolute flux density scale was generally $\sim 5\%$.

■ 3.4.2 Calibration of Polarization

As for polarization observations made at 1.7-, 5-, and 8-GHz bands, we corrected RL and LR delay offsets using the bright polarized source, J0854+2006 (OJ 287), and corrected instrumental polarization (D -term) using the compact unpolarized source, J1407+2827 (OQ 208). After D -term was calibrated, we confirmed that OQ 208 had almost become unpolarized. We estimated the error on the absolute flux density scale for polarization was within 10% including residual D -term.

An unknown phase offset between L and R polarizations for a reference antenna was corrected using the observed electric vector position angle (EVPA) of J1310+3220 which was observed by EVLA at 5- and 8-GHz bands on 2010 July 15 and June 22, respectively, under the project named TPOL. Each band consists of two 128-MHz wide IFs centered at 4.896 and 5.024 GHz at 5-GHz band, 8.395 and 8.523 GHz at 8-GHz band. Using the data obtained by UMRAO^b, we confirmed that during the months of June and July there was

^bThe data was obtained by the University of Michigan Radio Astronomy Observatory (UMRAO), which

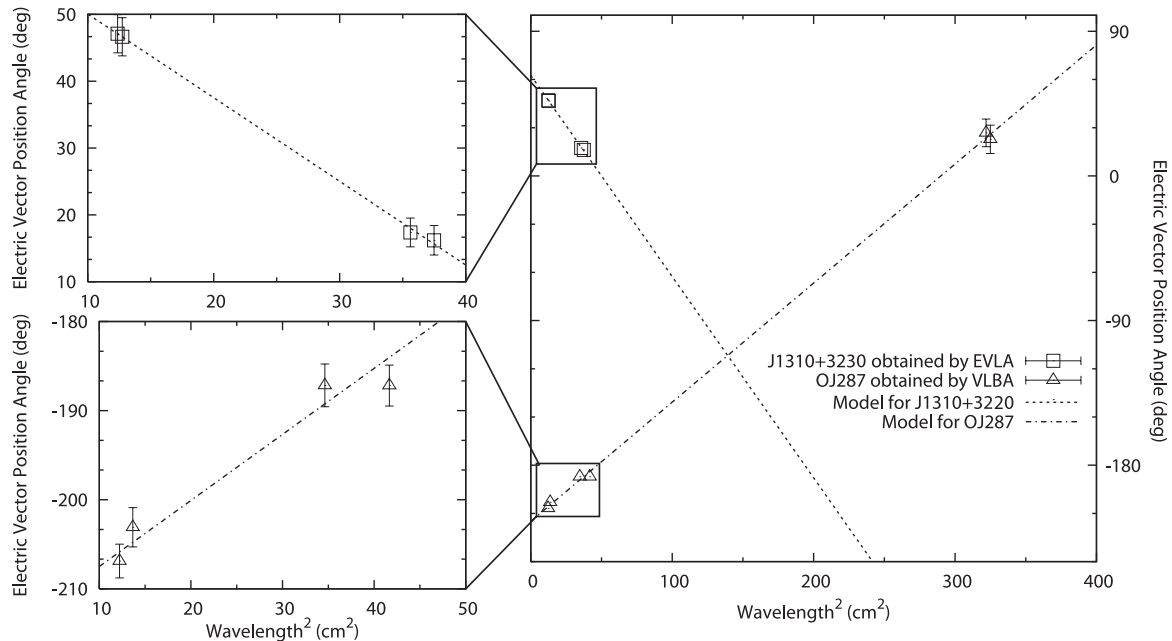


Figure 3.1 EVPA for polarization calibrator sources of J1310+3220 obtained by EVLA observation and OJ 287 obtained by our VLBA observation. We refer to EVPA of J1310+3220 (open squares) for that of OJ 287 (open triangles) and target sources. Reference value at 1.7 GHz is obtained by extrapolation of the value of 5 and 8 GHz (dotted line). EVPA of OJ 287 at 1.7 GHz is in excellent agreement with EVPA of OJ 287 extrapolated from 5 and 8 GHz (dot-dashed line).

no significant variability in their total flux densities, degree of polarization, and EVPA. In addition, total and polarized flux density of J1310+3220 obtained by VLBA were similar to that obtained by EVLA. We derived the integrated EVPA for J1310+3220 at 1.7-GHz band by extrapolating from EVPA at 5- and 8-GHz bands because EVPA would be affected by RM. After the EVPA correction, EVPA of the other EVPA calibrator, OJ 287, at 1.7-GHz band was consistent with that extrapolated from EVPA at 5- and 8-GHz bands obtained using VLBA (Figure 3.1). Hence, our EVPA calibrations seemed to be performed well.

The errors of EVPA are the root sum square of flux density measurement errors and fitting error to derive RM for the calibrator source. Because polarimetry at low frequency is affected by ionospheric Faraday rotation, we checked the total electron content of the ionosphere during our observation; the typical variation of ionospheric RM within a scan was $|\text{RM}_{\text{obs}}| < 0.5 \text{ rad m}^{-2}$ and between scans was $|\text{RM}_{\text{obs}}| < 3 \text{ rad m}^{-2}$. These values are equivalent to $\Delta\text{EVPA} < 0.02 \text{ rad}$ and $\Delta\text{EVPA} < 0.12 \text{ rad}$ at a wavelength of 20 cm, which do not affect the estimation of the EVPA significantly even at 1.7-GHz band.

was kindly provided by M. Aller.

■ 3.5 Result

■ 3.5.1 Morphology

Stokes I maps of the target at 1.7, 2.3, 4.9, and 8.3 GHz are shown in Figures 3.2. The images at 1.7, 2.3, and 4.9 GHz show the linear alignment of several discrete components that extend ~ 90 mas towards the southeast and a significant counter feature ~ 50 mas northwest across ~ 1 kpc in total (Figure 3.2). Flux densities of each component were measured by fitting with a Gaussian model profile (Table 3.3). The southeast components are consistent with the previous study by Montenegro-Montes et al. (2008b). They show steep spectra (Table 3.3) and thus morphology that can be classified as a two-sided structure. Although Montenegro-Montes et al. (2008b) also reported two symmetrical extensions close to the core located towards the northwest and the southeast, no such structure was detected by our observation.

Stokes I maps of the target at 15.3 and 22.8 GHz are shown in Figure 3.3. We detected the component A at the frequencies. The component was resolved into two components a1 and a2. Flux densities of each component were measured by fitting with a Gaussian model profile (Table 3.3). Figure 3.3 also shows spectral index map between the two frequencies. Registration of the maps is based on the position of the peak of flux density. Spectral index decreases towards the south east. Now, we also found sub components in the component A both at 4.9 and 8.3 GHz. However, the separation between these components (~ 1 mas) is not consistent with that between the components a1 and a2 (~ 0.5 mas). The components found at 4.9 and 8.3 GHz could not be resolved completely.

The radio spectrum of J1159+0112 (Figure 3.4) can be represented by double-peaked spectra, peaked at a few hundred MHz and ~ 10 GHz: a steep spectrum and an flat/inverted spectrum in the range of our VLBA observations. The GHz-peaked component originates in the radio core (the component A), while the steep spectrum components originate in the extended structure with several discrete blobs (the components B–E). The interpretation of the spectrum along with the morphology will be discussed in Section 3.6.4

■ 3.5.2 Polarization

Figures 3.2 also shows polarization vectors overlaid on the Stokes I maps. Polarized flux densities and degree of polarization at each component averaged within a band is listed in Table 3.4. Errors are the root sum square of calibration uncertainties of 10% and fitting error in the AIPS task IMFIT. EVPA at components whose polarized flux densities are detected is shown in Table 3.4. Polarization was detected in the component D with a very high degree of polarization of $11.8 \pm 1.4\%$ at 1.7 GHz but not at 5 and 8 GHz This will be discussed in Section 3.6.4.

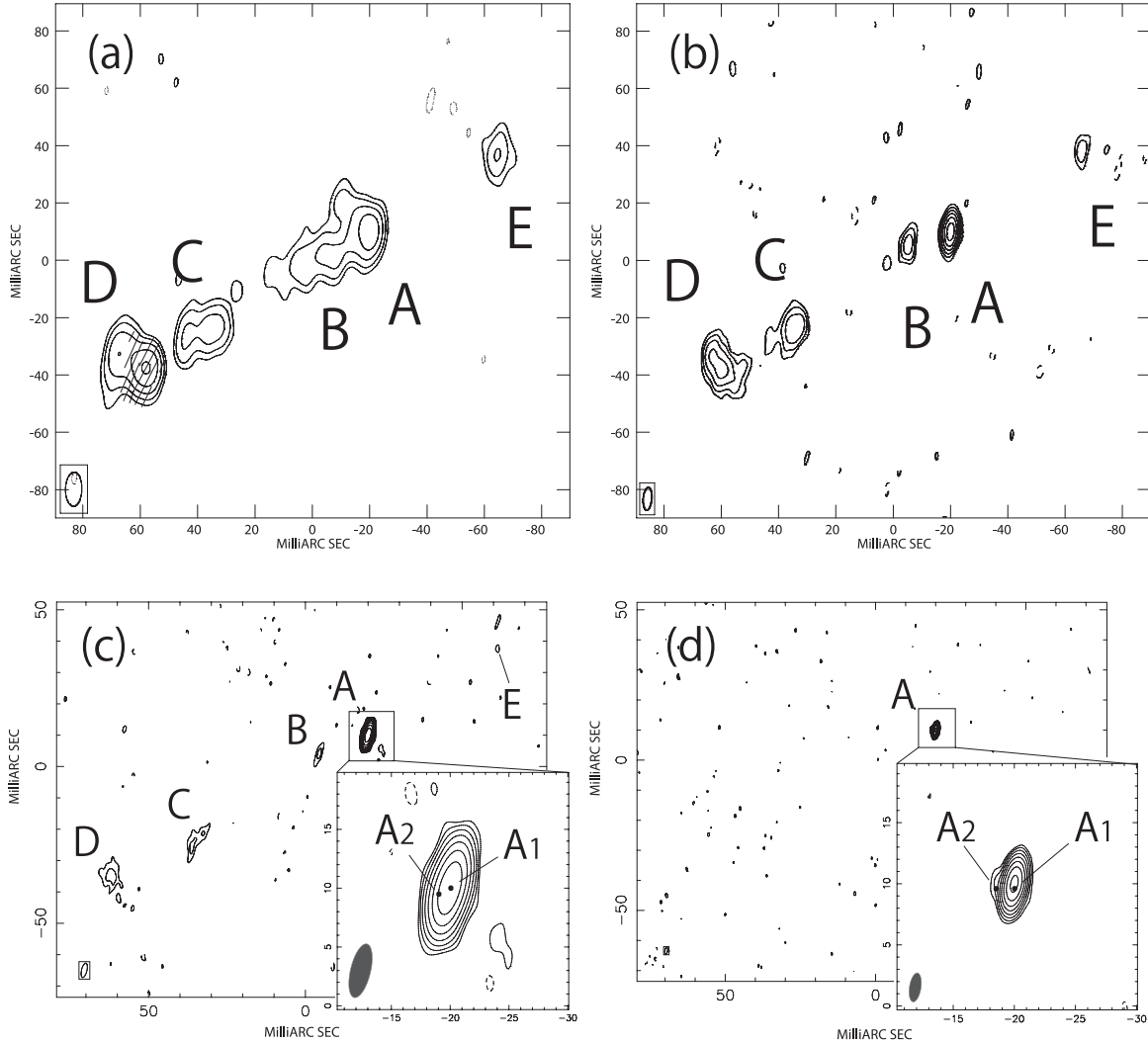


Figure 3.2 Natural weighted VLBA images of J1159+0112 observed on 2010 June 25 (a, c, d), and 2011 March 11 and 15 (b). (a) The 1.7-GHz Stokes I map with superposed polarization vectors. The restoring beam is 12×5.7 mas at $\text{PA} = -1.4^\circ$, the contour levels are $(-1, 1, 2, 4, 8, \dots) \times 1.86 \text{ mJy beam}^{-1}$, and the peak flux density is $32.1 \text{ mJy beam}^{-1}$. Vector lengths are proportional to the polarized flux density (1 mas corresponds to $0.3 \text{ mJy beam}^{-1}$). (b) The 2.3-GHz RR map. The restoring beam is 8.0×2.9 mas at $\text{PA} = -4.6^\circ$, the contour levels are $(-1, 1, 2, 4, 8, \dots) \times 1.2 \text{ mJy beam}^{-1}$, and the peak flux density is $57.7 \text{ mJy beam}^{-1}$. (c) The 4.9-GHz Stokes I map. The restoring beam is 4.7×1.7 mas at $\text{PA} = -14^\circ$, the contour levels are $(-1, 1, 2, 4, 8, \dots) \times 0.78 \text{ mJy beam}^{-1}$, and the peak flux density is $93.0 \text{ mJy beam}^{-1}$. (d) The 8.3-GHz Stokes I map. The restoring beam is 2.4×0.95 mas at $\text{PA} = -8.9^\circ$, the contour levels are $(-1, 1, 2, 4, 8, \dots) \times 0.76 \text{ mJy beam}^{-1}$, and the peak flux density is $122 \text{ mJy beam}^{-1}$.

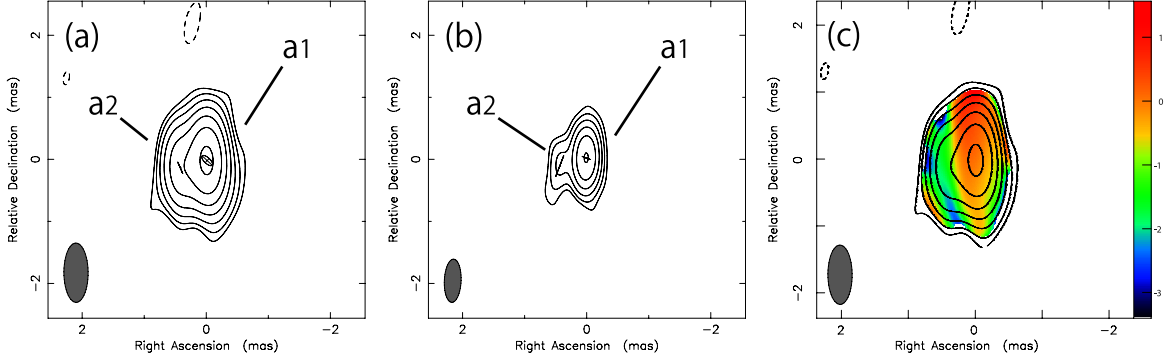


Figure 3.3 Uniform weighted VLBA images of J1159+0112 observed on 2013 January 31. (a) The 15.4-GHz LL map. The restoring beam is 0.96×0.39 mas at $PA = 2.7^\circ$, the contour levels are $(-1, 1, 2, 4, 8, \dots) \times 1.2$ mJy beam $^{-1}$, and the peak flux density is 90.7 mJy beam $^{-1}$. Model components are also illustrated. (b) The 23.8-GHz LL map. The restoring beam is 0.70×0.27 mas at $PA = -2.5^\circ$, the contour levels are $(-1, 1, 2, 4, 8, \dots) \times 2.7$ mJy beam $^{-1}$, and the peak flux density is 87.3 mJy beam $^{-1}$. Model components are also illustrated. (c) Spectral index map created with 15.4-GHz map and 23.8-GHz map restored by the beam size at 15.4 GHz. The contour represents the 15.4-GHz LL map, whose levels are same as that in (a).

Table 3.3. Flux densities of each component.

Component	1.7 GHz (mJy)	2.3 GHz (mJy)	4.9 GHz (mJy)	8.3 GHz (mJy)	15.4 GHz (mJy)	23.8 GHz (mJy)
A	34.3 ± 1.8	63.2 ± 6.3	99.9 ± 4.7^a	135.6 ± 6.7^b	130.6 ± 10.4	110.7 ± 9.9
a1	99.3 ± 9.9	97.2 ± 9.8
a2	31.3 ± 3.2	13.5 ± 1.6
B	53.2 ± 3.8	12.1 ± 1.3	2.1 ± 0.4	< 0.8	< 1.2	< 2.7
C	30.0 ± 1.6	27.2 ± 2.6^c	7.5 ± 0.5	< 0.8	< 1.2	< 2.7
D	76.8 ± 3.4^d	49.4 ± 5.0	16.2 ± 0.9	< 0.8	< 1.2	< 2.7
E	14.2 ± 0.9	6.2 ± 0.7	0.9 ± 0.4	< 0.8	< 1.2	< 2.7

^aThough the components are resolved into two components, A1 and A2, which are 94.2 ± 4.7 mJy and 5.1 ± 0.4 mJy, it is not clear that they are identical to the components a1 and a2 found at 15.4 and 22.8 GHz.

^bThough the components are resolved into two components, A1 and A2, which are 134.1 ± 6.7 mJy and 1.5 ± 0.4 mJy, it is not clear that they are identical to the components a1 and a2 found at 15.4 and 22.8 GHz.

^cThe components are resolved into two components, which are 24.3 ± 2.5 mJy and 2.9 ± 0.5 mJy.

^dThe components are resolved into two components, which are 64.4 ± 3.3 mJy and 12.4 ± 0.9 mJy.

Table 3.4. Polarization properties of the component D.

Parameters	1.7 GHz	4.9 GHz	8.3 GHz
Polarization Flux density (mJy)	7.6 ± 0.8	< 1.2	< 1.1
Degree of polarization (%)	11.8 ± 1.4	< 7.4	...
Electric vector position angle (deg.)	152 ± 9

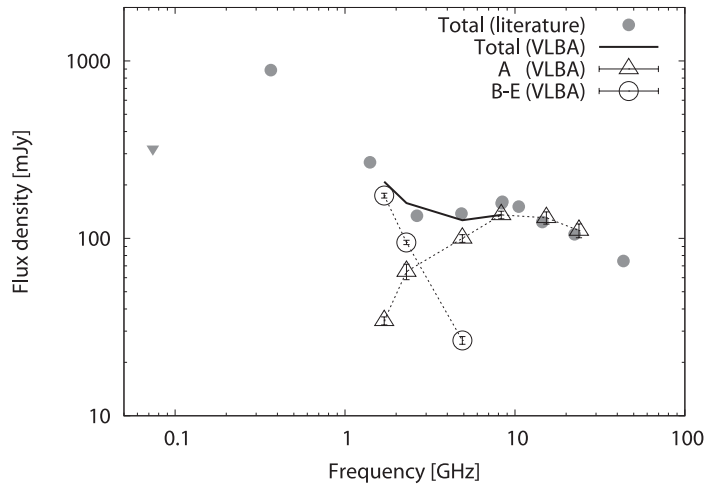


Figure 3.4 Radio spectrum of J1159+0112. Flux density obtained by literatures (filled gray circle; Becker et al. 1995; Douglas et al. 1996; Montenegro-Montes et al. 2008a), and our observation using VLBA are shown. Error bars of the data points from the literature are smaller than the symbol size. A triangle means 3σ upper limit at 74 MHz (Cohen et al., 2007). Flux density obtained by our observation is decomposed into that of the radio core (open triangle; the component A) and jets (open circle; the components B–E). Dashed and thick lines link the data points from our observation.

3.5.3 Flux Variability

We examined the flux variability. We utilized significance of variability by defining $\Delta S = |S_1 - S_2|$ and $\sigma_{\text{var}} = (\sigma_1^2 + \sigma_2^2)^{1/2}$, where S_i and σ_i are total flux density and its uncertainty of i -th epoch data, respectively. Usually the value more than 3 is regarded as significant variability (e.g., Zhou et al., 2006; Ghosh & Punjly, 2007). Between the FIRST survey and NVSS, we obtained $\Delta S/\sigma_{\text{var}} = 0.6$ which suggests no significant variability for J1159+0112. Here, errors were estimated to be 3% in total flux density for VLA observation at 20 cm (Condon et al., 1998). However, two-epoch observations are not enough to conclude that the sources are stable.

3.6 Discussion

3.6.1 Viewing Angle and Advancing Speed of Jets

Assuming an intrinsic symmetry of the jets, the apparent asymmetry of radio morphology with respect to the central engine results from the Doppler beaming effect. The ratio of flux densities of the approaching to receding components, R_F , is related to intrinsic jet velocity, β , and viewing angle, θ , by $R_F = [(1 + \beta \cos \theta)/(1 - \beta \cos \theta)]^{3-\alpha}$ (Blandford & Konigl, 1979; Urry & Padovani, 1995). We obtain $\beta \cos \theta \sim 0.2$ for J1159+0112. As a result, the constraints on β and θ are $0.2 < \beta < 1$ and $\theta < 77$ deg, respectively (Figure 3.6).

Alternatively, we can also obtain $\beta \cos \theta$ based on a arm-length ratio of the approaching to receding components, given by $R_D = (1 + \beta \cos \theta)/(1 - \beta \cos \theta)$. The apparent separation

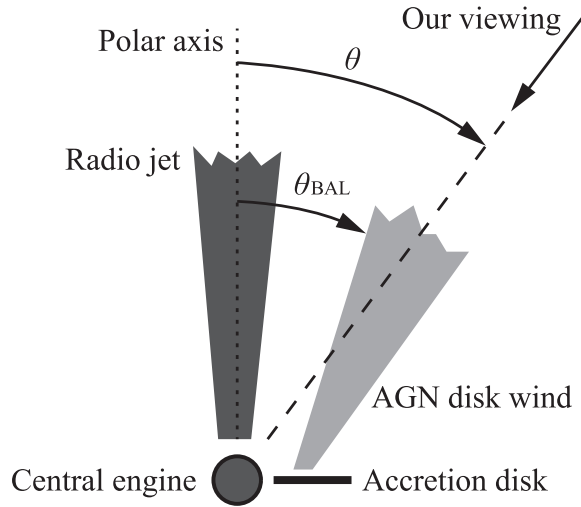


Figure 3.5 Schematic picture of geometric relationship between disk wind and jet on the basis of Elvis (2000). If we give constraint to our viewing, θ , a restriction is also imposed on inclination angle of the wind, θ_{BAL} . The scale size of each component in the picture is arbitrary.

from the core (the component A) to a putative approaching component (the component D) is ~ 90 mas and to the receding jet (the component E) is ~ 50 mas. Then, we obtain $\beta \cos \theta \sim 0.3$ (see Figure 3.6) which is nearly consistent with the result derived by the flux density ratio. We obtain $0.3 < \beta < 1$ and $\theta < 73$ deg (Figure 3.6).

In summary, we gave moderate constraints of $\beta > 0.3$ for J1159+0112 (Figure 3.6). This indicates that two kinds of outflows are present in BAL quasars in terms of the velocity (cf. Doi et al., 2009); one is the relatively fast nonthermal jet and the other is slower wind ($\sim 0.1c$). The model of an accretion disk generating both radiation-force-driven wind (e.g., Proga et al., 2000) and non-thermal jets with higher speeds (e.g., Ohsuga & Mineshige, 2011) should be applied to explain radio-loud BAL quasars. On the other hand, our estimations do not set so tight constraints on the orientation.

■ 3.6.2 Constraints on the AGN Wind

The geometry of the disk wind can be inferred from the viewing angle of the radio jet, which should be perpendicular to the innermost region of the accretion disk. The disk wind cuts across the line of sight to the central engine and the pc-scale non-thermal jets (Figure 3.5). The lower end of the range of opening angle for the disk wind, θ_{BAL} , should be less than the upper limit of the viewing angle, θ . This constraint will be an intriguing comparison with the theoretical models of accretion disk because the disk wind is thought to be lifted upward and accelerated to nearly edge-on from the disk by radiation force (Proga et al., 2000). A radio imaging study is one of the most direct ways to test the orientation scheme.

Using the arm-length and flux density ratio, we have set a constraint on $\beta \cos \theta$ for our

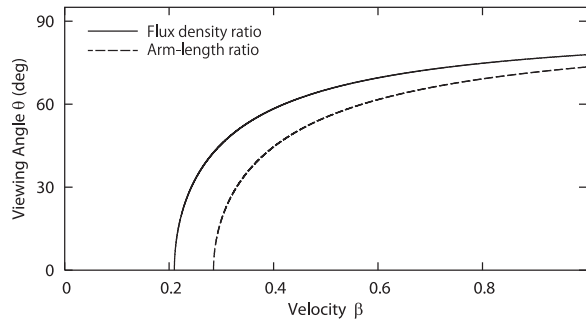


Figure 3.6 Constraints on viewing angles, θ , and bulk velocity, β , of jets. Results derived from flux density ratio (solid) and arm-length ratio (dashed) are shown.

target sources (Section 3.6.1). The result is $\theta_{\text{BAL}} < 73$ deg (Figure 3.6). This estimate gives only a mild constraint. According to the model presented by Elvis (2000), the disk wind bends outward to an opening angle of 60 deg with a divergence of 6 deg to give a covering factor of $\sim 10\%$. The derived inclinations are not strong constraints on the orientation of the disk wind in the framework of the orientation scheme. Stronger constraints can be obtained in a future observation because the capability of this method depends on an image dynamic range.

3.6.3 Classification of Radio Sources

For testing the orientation and evolution schemes of BAL quasars, it is crucial to distinguish between blazars as pole-on viewed AGN and the genuine GPS sources that are dominated by absorbed lobes. Only on the basis of a spectral shape in a single-epoch observation, the flaring state of blazars could be misidentified as the genuine GPS sources. In contrast, blazars show (i) long-term variability, (ii) one-sided jet structure on mas scale, and (iii) high degree of polarization, while the genuine GPS sources show (i) no significant spectral variability, (ii) usually two-sided structure on mas scale, and (iii) unpolarized radio emission in the core region at least at low frequency. These criteria allow us to distinguish the genuine GPS sources from the blazars in a convincing way (Tinti et al., 2005; Orienti et al., 2007). In terms of the morphology (Section 3.5.1) and the polarization (Section 3.5.2), J1159+0112 is classified as the genuine GPS source. Although discrimination between the blazars and the GPS sources was inconclusive in terms of radio flux variability (Section 3.5.3), we conclude that the genuine GPS sources can be hosted by BAL quasars in Doi et al. (2009).

3.6.4 Interpretations of the Radio Morphology

It is notable that J1159+0012 shows multiple components with the extension of more than 100 mas which corresponds to the projected size of ~ 1 kpc. The bright central component with GHz-peaked spectrum can be interpreted as the core as often seen in the radio-loud quasars (Blandford & Konigl, 1979). However, this source apparently exhibits the emis-

sions in both sides of the core while most of quasars show an one-side jet structure in VLBI-resolution scale. The components B–D are relatively brighter than component E, suggesting that these components are the approaching jet components and the components E is the receding jet component. The detection of the counter jet implies that the relativistic beaming is not significant at least in the component E. The most likely explanation is that the counter jet is decelerated at the component E as a result of jet termination. Strong polarized emission ($11.8 \pm 1.4\%$) is seen at the component D. This polarized flux density constitutes the most of polarized flux density detected by VLA. Multi-frequency observations with VLA and a single dish derived the intrinsic EVPA of 24 ± 3 deg which was taken into account the Faraday rotation (Montenegro-Montes et al., 2008a). The resultant magnetic field direction is 114 ± 3 deg which is nearly perpendicular to the position angle of approaching jet. Since the polarized flux density detected by our VLBA observations is almost equal to that by VLA, this magnetic field direction represents the one at the component D. Both strong polarized flux density and magnetic field perpendicular to the jet are consistent as if this feature results from the compression of random magnetic field (Laing, 1980), such as by shock. These evidences allow us to infer that the components D and E are hot spots produced by the jet termination by ISM (e.g., Dreher, 1981; Tsien, 1982). It is noted that the most of radio-loud quasars show two-sided structure at low frequencies (Bridle et al., 1994). Thus, the detection of the counter jet component in J1159+0012 is not surprising. The absence of counterpart of the components B and C is also naturally explained if both approaching and receding jets are still relativistic before reaching to the hot spots. One may think the lack of polarized emission from the component E is against above scenario but, if the component E possesses the similar level of fractional polarization to the component D, the polarized flux density is only ~ 1 mJy which is too diffuse to be detected by our observation. Besides, the counter jet component could be affected by rather significant Faraday depolarization. We need polarization observation with higher sensitivity particularly at higher frequency to confirm the polarized emission from the component E.

This source shows point-like structure in arcsecond scale (e.g., the FIRST survey; Becker et al. 1995). Two-sided structure with an angular size of about 200 mas, the same structure revealed by our observation, is seen on the image at 327 MHz by VLBA (Kanekar et al., 2009), whose total flux density is comparable to that measured by the Texas survey (Douglas et al., 1996) at 365 MHz. Therefore, the most of radio emission originates in the structure between the components D and E. Even if we assume a small viewing angle as usually inferred for the quasars, for instance 10 degree, total extent of these radio emissions is ~ 5 kpc. This source size is relatively compact as compared to the classical double radio galaxies. If we adopt typical hotspot velocity in young radio sources (Conway, 2002), the

kinematic age of this source is $\sim 10^4\text{--}10^5$ year. The source might be the product of recent episode of jet activity.

3.7 Conclusions

Previous arcsecond-scale radio observations made by Montenegro-Montes et al. (2008a) suggested that many GPS/CSS sources are associated with BAL quasars. This has been one of the bases for the evolution scheme. However, genuine GPS/CSS sources which are dominated by absorbed lobes are sometimes misidentified as a flaring state of blazars. To distinguish the genuine GPS/CSS sources from the blazars, high resolution direct imaging with VLBI is efficient. In addition, VLBI observations can determine the orientation of the sources. This can be the most direct way to test the orientation scheme. For the above purposes, we performed multi-frequency VLBI imaging of a radio-loud BAL quasar, J1159+0112, whose radio spectrum is similar to that found in GPS sources. Our conclusions are summarized as follows:

- The source exhibits a two-sided structure across ~ 1 kpc and no significant polarization in its central component. The radio spectrum in the integrated flux density can be represented by a hybrid of a MHz-peaked and GHz-peaked spectral component. The former corresponds to the extended 1-kpc scale structure while the latter corresponds to the central component containing a possible jet base. These characteristics are consistent with those of the genuine GPS sources associated with quasars. Thus, BAL quasars can host the genuine GPS sources. This will be an important basis for spectral study described in Chapter 4.
- Utilizing the two sided morphology of the source, we obtained the jet speed and the inclination of the sources as $\beta > 0.2$ and $\theta < 73$ deg, respectively. The latter result does not compete with the orientation model presented by Elvis (2000).

Low-frequency Survey Observations of BAL quasars

4

4.1 Introduction

Radio spectrum of non-thermal sources gives us diverse insights into the nature of the sources. In specific, convex radio spectrum suggests absorption of compact radio sources. These sources suffering from absorption are considered to be young sources which is a progenitor of large-sized radio galaxies (Phillips & Mutel, 1982; O’Dea & Baum, 1997) or frustrated sources confined by the ambient medium (van Breugel et al., 1984; O’Dea et al., 1991). Thus, spectral studies at radio provide clues about the age of the sources or the ambient medium. In this chapter, utilizing these properties found in non-thermal sources, we would like to investigate the nature of BAL quasars in terms of the evolution and orientation schemes.

The first multi-frequency radio observation of BAL quasars was made by Montenegro-Montes et al. (2008a) with arcsecond scale resolution. They found a large number of GPS/CSS radio sources in a sample selected from Becker et al. (2000, 2001). Though genuine GPS/CSS sources that are candidates for young or frustrated radio sources are sometimes misidentified by blazars only based on arcsecond-scale observations (Torniainen et al., 2005, 2007), in Chapter 3 we confirmed the existence of the genuine GPS source associated with a BAL quasar using VLBI (also see Hayashi et al., 2013). Now, these results imply the evolution scheme (Becker et al., 2000) where BAL quasars are in a relatively early phase before its emergence from a thick shroud which frustrates the non-thermal jet (Voit et al., 1993; Gregg et al., 2006; Lípari & Terlevich, 2006). Meanwhile, inverted spectra due to absorption have not been fully detected yet. This is because previous observations were mainly made at gigahertz frequency (Montenegro-Montes et al., 2008a; DiPompeo et al., 2011; Bruni et al., 2012). For instance, at redshift of $z \gtrsim 2$ where most of BAL quasars

are found, observing frequency of 1.4 GHz corresponds to $\gtrsim 5$ GHz at rest. To detect GPS/CSS sources completely and then to test the evolution scheme, observations at the lower frequency are required.

In addition to the above argument, comparisons of optically-thin part of radio spectra between BAL and non-BAL quasars have also been made by several authors (DiPompeo et al., 2011; Bruni et al., 2012). DiPompeo et al. (2011) clearly showed that in the gigahertz regime radio spectra of BAL quasars are steeper than non-BAL quasars. Because spectral index can be a statistical indicator of the inclination (e.g., Massaro et al., 2013), BAL quasars are statistically suggested to be sources seen from relatively edge-on viewing. This is consistent with what is expected from the orientation scheme (Elvis, 2000). At the same time, DiPompeo et al. (2011) also found flat or inverted spectra in BAL quasars which are similarly found in non-BAL quasars. They concluded that the range of viewing angles is similar to non-BAL quasars. However, radio sources suffering from the absorption show flat or inverted spectrum regardless of the inclination, and the flat or inverted spectra do not necessarily mean the pole-on inclination of BAL quasars. Hence, also to test the orientation scheme, it is important to understand the absorption of BAL quasars at the low frequency.

Thus far, a statistical comparison at the low frequency has been made only by Fine et al. (2011) utilizing NRAO VLA Sky Survey at 1.4 GHz (NVSS Condon et al., 1998) and Westerbork Northern Sky Survey at 327 MHz (WENSS Rengelink et al., 1997). However, their sample is small; only 25 BAL quasars are contained there. Moreover, the angular resolution of NVSS and WENSS (~ 1 arcmin) is not so high to avoid contamination from background sources. Therefore, extensive survey observations with high angular resolution and a larger sample have been expected.

In this chapter, we will present results of low frequency survey observations of BAL quasars made with the Giant Meterwave Radio Telescope (GMRT). Because of the high angular resolution of GMRT (~ 9 arcsec at 322 MHz), we can make a statistical comparison at the low frequency avoiding the contamination. This is the first systematic low-frequency survey program of BAL quasars in the world. We describe our sample in Section 4.2. The observation and data reduction are described in Sections 4.3 and 4.4, respectively. The result is presented in Section 4.5. We discuss the presence of the absorption and its relation to the evolution and orientation schemes in Section 4.6. Finally, conclusions are summarized in Section 4.7. Throughout this chapter, we adopt a cosmology consistent with WMAP results of $h = 0.71$, $\Omega_m = 0.27$, and $\Omega_\Lambda = 0.73$ (Komatsu et al., 2011).

4.2 Target Selection

We selected our targets from the Faint Images of the Radio Sky at Twenty centimeters survey (FIRST survey; Becker et al. 1995) and the quasars catalog (Schneider et al., 2007)

from the fifth data release (DR5; Adelman-McCarthy et al. 2007) of Sloan Digital Sky Survey (SDSS; York et al., 2000). Now, how to define BAL is one of the fundamental issue in the field (Hall et al., 2002; Ganguly et al., 2007; Knigge et al., 2008). Classically, balnicity index (BI, see Equation 2.2; Weymann et al. 1991) is adopted as a conservative definition. However, Knigge et al. (2008) suggested BI could underestimate the existence of BAL. In this study, we adopt modified balnicity index (BI_0 , Equation 2.4; Gibson et al. 2009) which is designed to be less strict than BI. Then, selection criteria of BAL sample are following; (i) $1.68 \leq z \leq 4.93$ where blue-shifted and high-velocity C IV absorption line falls inside the SDSS spectral bandpass, (ii) C IV BAL is reported by Gibson et al. (2009), (iii) radio counterparts with ≥ 10 mJy in the FIRST survey are located within 3 arcsec of each quasar, and (iv) RA is in the ranges of 10–17 hrs. As a result, the sample consists of 48 sources (Table 4.1) of which 35 sources overlap with sample in DiPompeo et al. (2011). In the sample, three sources are resolved by the FIRST survey, whose images are shown in Figure 4.1.

We also constructed the same number of non-BAL sample for use as a comparison. To minimize antenna slewing time during the observations, we did not use the sample constructed by DiPompeo et al. (2011). The selection criteria of our non-BAL sample are following; (i) redshift is in the range of $1.68 \leq z \leq 4.93$ and within 20% of each BAL quasar, (ii) flux density at 1.4 GHz is within 10% of each BAL quasar, (iii) i -band magnitude is within ± 1.0 of each BAL quasar, and (iv) the source can be observed with a phase calibrator selected for BAL sample if possible. Table 4.2 lists the non-BAL sample. We inspected their SDSS spectrum at rest 1400–1600 Å visually and confirmed that they are free from significant broad absorption. In the sample, two sources are resolved by the FIRST survey, whose images are shown in Figure 4.2. Four sources in the sample overlap with that in DiPompeo et al. (2011). Figure 4.4 shows distributions of redshift, specific luminosity at 5 GHz assuming a spectral index of $\alpha = -0.7$, and i -band absolute magnitude for the BAL and non-BAL sample. A Kolmogorov-Smirnov (KS) test and Wilcoxon rank sum (RS) test indicated that these distributions are indistinguishable between the two samples at 5% significance.

We made Monte-Carlo simulation to evaluate possibility that the two samples show significant difference in spectral index between 1.4 and 5 GHz. First, BAL and non-BAL samples, which contain N radio-loud sources each, were selected from sources observed by DiPompeo et al. (2011) randomly. We made a KS test and a RS test for the randomly selected samples to test difference in the spectral index reported in DiPompeo et al. (2011). We repeated this procedure 10^5 times for each N , and counted trials showing the significant difference at 5% significance. The result is shown in Figure 4.3. Based on the RS test, the

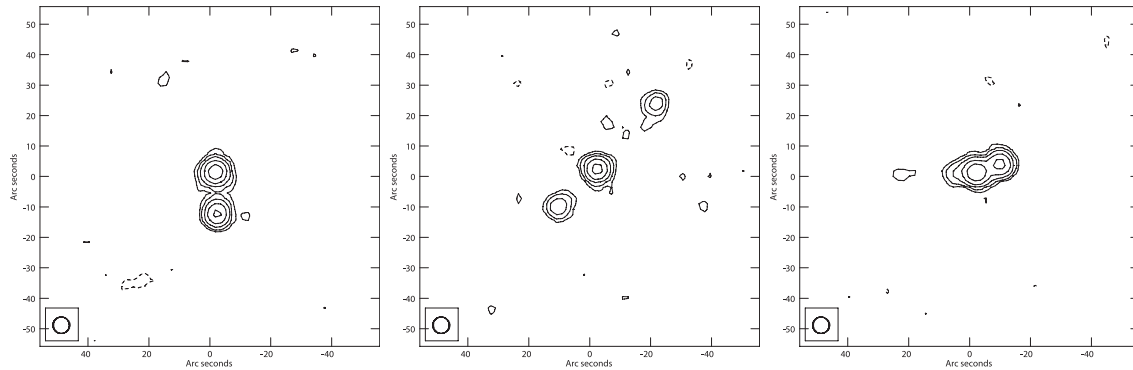


Figure 4.1 1.4-GHz images of BAL quasars resolved by the FIRST survey. Three resolved BAL quasars are shown from the left to the right; 100109.42+114608.8, 123954.15+373954.5, and 133004.34+605949.7. The contours are in successive powers of 2 times the base contour level that is 3σ noise level measured on the image plane. Restoring beam is represented in each map. The optical quasars position corresponds to the map center.

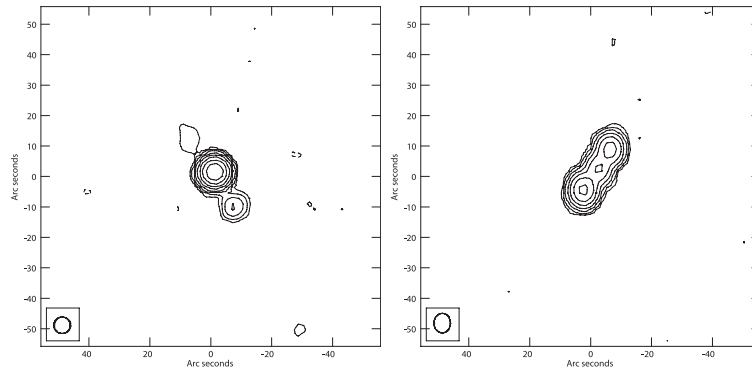


Figure 4.2 1.4-GHz images of non-BAL quasars resolved by the FIRST survey. Two resolved non-BAL quasars are shown from the left to the right; 141031.00+614136.9 and 142033.25−003233.3. Same as Figure 4.1.

samples with $N = 48$ are expected to show the significant difference $\sim 80\%$ of the time.

The purpose of the observation is obtaining spectral index between 322 MHz and 1.4 GHz. However, we do not obtain the data at the frequencies simultaneously. As a check for the variability, we compared the flux densities from NVSS and the FIRST survey. We utilize variability significance defined as

$$\sigma_{\text{var}} = \frac{S_1 - S_2}{\sqrt{\sigma_1^2 + \sigma_2^2}}, \quad (4.1)$$

where S_i and σ_i are integrated flux density and its uncertainty of i -th epoch data, respectively (Zhou et al., 2006). We recognize $\sigma_{\text{var}} > 3$ as significant variability. Here, errors were estimated to be 3% of integrated flux density (Condon et al. 1998). As shown in Figure 4.5, we found no significant variability for most of the targets. Although two-epoch observations are not enough to conclude that the sources are stable, the variability could not influence our measurement of the spectral index statistically.

Table 4.1. The BAL Quasar Sample.

Source Name (SDSS J) (1)	z (2)	M_i (mag) (3)	BI (km s ⁻¹) (4)	BI ₀ (km s ⁻¹) (5)	$S_{1.4}$ (mJy) (6)	$\log L_{5.0}$ (erg s ⁻¹ Hz ⁻¹) (7)	$S_{0.322}$ (mJy) (8)	α (9)
100109.42+114608.8	2.278	-27.1	716.1	3030.5	23.8 ± 0.7 ^a	32.4
100424.88+122922.2	2.640	-25.8	4534.0	4534.0	12.3 ± 0.4	32.3
104059.79+055524.4	2.443	-26.6	4120.3	4120.3	42.2 ± 1.3	32.7	176.0 ± 19.5	-0.97 ± 0.03
104452.41+104005.9	1.882	-27.9	2463.3	3283.9	17.2 ± 0.5	32.1	< 10.6	> 0.33
105416.51+512326.0	2.341	-27.2	337.5	1056.2	33.9 ± 1.0	32.6	53.6 ± 6.5	-0.31 ± 0.04
110206.66+112104.9	2.351	-27.7	0.0	75.3	83.1 ± 2.5	33.0	< 10.6	> 1.40
110531.42+151215.9	2.063	-27.0	4556.4	4556.4	12.3 ± 0.4	32.0	22.0 ± 5.0	-0.39 ± 0.07
112241.46+303534.9	1.810	-28.6	0.1	0.1	10.0 ± 0.3	31.8	< 13.6	> -0.21
112938.47+440325.0	2.212	-27.8	0.0	806.5	42.0 ± 1.3	32.6	< 7.4	> 1.18
113152.56+584510.2	2.262	-26.8	2.5	925.3	12.8 ± 0.4	32.2	40.6 ± 5.2	-0.79 ± 0.04
113445.83+431858.0	2.184	-26.9	4443.4	4443.4	28.0 ± 0.9	32.5	< 34.0	> -0.13
115901.75+065619.0	2.191	-26.6	1675.4	1675.4	160.1 ± 4.8	33.2	455.0 ± 45.9	-0.71 ± 0.03
115944.82+011206.9	2.000	-28.4	0.0	937.9	268.5 ± 8.1	33.4	1027.0 ± 102.9	-0.91 ± 0.03
121323.94+010414.7	2.829	-26.0	1551.0	1551.0	22.9 ± 0.7	32.6	13.2 ± 3.4	0.38 ± 0.08
121539.66+090607.4	2.723	-28.0	116.3	116.3	49.8 ± 1.5	32.9	14.3 ± 5.5	0.85 ± 0.11
122848.21-010414.5	2.655	-28.1	17.1	17.1	30.8 ± 0.9	32.7
123411.73+615832.6	1.946	-26.9	4907.9	4907.9	24.0 ± 0.7	32.3	< 8.4	> 0.71
123511.59+073330.7	3.035	-27.9	0.0	93.5	11.3 ± 0.4	32.4
123717.44+470807.0	2.271	-27.3	868.7	868.7	80.2 ± 2.4	33.0
123954.15+373954.5	1.841	-25.5	959.3	959.3	18.5 ± 0.6 ^b	32.1	< 7.6	> 0.61
125243.85+005320.1	1.693	-27.1	94.6	94.6	12.8 ± 0.4	31.9	< 6.4	> 0.47
130332.05+014407.4	2.109	-26.2	0.0	136.0	38.0 ± 1.1	32.6	33.7 ± 5.4	0.08 ± 0.05
130448.06+130416.5	2.568	-27.3	4.8	4.8	50.0 ± 1.5	32.9	< 3.4	> 1.84
130756.73+042215.5	3.022	-28.7	879.0	879.0	14.9 ± 0.5	32.5	13.9 ± 3.0	0.05 ± 0.06
133004.34+605949.7	1.734	-26.2	72.1	72.1	28.5 ± 0.9 ^c	32.2	98.3 ± 11.0 ^d	-0.84 ± 0.05
133701.39-024630.3	3.064	-27.9	0.0	2.3	44.8 ± 1.4	33.0	< 6.2	> 1.35
135550.30+361627.6	1.855	-26.3	0.0	604.4	10.7 ± 0.4	31.9	< 3.2	> 0.81
135910.45+563617.4	2.248	-27.9	56.2	156.9	17.9 ± 0.6	32.3	39.6 ± 4.8	-0.54 ± 0.04
135910.77+400218.6	2.013	-26.8	432.9	432.9	15.0 ± 0.5	32.1	23.1 ± 4.6	-0.29 ± 0.06
140126.15+520834.6	2.972	-28.0	80.3	80.3	37.1 ± 1.1	32.9	< 9.7	> 0.92
140501.12+041535.7	3.215	-27.1	12.5	12.5	1055.9 ± 31.7	34.4	1258.3 ± 125.9	-0.12 ± 0.03
141313.63+411637.8	2.616	-28.4	1053.3	1053.3	26.7 ± 0.8	32.6	21.3 ± 3.6	0.15 ± 0.05
141334.38+421201.7	2.817	-27.9	0.0	1446.9	18.7 ± 0.6	32.5	< 5.8	> 0.79
141437.99+045537.4	1.851	-26.1	2015.1	2201.2	11.8 ± 0.4	31.9	20.9 ± 3.0	-0.39 ± 0.04
141736.05+372825.9	2.554	-26.1	0.0	177.3	25.8 ± 0.8	32.6	< 9.2	> 0.70
143340.35+512019.3	1.863	-26.9	1085.7	1085.7	12.6 ± 0.4	32.0	49.6 ± 5.4	-0.93 ± 0.03
144434.80+003305.3	2.036	-26.5	0.0	163.0	13.2 ± 0.4	32.1	7.3 ± 3.3	0.40 ± 0.13
145910.13+425213.2	2.967	-28.2	87.1	87.1	13.7 ± 0.4	32.4	< 6.7	> 0.49
150332.93+440120.6	2.050	-27.0	1405.1	1405.1	11.2 ± 0.4	32.0	35.5 ± 4.4	-0.78 ± 0.04
150823.71+334700.7	2.208	-27.6	663.5	663.5	132.0 ± 4.0	33.1	160.5 ± 16.2	-0.13 ± 0.03
151630.30-005625.5	1.921	-27.0	0.0	517.0	25.5 ± 0.8	32.3	52.1 ± 5.9	-0.49 ± 0.03
153729.54+583224.6	3.059	-26.8	0.0	1432.0	14.2 ± 0.5	32.5	< 4.1	> 0.84
155429.40+300118.9	2.693	-28.4	574.8	574.8	41.2 ± 1.2	32.8	47.9 ± 6.0	-0.10 ± 0.04
160354.15+300208.6	2.030	-27.7	0.0	480.0	54.2 ± 1.6	32.7	67.2 ± 8.2	-0.15 ± 0.04
162453.47+375806.6	3.381	-28.4	900.5	900.5	56.4 ± 1.7	33.2	62.9 ± 7.2	-0.07 ± 0.04
162559.90+485817.5	2.724	-28.4	3447.9	3447.9	25.5 ± 0.8	32.6	40.7 ± 4.7	-0.32 ± 0.04
162656.74+295328.0	2.312	-26.9	283.4	283.4	11.3 ± 0.4	32.1	< 8.4	> 0.20
165543.24+394519.9	1.753	-27.2	3635.3	3635.3	10.2 ± 0.3	31.8	< 10.7	> -0.04

Note. — Column 1: object name in the SDSS DR5. Column 2: redshift. Column 3: i-band absolute magnitude. Column 4: balnicity index. Column 5: modified balnicity index. Reference for Columns 1–5 is Gibson et al. (2009). Column 6: FIRST 1.4-GHz integrated flux density (Becker et al., 1995). Column 7: specific radio luminosity at rest 5 GHz calculated by FIRST integrated flux density assuming spectral index of $\alpha = -0.7$. Column 8: our new measurement of 322-MHz integrated flux density. Column 9: two-point spectral index between 1.4 GHz and 322 MHz.

^aThe source is resolved into two components which are 13.7 mJy and 10.1 mJy.

^bThe source is resolved into two components which are 10.7 mJy, 4.3 mJy, and 3.5 mJy.

^cThe source is resolved into two components which are 18.1 mJy and 10.4 mJy.

^dThe source is resolved into two components which are 57.3 mJy and 41.0 mJy.

Table 4.2. The non-BAL Quasar Sample.

Source Name (SDSS J) (1)	z (2)	M_i (mag) (3)	$S_{1.4}$ (mJy) (4)	$\log L_{5.0}$ (erg s ⁻¹ Hz ⁻¹) (5)	$S_{0.322}$ (mJy) (6)	α (7)
074927.90+415242.3	3.111	-28.9	15.2 ± 0.5	32.5	28.6 ± 5.4	-0.43 ± 0.06
095537.94+333503.9	2.477	-28.6	36.6 ± 1.1	32.7	< 5.4	> 1.31
103808.94+464249.1	1.924	-26.9	12.2 ± 0.4	32.0	11.9 ± 4.2	0.01 ± 0.11
111048.93+045608.0	2.208	-26.8	65.2 ± 2.0	32.8	80.3 ± 9.2	-0.14 ± 0.04
111336.10+494034.7	2.466	-27.6	28.7 ± 0.9	32.6	68.9 ± 7.9	-0.60 ± 0.03
111434.01+041434.0	1.719	-26.0	17.1 ± 0.5	32.0	< 8.0	> 0.52
112854.24+035341.4	1.829	-26.9	19.8 ± 0.6	32.1	< 7.3	> 0.68
113017.37+073212.9	2.647	-28.9	31.6 ± 1.0	32.7	< 8.6	> 0.89
113716.36+371046.4	2.027	-27.3	10.3 ± 0.3	32.0	< 18.0	> -0.38
113854.52+394553.6	2.159	-27.2	21.2 ± 0.7	32.3	< 7.1	> 0.74
115534.50+575156.4	1.967	-26.4	23.9 ± 0.7	32.3
121911.23-004345.5	2.293	-27.7	94.5 ± 2.8	33.0
123215.09+554049.4	2.307	-26.3	11.1 ± 0.4	32.1
123545.38-033610.9	2.375	-26.6	10.2 ± 0.3	32.1
123856.09-005930.8	1.844	-27.3	14.0 ± 0.4	32.0	< 6.7	> 0.50
124409.64+554823.4	1.768	-25.9	10.2 ± 0.3	31.8
125321.59-032315.7	1.771	-26.6	26.7 ± 0.8	32.2	50.9 ± 11.9 ^a	-0.44 ± 0.14
131003.35+535348.2	3.278	-27.2	14.5 ± 0.5	32.6
131926.27+143439.9	2.541	-27.6	59.3 ± 1.8	32.9	68.7 ± 7.3	-0.10 ± 0.03
133754.41+451239.1	2.758	-28.3	25.8 ± 0.8	32.7	17.7 ± 3.8	0.26 ± 0.06
134253.64+390223.6	1.723	-26.2	13.4 ± 0.4	31.9	< 12.2	> 0.07
134303.25+502832.0	1.962	-26.6	39.9 ± 1.2	32.5	68.5 ± 7.4	-0.37 ± 0.03
134520.40+324112.5	2.255	-27.7	14.6 ± 0.5	32.2	< 2.3	> 1.27
140637.60+141530.0	2.926	-27.3	40.9 ± 1.2	32.9	130.0 ± 13.2	-0.79 ± 0.03
140909.74+071226.1	2.734	-27.1	11.7 ± 0.4	32.3	< 5.0	> 0.58
141031.00+614136.9	2.246	-27.0	125.0 ± 3.8 ^b	33.1	64.1 ± 6.9	0.45 ± 0.04
141846.20+482308.2	2.193	-26.2	12.8 ± 0.4	32.1	< 6.1	> 0.50
142009.33+392738.5	2.295	-26.9	38.4 ± 1.2	32.6	40.0 ± 5.7	-0.03 ± 0.04
142033.25-003233.3	2.682	-27.3	77.6 ± 2.3 ^c	33.1	279.1 ± 28.7 ^d	-0.87 ± 0.05
142326.05+325220.3	1.905	-29.3	8.2 ± 0.3	31.8	< 4.2	> 0.45
142352.38+031125.8	1.884	-26.9	55.8 ± 1.7	32.6	63.3 ± 7.1	-0.09 ± 0.03
142921.87+540611.2	3.013	-26.5	1165.4 ± 35.0	34.4	2441.4 ± 244.2	-0.50 ± 0.03
143243.29+410327.9	1.970	-27.8	261.7 ± 7.9	33.3	410.3 ± 41.2	-0.31 ± 0.03
143708.18+040534.3	2.025	-27.5	16.5 ± 0.5	32.2	< 8.8	> 0.43
143737.06+094847.7	2.162	-26.8	181.2 ± 5.4	33.3	330.8 ± 33.2	-0.41 ± 0.03
144752.46+582420.3	2.983	-28.1	33.2 ± 1.0	32.8	8.2 ± 3.0	0.95 ± 0.11
145627.72+414944.2	2.668	-26.5	13.2 ± 0.4	32.3	< 7.7	> 0.37
145924.24+340113.1	2.790	-28.3	21.7 ± 0.7	32.6	18.9 ± 2.8	0.10 ± 0.04
151258.36+352533.2	2.236	-26.7	47.5 ± 1.4	32.7	34.8 ± 4.3	0.21 ± 0.04
152314.87+381402.0	3.159	-27.9	47.7 ± 1.4	33.0	32.9 ± 4.4	0.25 ± 0.04
154644.24+311711.3	2.122	-26.3	12.7 ± 0.4	32.1	38.7 ± 7.5	-0.76 ± 0.06
154935.74+314338.2	1.815	-25.8	11.0 ± 0.4	31.9	< 4.7	> 0.57
155816.63+502953.7	1.900	-26.5	16.7 ± 0.5	32.1	5.5 ± 1.7	0.75 ± 0.09
160911.26+374635.7	2.412	-26.4	22.7 ± 0.7	32.5	80.5 ± 8.7	-0.86 ± 0.03
161920.20+375502.7	2.966	-26.7	18.9 ± 0.6	32.6	75.6 ± 8.9	-0.94 ± 0.04
162004.73+351554.6	2.960	-27.6	50.0 ± 1.5	33.0	131.3 ± 13.4	-0.66 ± 0.03
165137.53+400219.0	2.343	-28.5	43.9 ± 1.3	32.7	26.4 ± 9.4	0.35 ± 0.10
165508.72+373244.6	2.092	-26.6	9.5 ± 0.3	31.9	35.6 ± 4.4	-0.90 ± 0.04

Note. — Column 1: object name in the SDSS DR5. Column 2: redshift. Column 3: i-band absolute magnitude. Reference for Columns 1–3 is Gibson et al. (2009). Column 4: FIRST 1.4-GHz integrated flux density (Becker et al., 1995). Column 5: specific radio luminosity at rest 5 GHz calculated by FIRST integrated flux density assuming spectral index of $\alpha = -0.7$. Column 6: our new measurement of 322-MHz integrated flux density. Column 7: two-point spectral index between 1.4 GHz and 322 MHz.

^bThe source is resolved into two components which are 118.4 mJy, 4.9 mJy and 1.8 mJy.

^cThe source is resolved into two components which are 38.5 mJy, 22.7 mJy, and 16.4 mJy.

^aThe source is resolved into two components which are 23.3 mJy, and 27.6 mJy.

^dThe source is resolved into two components which are 116.0 mJy, and 163.1 mJy.

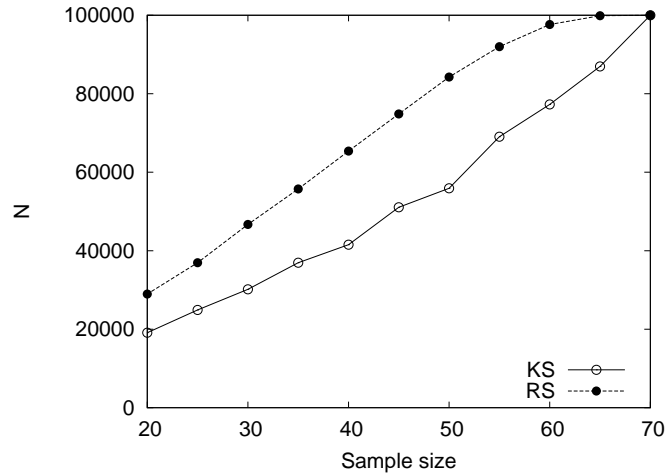


Figure 4.3 Result of the Monte-Carlo simulation to determine the sample size. The horizontal and vertical represent the sample size, N , and number of trials (out of 10^5 runs) that the two samples show significant difference at 5% significance level, respectively. Filled circles and open circles represent result from the RS test and the KS test, respectively. See text for detailed explanation of the simulation.

4.3 GMRT Observations

The GMRT observations were carried out on 2013 May 16–19 (four nights). The observation on each night consisted of a continuous block of 10 hours. To minimize the ionospheric variations, the observations began in the early evening and were running through the night. On each night, 2 of the 30 GMRT antennas (E03 and E04) did not work. The observations were made with its default parameters at 306-MHz band. One 32-MHz wide intermediate frequency centered at 322 MHz was used for both LL and RR polarization. We observed 3C 286 as a flux and bandpass calibrator. Each target was observed with 6–8 minutes scan at 2 different hour angles. Figure 4.6 shows typical u - v coverages of the targets. Phase calibrators were observed every ~ 30 minutes. Angular separation between each target and a phase calibrator was typically ~ 6 deg and 13.5 deg at a maximum.

4.4 Data Reduction

Data reduction was performed with a standard procedure using the Astronomical Image Processing System (AIPS; Greisen 2003) software developed at the National Radio Astronomy Observatory. At first, delay corrections were performed with the AIPS task FRING with bright calibrators. Bandpass calibration for both amplitude and phase was performed with 3C 286. Then, the flux density scale was given by 3C 286 with formula in Baars et al. (1977). Finally, antenna-based amplitude and phase time variation were calibrated with phase calibrators. The error on the absolute flux density scale was generally $\sim 10\%$ (Chandra et al., 2004). At each step, we manually flagged radio frequency interference both

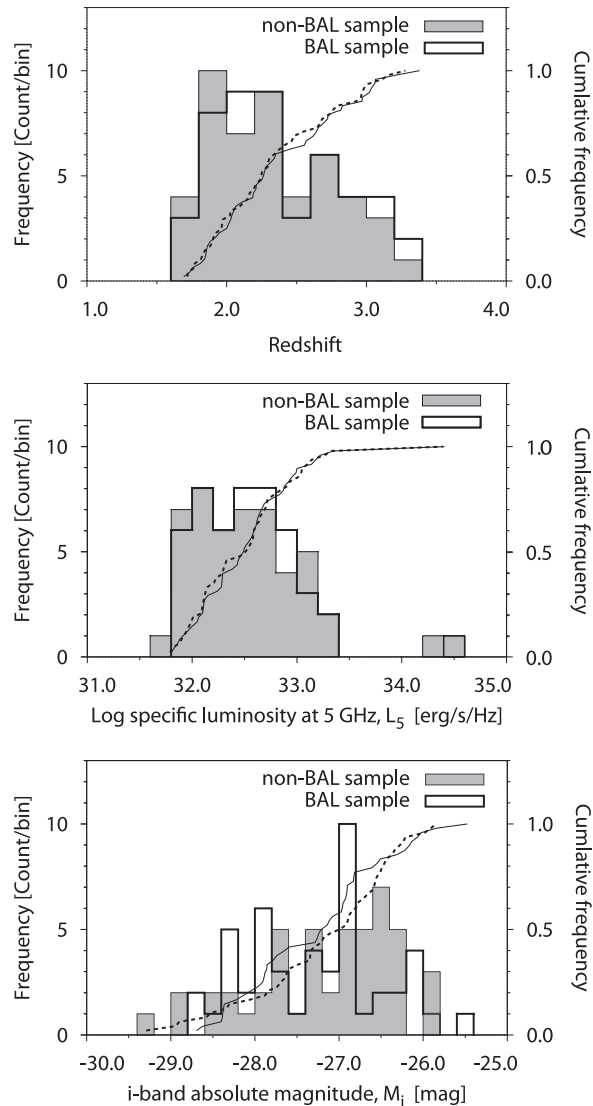


Figure 4.4 Comparison of the properties of BAL and non-BAL sample to be observed; redshift, z , K -corrected specific luminosity at rest 5.0 GHz, $L_{5.0}$, and i -band absolute magnitude, M_i . At each panel, number distributions of BAL (solid black histogram) and non-BAL sample (shaded histogram), and cumulated frequencies for BAL (solid line) and non-BAL sample (dotted line) are displayed. The KS test gives $D_{\text{KS}} = 0.0833, 0.0833, \text{ and } 0.1875$ with a corresponding probability that the two distributions are from the same parent population of $p = 0.996, 0.996 \text{ and } 0.368$ for $z, L_{5.0}, \text{ and } M_i$, respectively. The RS test gives $Z_{\text{RS}} = 1194, 1162, \text{ and } 1018$ with a corresponding probability that the two distributions are from the same parent population of $p = 0.764, 0.945 \text{ and } 0.326$ for $z, L_{5.0}, \text{ and } M_i$, respectively.

on time and frequency domain. Out of the 48 sources in each sample, phase calibration for five BAL quasars and six non-BAL quasars were not able to be made properly because of significant scintillation (see Table 4.1 and 4.2). We did not consider these sources when we made a statistical comparison.

Imaging processes were performed using the `difmap` software (Shepherd, 1997). We conducted self-calibration to solve for the antenna-based phase corrections for Stokes I .

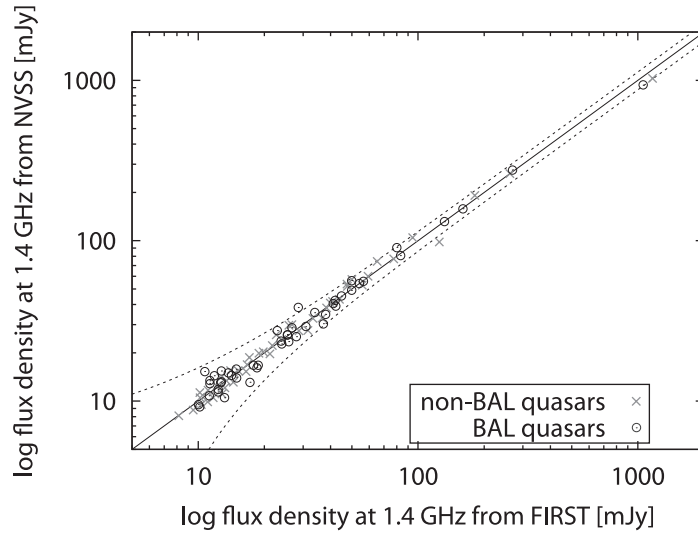


Figure 4.5 Flux density distribution at 1.4 GHz from the FIRST and NVSS. The solid line shows where the two survey fluxes are equal, and the dotted lines show the 3σ variation of the sources around the line of equal flux. The two non-BAL sources that seem to lie well above the line may both have a second object contaminating the NVSS fluxes and are probably not actually variable

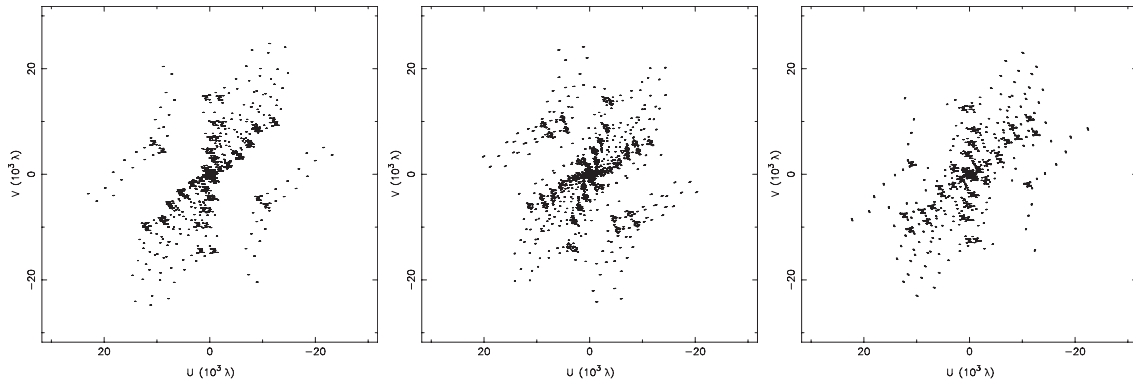


Figure 4.6 Typical u - v coverages of targets at declination of ~ 0 deg, ~ 30 deg, and ~ 50 deg from the left to the right (104059.79+055524.4, 162656.74+295328.0, and 105416.51 +512326.0, respectively). Visibilities affected by significant radio frequency interference are flagged and not displayed here.

When we self-calibrate targets, we did not solve for the amplitude variation. After the self-calibration, we measured flux densities of targets with the AIPS task IMFIT, where an elliptical Gaussian component was fitted within a small box containing the radio source. Major and minor axes of the beam are typically 12 arcsec and 7 arcsec on the uniform weighted images, respectively. Typical rms noise level obtained by IMFIT is ~ 3 mJy beam $^{-1}$, which is consistent with that of previous snapshot survey observation with GMRT (e.g., Mauch et al., 2013).

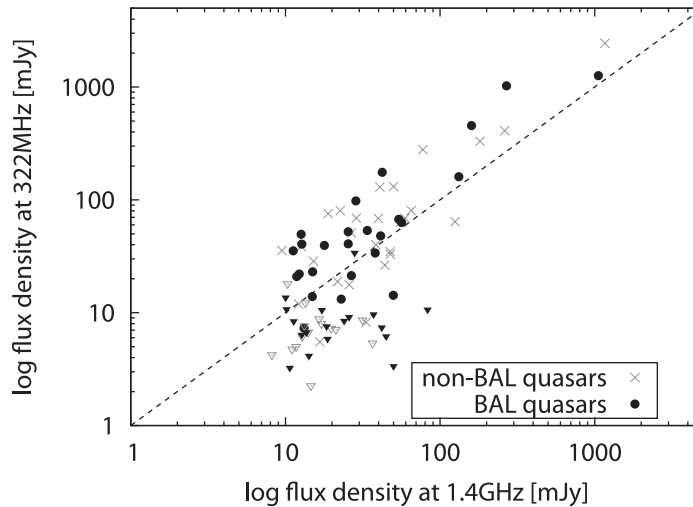


Figure 4.7 Flux densities distribution of our targets at 1.4 GHz and 322 MHz. BAL and non-BAL samples are indicated by filled circle and gray cross, respectively. In case of sources not detected by our observation at 322 MHz, 3σ upper limit is displayed by filled and open triangle for BAL and non-BAL sample, respectively. The dashed lines indicates where the flux densities at the two frequencies are the same.

4.5 Result

4.5.1 Flux Density

Of the targets whose phase was calibrated correctly (43 BAL quasars and 41 non-BAL quasars), we detected 25 BAL quasars and 27 non-BAL quasars. The flux densities at 322 MHz is presented in Tables 4.1 and 4.2. Also its distribution is shown in Figure 4.7. The errors were estimated by the root sum square of thermal noise presented by IMFIT and the systematic error of 10%. The upper limits were presented by 3σ of the thermal noise level. Figure 4.8 shows spectral energy distribution of the BAL sample with data at other frequencies gathered from the literature (Becker et al., 1995; Rengelink et al., 1997; Condon et al., 1998; Montenegro-Montes et al., 2008a; DiPompeo et al., 2011; Bruni et al., 2012).

While most of the targets show point-like structure, we resolved three sources, whose images are displayed in Figure 4.9. Of these sources, 133004.34+605949.7 (BAL) and 142033.25–003233.3 (non-BAL) are also resolved by the FIRST survey (Figure 4.1 and 4.2). Their morphologies obtained with GMRT are consistent with those from the FIRST survey. In contrast, 141031.00+614136.9 (non-BAL) resolved by the FIRST survey was unresolved by our observation, whose GMRT image is shown in Figure 4.10.

4.5.2 Spectral Index

We calculated the spectral index between 1.4 GHz and 322 MHz (Tables 4.1 and 4.2). We used the integrated flux densities even for the resolved sources. The lower limit of the spectral index is calculated with 3σ upper limit of the flux density. Its distribution as a function

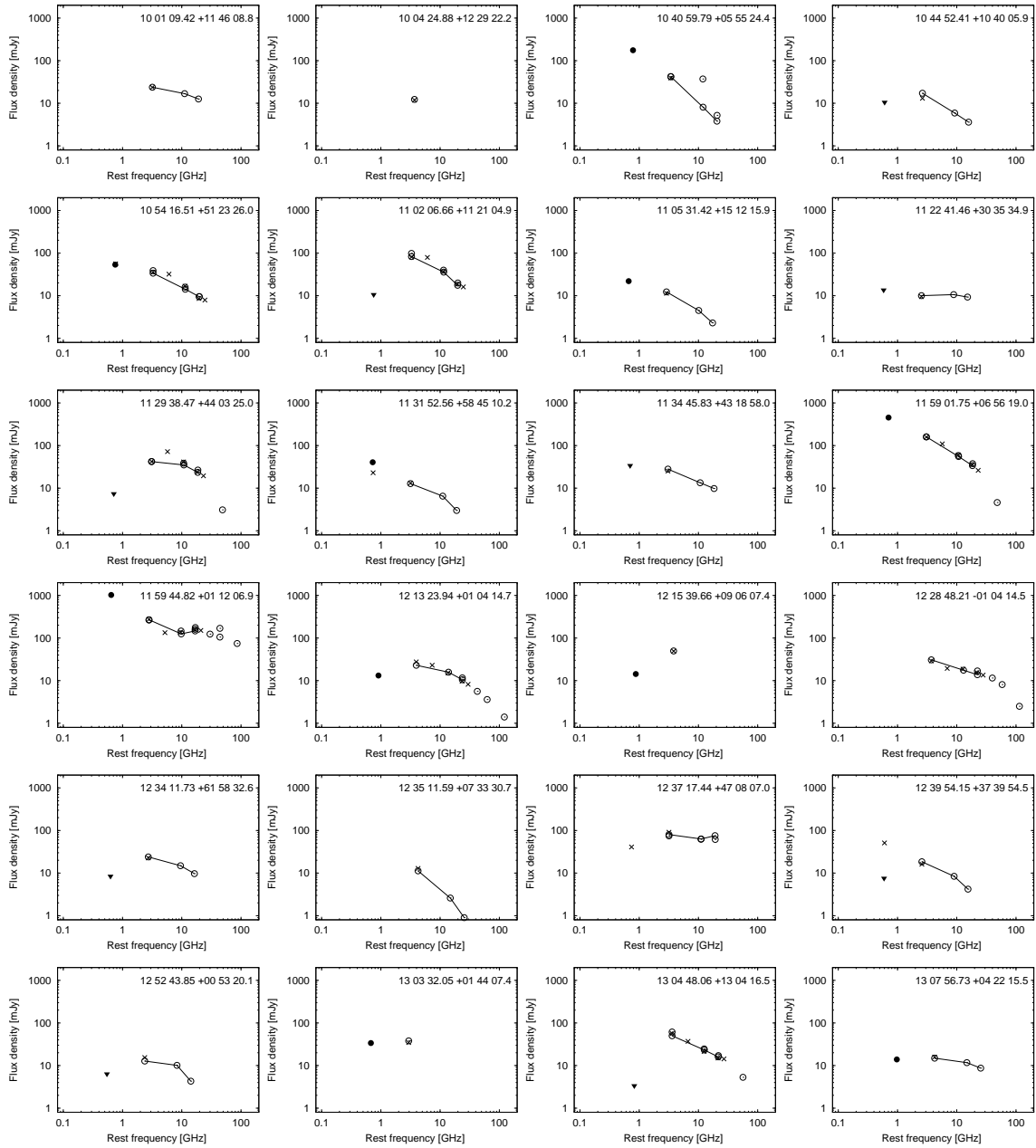
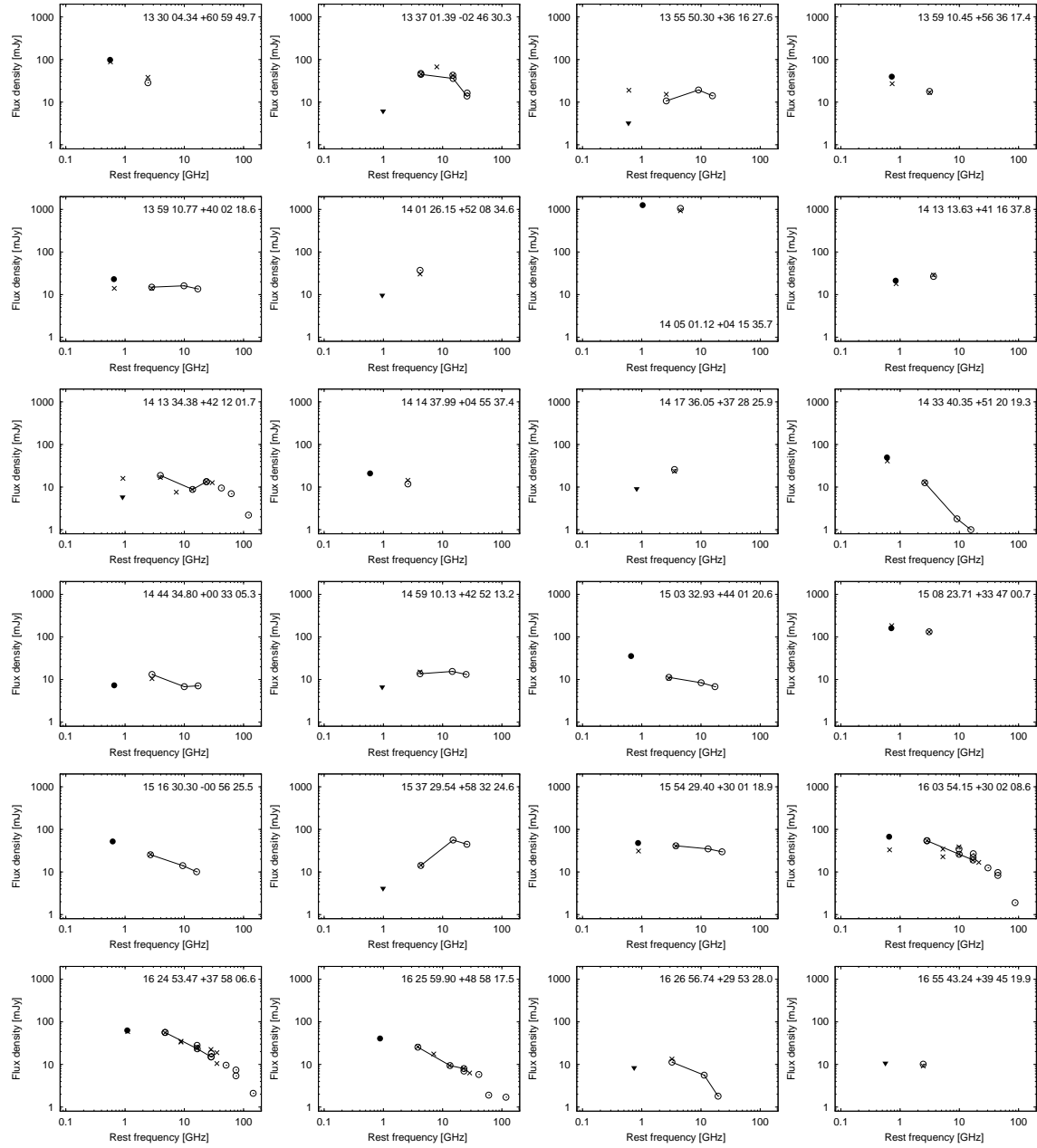


Figure 4.8 Radio spectra of the BAL sample, including literature data. Data points from our observations are indicated by filled circles or filled triangles depending on whether the source is detected. Data points from VLA and the other telescopes are indicated by open circles and crosses, respectively. Lines link the data points from the FIRST survey (Becker et al., 1995) and DiPompeo et al. (2011). The sources whose flux density is not measured with GMRT due to radio frequency interference are also displayed.

Figure 4.8 *Continued*

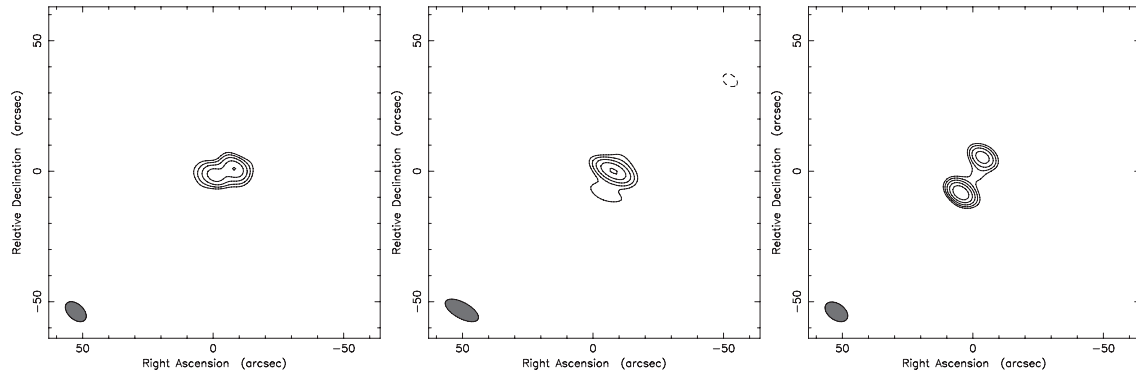


Figure 4.9 Uniform weighted 322-MHz images of the sources resolved by GMRT; 133004.34+605949.7 (BAL), 125321.59–03 2315.7 (BAL), and 142033.25–003233.3 (non-BAL) from the left to the right. The contours are in successive powers of $\sqrt{2}$ times the base contour level that is 3σ noise level measured on the image plane. Restoring beam is represented in each map. The map center corresponds to the optical quasars position.

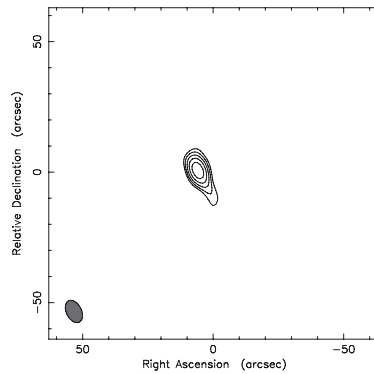


Figure 4.10 Uniform weighted 322-MHz image of the source resolved by the FIRST survey but not resolved by GMRT; 141031.00+614136.9 (non-BAL). Same as Figure 4.9.

of 1.4-GHz flux density is shown in Figure 4.11, suggesting that spectral index distribution in $\alpha \lesssim 0$ is unbiased by the sensitivity of the observations. The number distribution of the spectral index is presented in Figure 4.12. We utilized ASURV package (Lavalley et al., 1992) to test the difference in the distributions with uncensored data. Figure 4.13 shows a Kaplan-Meier survival curve of the two samples. A Gehan’s generalized Wilcoxon test, which assumes the censoring patterns of the two samples are the same, gives the probability that the two samples are from the same parent is $P = 0.909$. In addition, a Peto-Prentice generalized Wilcoxon test, which is a test less affected by differences in the censoring patterns, gives the probability of $P = 0.851$. Thus, at 5% significance level, we cannot reject the null hypothesis that BAL quasars have the same spectral index distribution as non-BAL quasars. The result did not change even if we restricted to the sources unresolved by our observations and the FIRST survey. In this case, we obtained $P = 0.932$ and $P = 0.984$ for the Gehan’s generalized Wilcoxon test and the Peto-Prentice generalized Wilcoxon test, respectively.

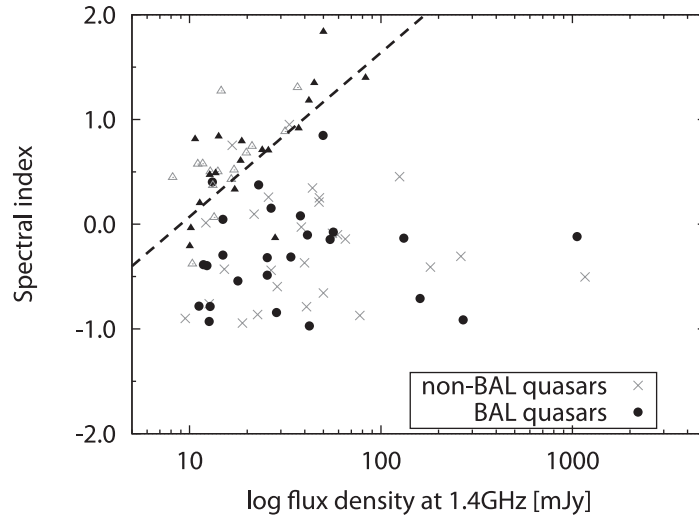


Figure 4.11 Spectral index between 1.4 GHz and 322 MHz as a function of 1.4-GHz flux density. BAL and non-BAL samples are indicated by filled circle and gray cross, respectively. In case of sources not detected by our observation at 322 MHz, lower limit is displayed by filled and open triangle for BAL and non-BAL sample, respectively, which is calculated using the 3σ upper limit of flux density at 322 MHz. The dashed line indicates the spectral index traced by the typical 3σ limit (9 mJy) of the 322-MHz data.

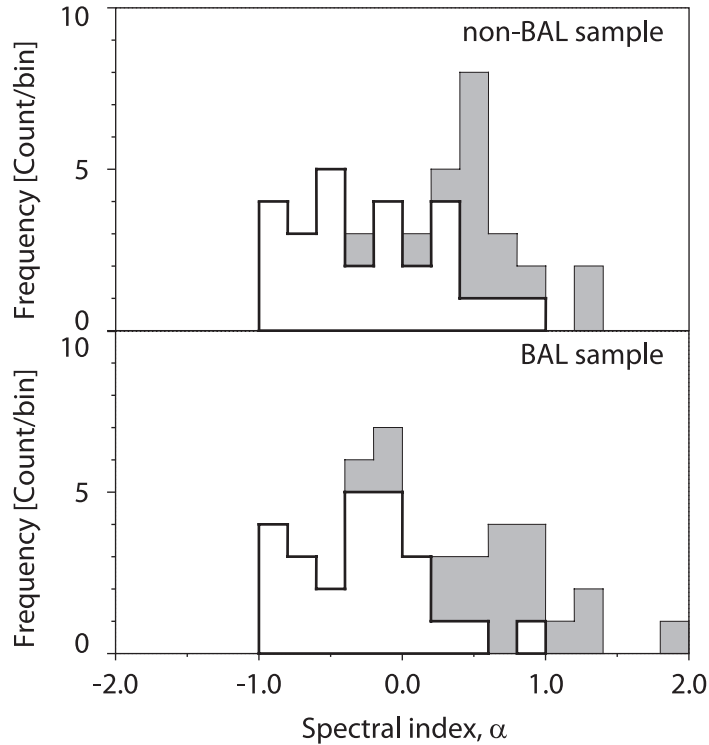


Figure 4.12 Distributions of spectral index between 1.4 GHz and 322 MHz, α , for the non-BAL (top) and BAL (bottom) samples. Sources with lower limit are indicated by shaded histogram.

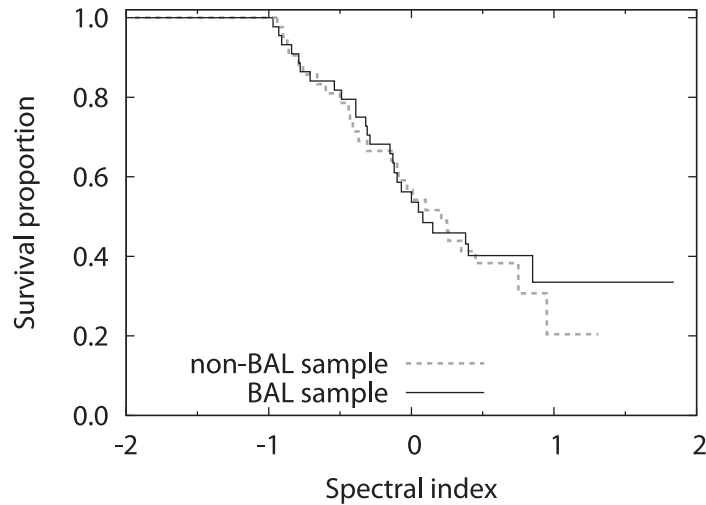


Figure 4.13 A Kaplan-Meier survival curve of the spectral index between 1.4 GHz and 322 MHz. BAL and non-BAL sample are indicated by solid and dashed lines, respectively. The Gehan’s generalized Wilcoxon test gives probability that the two samples are from the same parent is $P = 0.909$. In addition, the Peto-Prentice generalized Wilcoxon test gives the probability of $P = 0.851$.

4.6 Discussion

4.6.1 Absorption at the Low Frequency

Approximately half of the targets show flat or inverted spectra with $\alpha > 0$ between 322 MHz and 1.4 GHz (Figure 4.12). These fractions are significantly larger than that reported by previous observation at higher frequency (Montenegro-Montes et al., 2008a; DiPompeo et al., 2011; Bruni et al., 2012), where only $\sim 15\%$ of their sample shows spectral index with $\alpha > 0$ between 4.9 and 8.4 GHz. This suggests that at the low frequency our targets suffer from absorption. This is supported by a comparison of our result with that of DiPompeo et al. (2011) shown in Figure 4.14. Most of the sources with $\alpha > 0$ at the low frequency show steep spectra with $\alpha < 0$ at the higher frequency. Such a spectral turnover is only made by absorption. Though there are also sources showing inverted spectra both at the high and low frequency, they are only a part of the sample. Therefore, mainly the large fraction results from absorption.

Spectral index distribution of BAL quasars at the low frequency was previously obtained by Fine et al. (2011). However, the above findings of absorption were not mentioned there. Fine et al. (2011) made a statistical comparison at the frequency with sources detected by both WENSS and NVSS. Thus, uncensored data was not considered there. Because sensitivity of WENSS is same as our observation (Rengelink et al., 1997), their statistics lack highly inverted spectral sources (also see Figure 4.11). As a result, the fraction of sources with $\alpha > 0$ is $\sim 10\%$ in Fine et al. (2011). The selection effect causes the difference

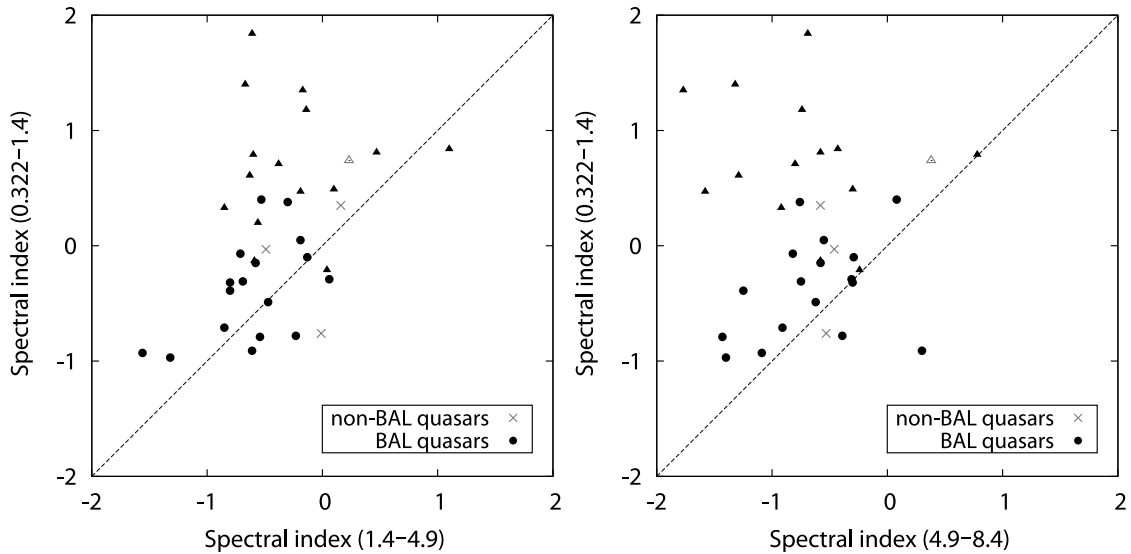


Figure 4.14 Comparison between spectral index from this study (322 MHz–1.4 GHz) and that from DiPompeo et al. 2011 (1.4 GHz–4.9 GHz and 4.9 GHz–8.4 GHz on the left- and right-hand side, respectively). The dashed lines indicates where the spectral index is the same in both regions of the spectrum. BAL and non-BAL samples are indicated by filled circle and gray cross, respectively. In case of sources not detected by our observation at 322 MHz, 3σ upper limit is displayed by filled and open triangle for BAL and non-BAL sample, respectively. In general, for both BAL and non-BAL quasars there is a flattening or a inversion of the radio spectrum towards lower frequencies.

from our result.

4.6.2 Relation of the Absorption to the Evolution Scheme

The flat or inverted spectra are found in 19–22 out of 43 BAL quasars and 22–23 out of 42 non-BAL quasars at the low frequency (Figure 4.12), which correspond to 44–51% and 52–55% of the samples, respectively. Because uncertainty of the fraction assuming normal distribution is $\sim 10\%$, a difference in the fractions is not significant. This is consistent with statistical test with survival curve presented in Section 4.5.2.

Becker et al. (2000) found that most of radio sources associated with BAL quasars are unresolved at sub-arcsecond scale. In addition, Gregg et al. (2006) reported that appearance of FR-II BAL quasars is less common than that assuming both BAL and FR II phenomena are independent with each other (see also Chapter 5). Based on these statistics, the evolution scheme of BAL quasars has been discussed; BAL is observed in a relatively early phase before its emergence from a thick shroud, and non-thermal jet of BAL quasars is frustrated by the ambient medium. If this scenario is true, BAL quasars ought to suffer from strong absorption due to the ambient medium. However, our observations do not show the significant difference in the absorption between the two samples. Though optical depth is not obtained and the sample size could be small to detect the difference, the above evolution scenario is not confirmed in our observations.

Our result is consistent with polarization properties of BAL quasars. If the sources are in the dense environment, weak polarization owing to Faraday depolarization is expected. However, Bruni et al. (2012) reported BAL quasars show polarization properties similar to non-BAL quasars. Moreover, detection rate of dust in BAL quasars is same as that of non-BAL quasars (Willott et al., 2003, 2002; Priddey et al., 2007; Cao Orjales et al., 2012). These results also do not support the galactic-scale frustration and thus the evolution scheme of BAL quasars.

■ 4.6.3 Suggestion for the Orientation Scheme

DiPompeo et al. (2011) reported a wide range of spectral index in BAL quasars, which is same as in non-BAL quasars. Based on the result, they suggested that BAL quasars also include pole-on sources and thus the orientation cannot explain the fraction of the objects (DiPompeo et al., 2012). However, if we take the absorption into account, the situation must be changed. Radio sources suffering from absorption show flat or inverted spectrum regardless of the inclination. Because BAL quasars are also affected by the absorption (Section 4.6.1), the flat/inverted spectra do not necessarily mean its pole-on inclination. To determine the orientation of the absorbed sources, VLBI observations are required (see Chapter 3). Though the existence of pole-on BAL quasars itself can be inferred by other studies (e.g., radio variability; Zhou et al., 2006; Ghosh & Punjly, 2007), the distribution of the spectral index in DiPompeo et al. (2011) does not suggest the incompleteness of the simple observation scheme.

■ 4.6.4 Source with Optically Thin Emission

Most of the targets in DiPompeo et al. (2011) show steep spectrum with $\alpha < 0$ at the high frequency. One of possible origins of the spectral difference at the frequency is synchrotron aging and/or absorption (both free-free and synchrotron self-absorption are considerable). However, distributions of the difference in spectral indices ($\alpha_{3.4}^{4.9} - \alpha_{4.9}^{1.4}$) are comparable between the two samples. Therefore, another explanation is required. Usually, a core shows a flat or inverted spectrum but in contrast decelerated lobes show a steep spectrum. In case of unresolved radio sources in which both a core and lobes are contained, observed spectral index changes with the flux contribution from the beamed flat-spectrum core, which depends on inclination of the sources. If this effect due to viewing angles is the main cause of the difference reported in DiPompeo et al. (2011), at the lower frequency where decelerated lobes dominate, spectral index is expected to be same between the two sample regardless of the inclination of the sources.

In our targets, there are also sources which show optically thin, steep spectrum of $\alpha < 0$. The statistical test in Section 4.5.2 indicates that the difference in the spectral index

distribution between the two samples is not significant. This is consistent with the scenario that the orientation effect results in the difference at the high frequency which converges at the low frequency. However, the sample size is too small in our study; only ~ 20 sources show steep spectrum with $\alpha < 0$. In this case, probability to show the significant difference at the high frequency is only $\sim 20\text{--}30\%$ (Figure 4.3). Thus, it is possible that indistinguishable distribution at the low frequency is simply due to the decreased sample size. Therefore, we cannot discuss this any more. Future extensive observations with larger sample could uncover this issue.

4.7 Conclusions

Based on the evolution scheme, BAL quasars are embedded in a dense environment and expected to suffer from strong absorption. Low-frequency observation is the only way to investigate such an absorption, and thus is important to test the evolution scheme. To perform spectral comparison between BAL and non-BAL quasars, we made GMRT survey observations at 322 MHz. This is the first systematic low-frequency observations for this class of AGN in the world. We can summarize our conclusions as follows:

- Approximately half of the targets were not detected by the observations. Most of these undetected sources could suffer from the absorption. Combined with the flux density obtained by the FIRST survey at 1.4 GHz, we calculated the spectral index. Statistical test using survival curve does not indicate a significant difference in the spectral index distributions between the two samples. Thus, we found a contrary evidence for the evolution scheme.
- In addition to the above, spectral index can be a statistical indicator of the inclination of the sources. Therefore, a wide range of spectral index of BAL quasars similar to non-BAL quasars was a basis for the incompleteness of the orientation scheme (DiPompeo et al., 2011, 2012). However, radio sources suffering from absorption show flat or inverted spectrum regardless of the inclination. Our findings of a significant number of absorbed sources suggest that the range itself cannot be the contrary evidence for the orientation scheme.

Rarity of BAL Quasars with Large-sized FR II Morphology

5

5.1 Introduction

Radio morphology of quasars provides a way to measure orientation of the sources. Especially, distribution of projected linear size can be a good indicator of the orientation (e.g., Barthel, 1989). Now, if the orientation scheme (Elvis, 2000) is valid, fraction of large-sized radio sources associated with BAL quasars should be larger than non-BAL quasars. However, Becker et al. (2000) reported that most of radio-selected BAL quasars exhibit point like structure at resolution of the FIRST survey (~ 5 arcsec; Becker et al., 1995). The first BAL quasar whose radio structure is composed of multi components in arcsecond scale was reported by Gregg et al. (2000). Thus far, such a large-sized radio source has been found in eight BAL quasars (Zhou et al., 2006; Gregg et al., 2006), which is roughly ten times less common than that assuming detections of BAL and large-sized radio morphology are independent with each other (Gregg et al., 2006). In this way, arcsecond-scale radio morphology of BAL quasars is inconsistent with what is expected from the orientation scheme.

As seen from the above, the rarity of the large-sized BAL quasars could be attributed to a difference other than the viewing angles. One of the widely discussed hypotheses is the evolution scheme. There, BAL might be observed in a relatively early phase before its emergence from a thick shroud (Briggs et al., 1984; Lípari & Terlevich, 2006), and non-thermal jet in BAL quasars is frustrated by the ambient medium (Becker et al., 2000; Gregg et al., 2006). Meanwhile, there still remains large ambiguity in the estimate of the rarity. Shankar et al. (2008) suggested that only a factor of difference exists in fraction of BAL quasars between compact and large-sized radio sources. The basis for the evolution scheme has not been established firmly. Moreover, the rarity is not necessarily caused by the frustration but an intrinsic difference in central engines is also considerable. To

discuss the origin of the morphological difference, statistical properties of the large-sized BAL quasars have to be studied. At the moment, the sample presented by Gregg et al. (2006) is inhomogeneous. Thus, the statistical study with a uniform sample has not been made yet.

In this chapter, we will focus on large-sized Fanaroff-Riley class II (FR II) radio sources (Fanaroff & Riley, 1974). FR II sources are found at the high luminosity end in radio total power (Fanaroff & Riley, 1974) which is dominated by radio lobes. At the same time, their linear size becomes several Mpc at most (e.g., Machalski et al., 2008). Because particles that loss energy in the lobes are injected by collimated jet from the central engine (Blandford & Rees, 1974; Scheuer, 1974; Carilli et al., 1991; Giovannini et al., 2001) and lobe advance speed is $\sim 0.1c$ typically (Kawakatu et al. 2008 and references therein), to form these powerful and large-sized radio sources, a certain amount of intense and continuous activity of the engine is needed. Therefore, investigation of the lobes gives us information about integral quantity of radio activity which is not affected by short-time variability as in the core. Furthermore, observations of the lobes also provide us intrinsic properties of the sources not obtained by the core. Usually, observed core power is degenerated quantity of the intrinsic power and the bulk Lorentz factor that is a function of the inclination and jet velocity. Now, owing to spectral bandpass of the SDSS (York et al., 2000), most of BAL quasars showing absorption trough at rest ultraviolet are found at high redshift ($z \sim 2$ for C IV BAL). At the redshift, because of difficulty in measuring apparent jet velocity directly, we cannot resolve the degeneracy in the core. In contrast, at the decelerated lobes Doppler beaming is not so strong that we can test the intrinsic difference between the two quasar populations.

In addition to the above, radio morphology also could represent environment of the sources. The paired lobes are usually found on the two opposite sides of the central engine, or the core (if detected). However, flux density or core-lobe distance are sometimes asymmetric in the sense that it cannot be explained only by projection effects (Saikia et al., 2003) which are Doppler beaming effect or aberration (Urry & Padovani, 1995). This kind of distortion is considered to be a result of interaction between jet and inhomogeneous ambient medium (Dallacasa et al., 2013). Although these asymmetric structure have been found in many galactic-scale sources (Arshakian & Longair, 2000; Stanghellini et al., 2005), effect of the intra-galactic scale interaction could also be confirmed in large-sized sources because radio morphology is known to be continuous from small to large scales (Saikia et al., 2003; Stanghellini et al., 2005). Now, in view of the evolution scheme, BAL quasars reside in the dense environment (Becker et al., 2000; Lípari & Terlevich, 2006) and thus are expected to show distorted morphology more often. Therefore, utilizing the asymmetry, we can test the hypothesis.

This chapter is organized as below. We describe our sample in Section 5.2. Then, rarity of FR II–BAL quasars will be presented in Section 5.3. Additionally, combined with statistical properties of the sample, we will discuss origin of the rarity and then the nature of BAL quasars in Section 5.4. Finally, conclusions are described in Section 5.5. Throughout this chapter, we adopt a cosmology consistent with WMAP results of $h = 0.71$, $\Omega_m = 0.27$, and $\Omega_\Lambda = 0.73$ (Komatsu et al., 2011).

■ 5.2 Sample Selection

We constructed our sample by using the quasar catalog (Schneider et al., 2010) from the seventh data release (DR7) of SDSS (Abazajian et al., 2009). Also we identified radio counterparts for each quasar by using the FIRST survey (Becker et al., 1995). In this study, we only use radio sources whose sidelobe probability in the FIRST survey is less than 0.1.

■ 5.2.1 Identification of FR II Quasars

In addition to a radio core which is supposed to contain a jet base, FR II sources have symmetrical radio lobes. While the core is positioned at optical position of quasars, it is not obvious that distant radio components are physically associated with the quasar based on images on the celestial sphere. Random radio sources could be misidentified as associated radio lobes. To avoid this and then to identify true radio lobes quantitatively and objectively, we adopted statistical method introduced by de Vries et al. (2006). Here, we briefly explain the procedure.

First, we identified a radio source located within 3 arcsec of each optical quasar as a radio core. Then, we listed all radio components positioned within 450 arcsec of each optical quasar, except for the identified core. In these components, both true radio lobes and random components are included. We would like to select the most probable candidates for a pair of radio lobes in each quasars. To select the candidates, we scored the likelihood of pairs of radio components in each quasar, w_{ij} , defined as

$$w_{ij} = \frac{\Psi_{ij}}{(i+j)^2}, \quad (5.1)$$

where i and j are the rank number of distance between the quasar and each radio source (the closest component to the quasar has $i = 0$, the next closet component has $i = 1$, etc.), and Ψ_{ij} is opening angle between i - and j -th radio components. With respect to each quasar, we selected the pair which has the largest w_{ij} as the most probable candidates for radio lobes. We also calculated diameter of the source, D_{ij} , which is a sum of separation between an optical quasar and each of the candidates.

Now, we have a list of the quasars with a pair of radio-lobe candidates. To select true FR II quasars from these sources, we examined the number distribution of D_{ij} and Ψ_{ij} . In

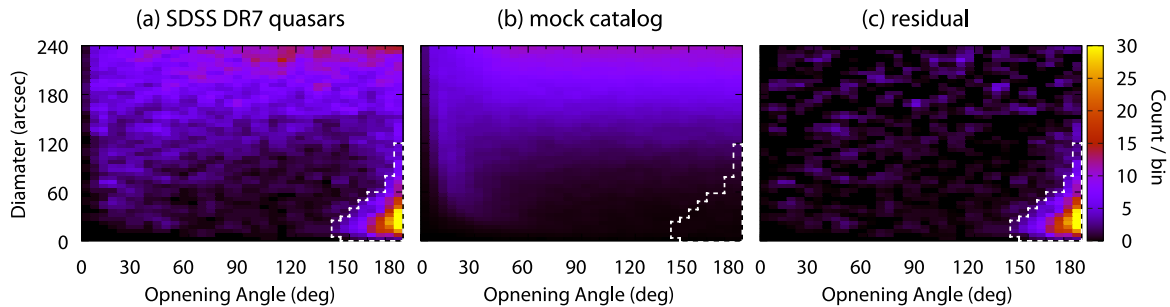


Figure 5.1 (a) Number distribution of opening angle and diameter of pair of candidate for radio lobes associated with each SDSS quasar. (b) That of mock catalog. Average of 40 trials is displayed. (c) Residual of (a) and (b). Size of the bin is $5 \text{ deg} \times 5 \text{ arcsec}$ for all maps. The white dotted lines in each map indicate pixels where we extract FR II quasars candidates.

Figure 5.1(a), "signal" is found in pixels of small D_{ij} and large Ψ_{ij} . Most of the sources contained in the signal could be true FR II quasars, but there might be contaminations of misidentified sources with random components. To estimate the amount of the contamination, we utilized mock catalog created by MANGLE (Hamilton & Tegmark, 2004) which contained the same number of random position as the quasars catalog from SDSS DR7. The procedure same as that for the SDSS quasars catalog was made for 40 mock catalogs with different seeds. Figure 5.1(b) shows stacked number distribution of D_{ij} and Ψ_{ij} produced by the mock catalog. The distribution of the mock catalog could correspond to the contamination by the random sources in Figure 5.1(a). Figure 5.1(c) is a residual of Figure 5.1(a) and (b), suggesting the mock catalogs were able to replicate the distribution other than the signal. In order to construct reliable FR II quasars catalog, we set range of D_{ij} and Ψ_{ij} (see Figure 5.1). As a result, 1,099 candidates for FR II quasars were selected. Inside the boundary shown in Figure 5.1, the ratio of number count in Figure 5.1(b) to Figure 5.1(a) is $\sim 2\%$. Thus, reliability of the 1,099 FR II candidates is $\sim 98\%$. Of the 1,099 candidates, there are 198 sources whose redshift is in the range of $1.68 \leq z \leq 4.93$. Then, the all sources at the redshift go through our visual inspection. In this step, we excluded the sources whose radio lobes have another optical counterpart (see Appendix B for the excluded sources). Consequently, 186 sources are identified as genuine FR II sources.

The above method can select the sources with radio components ordered in a line and closest to the optical positions of quasars objectively and quantitatively. However, though reliability of the catalog is $\sim 98\%$, completeness of the catalog is just $\sim 50\%$ as noted in de Vries et al. (2006). We note that the selection using Equation 5.1 might produce some bias related to radio morphology. For example, bending sources whose opening angle is much smaller than 180 deg could be missed in this method. This will be discussed in Section 5.4.1.

■ 5.2.2 Identification of BAL Quasars

We measured BI_0 (Equation 2.4; Gibson et al., 2009) of C IV for SDSS DR7 quasars at $1.68 \leq z \leq 4.93$, where entire absorption feature of high-velocity C IV BAL (25,000 to 0 km s^{-1}) is visible in the SDSS spectral bandpass (3800–9200 Å). The basic strategy used to fit the model is same as Gibson et al. (2008, 2009). We removed the effects of Galactic extinction using the Milky Way extinction curve of Pei (1992), and $E(B - V)$ provided by the dust maps of Schlegel et al. (1998). Then, we shifted the spectra to rest frame using the redshift in the SDSS quasars catalog (Schneider et al., 2010). Our continuum model is a power-law in which no intrinsic reddening is assumed (cf. Shen et al., 2011). We initially fitted regions that are generally free from strong absorption or emission features; 1250–1350, 1700–1800, 1950–2200, 2650–2710, and 2950–3700 Å (rest frame). We then iteratively fitted the continuum. In order to exclude strong absorption and emission features, at each step we ignored wavelength bins that deviated by $>3\sigma$ from the current fit. Next, we fitted Voigt profiles to the strongest emission lines expected in the spectrum of C IV $\lambda 1549$. Here, the wavelengths of the emission lines are allowed to vary in the fit. We fitted emission lines iteratively as well, ignoring at each step bins that were absorbed by more than 2.5σ from the continuum and the emission. After the initial automatic fits, BI_0 was calculated, where trough with $BI_0 > 0$ was identified as tentative BAL. Then, we visually inspected the automatic fits of the FR II sample which was described in Section 5.2.1. For non-FR II sources, we did not make visual inspection and just excluded not-well fitted sources. This does not affect our discussion (see Section 5.3.1 and Appendix C).

■ 5.3 Result

■ 5.3.1 Fraction of BAL quasars

Combined the FR II catalog and the BAL catalog, we identified 12 FR II–BAL quasars. Figure 5.2 shows spectra and images of the FR II–BAL quasars provided by SDSS and the FIRST survey. Table 5.1 and 5.2 show the optical and radio properties, respectively. While two sources were already reported by Gregg et al. (2006), the others are newly identified FR II–BAL quasars at $1.68 \leq z \leq 4.93$. Though Gregg et al. (2006) reported J0148–0819 as a FR II–BAL quasar at $z = 1.68$, we exclude the source from our FR II–BAL sample, because $z = 1.6797$ is reported in the quasars catalog from SDSS DR7 (Schneider et al., 2010). We identified J1439+4550 as a considerable candidate for a FR II quasar, but it needs further inspection. This is because there is a lack of any connection between the lobes and the central source, and the south-east lobe could become a pair with the nearest radio source at the south. However, there is also no competing contrary evidence. Therefore, we include the source in our sample.

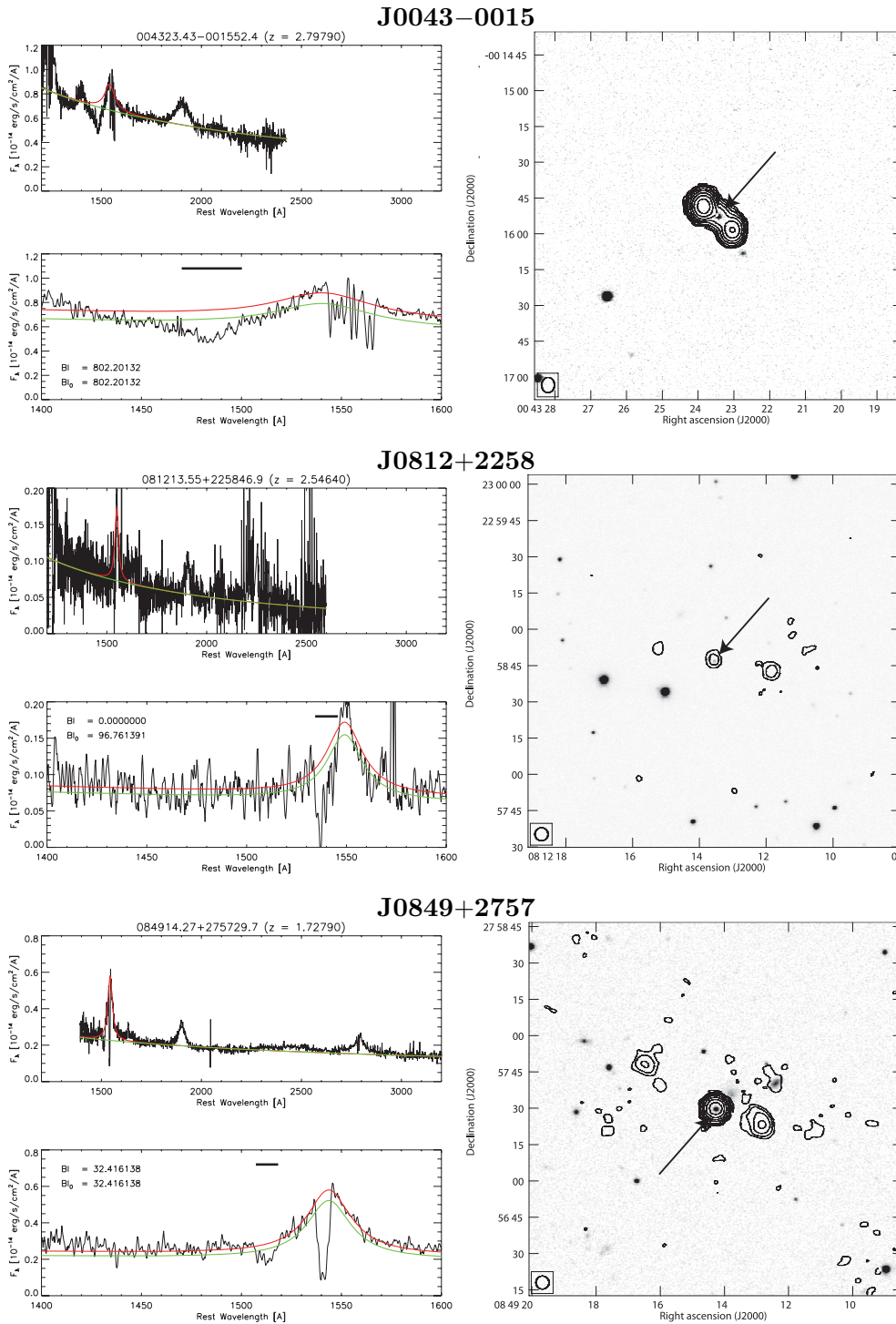


Figure 5.2 (left) SDSS spectra used to identify the C IV BAL. The bottom spectra are close-up of the C IV region. At the top, our model fit is indicated by green (continuum) and red (C IV emission line) lines. At the bottom, the model and 0.9 times of it are indicated by red and green lines, respectively. Thick black lines suggest absorption trough used to calculate BI_0 . (Right) SDSS r -band images of the FR II-BAL quasars overlaid by radio contours from the FIRST survey. The contour levels are $(-1, 1, 2, 4, 8, \dots) \times 0.45$ mJy beam $^{-1}$. Optical position of the quasars is indicated by black arrow.

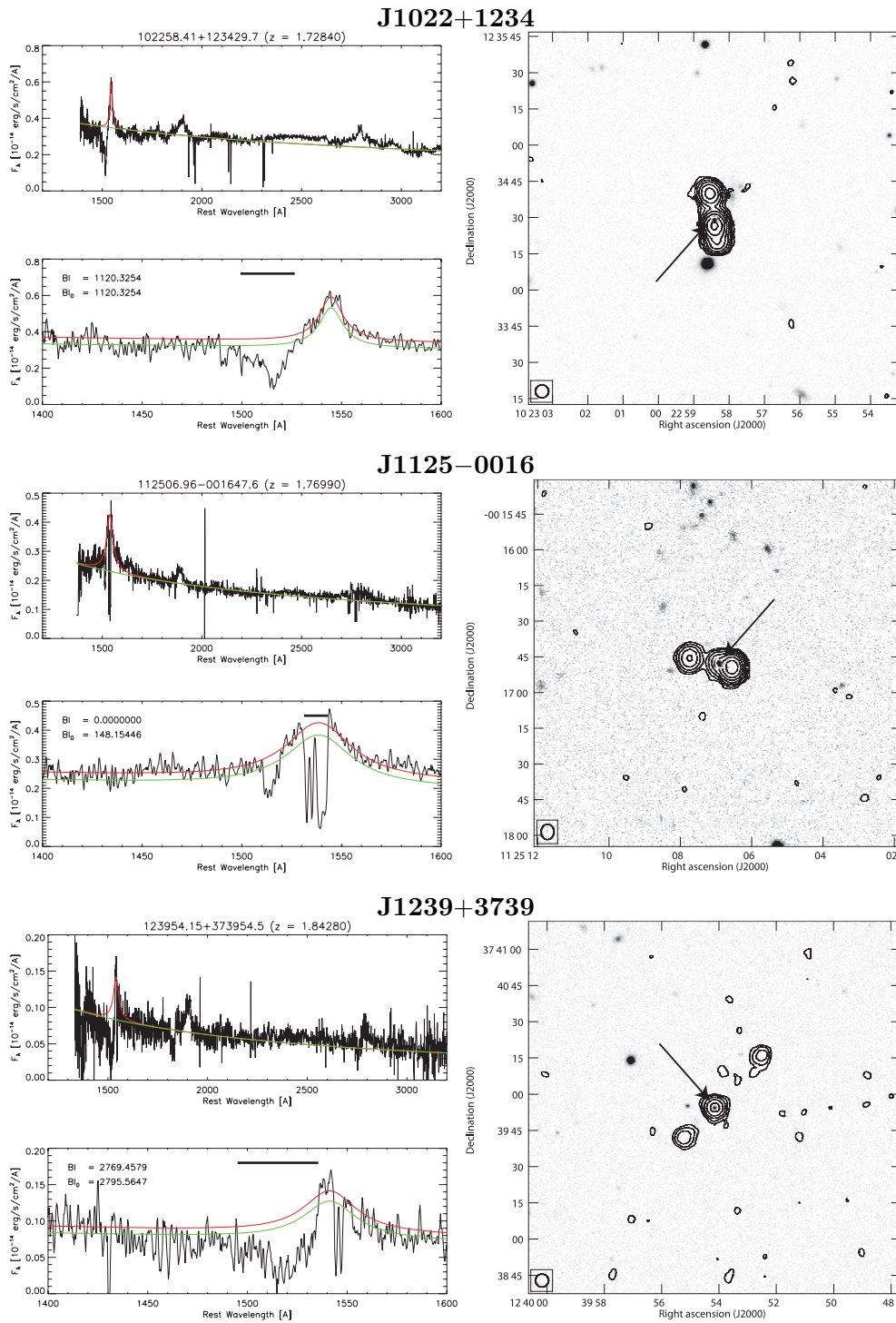
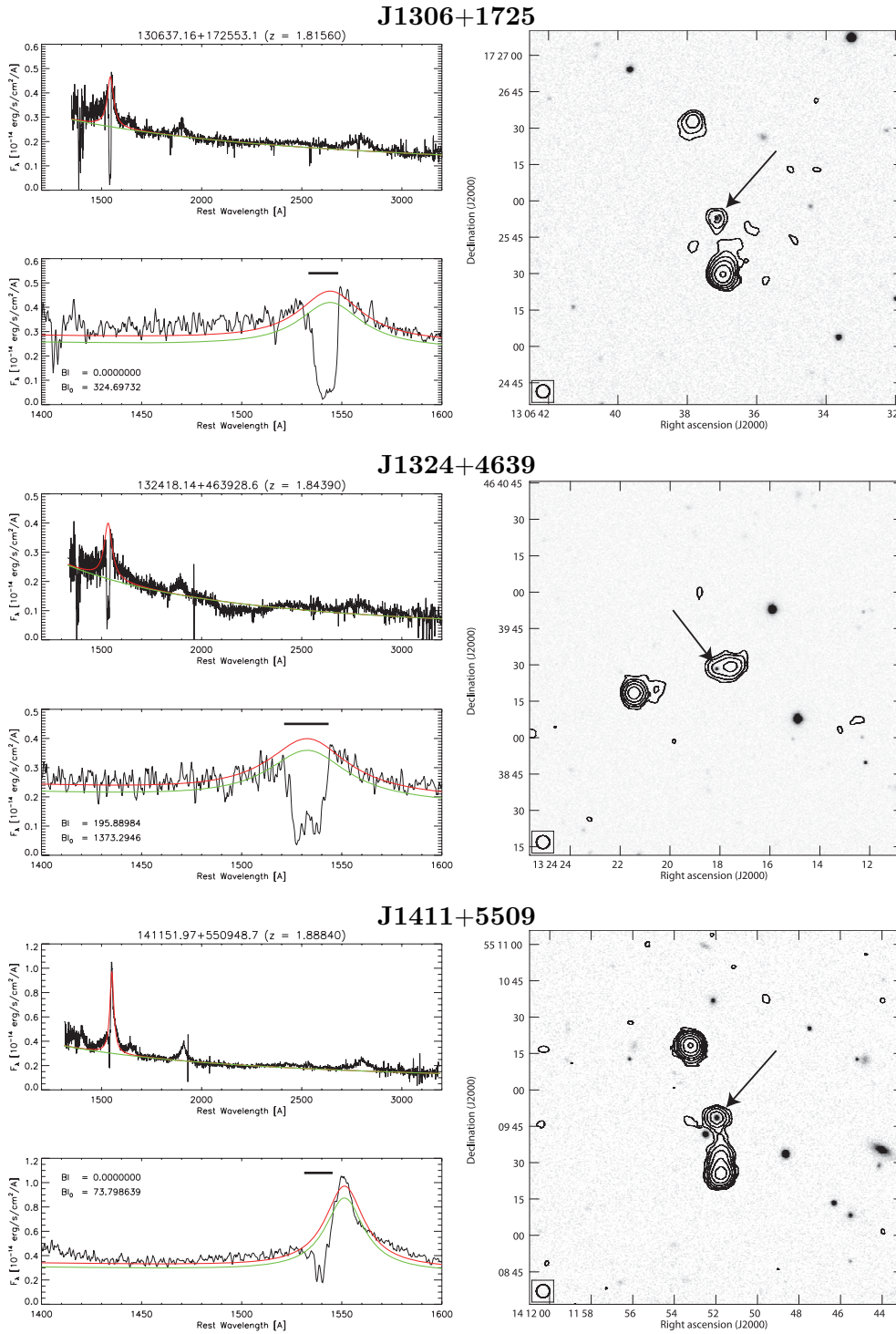


Figure 5.2 *Continued*

Figure 5.2 *Continued*

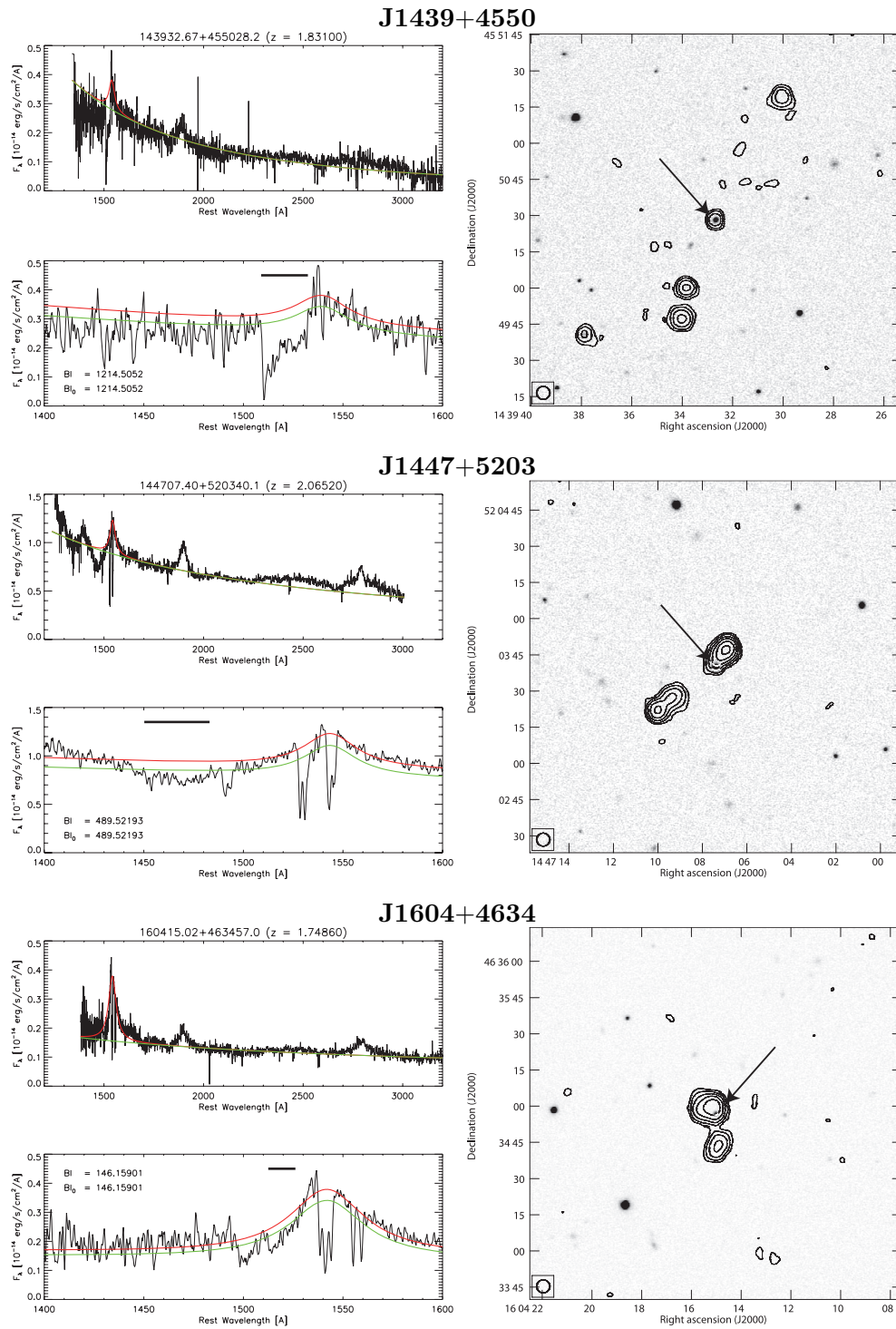


Figure 5.2 *Continued*

Table 5.3 shows the number and fraction of C IV BAL quasars in each quasar group at $1.68 \leq z \leq 4.93$. Uncertainties of the fraction are given by the standard deviation assuming normal distribution. BAL is shown in $6.4 \pm 1.8\%$ of the FR II sample. On another front, $17.4 \pm 0.2\%$ of total SDSS quasars at $1.68 \leq z \leq 4.93$ shows BAL. There is a factor (2.7 ± 0.7) of a difference in the fraction between the FR II sample and the total quasars sample. This estimation supports the result from Shankar et al. (2008) but is inconsistent with that from Gregg et al. (2006). This will be discussed in Section 5.4. Because we did not make a visual inspection of the optical spectra for non-FR II sources, their BAL fraction could be overestimated. However, significance of the rarity of FR II–BAL quasars does not change even in other BAL quasars catalog from SDSS (Trump et al., 2006; Gibson et al., 2009; Scaringi et al., 2009; Allen et al., 2011; Shen et al., 2011). The lack of the inspection does not affect following discussion (see Appendix C).

For a comparison, we also evaluate BAL fraction for quasars associated with a single radio component in the FIRST survey. Considering typical resolution of the FIRST survey (~ 5 arcsec), projected linear size of the single components is less than 40 kpc at the redshift. Now, though these distinct components could include young radio lobe (O’Dea, 1998), we call these counterparts ”core” for convenience. Out of 2,833 non FR II quasars associated with core, 558 sources ($19.7 \pm 0.7\%$) show C IV BAL. The fraction is significantly larger than that in the FR II sample. Therefore, rarity of BAL quasars is not characteristic of radio-loud quasars but that of large-sized FR II quasars.

We found six FR II–BAL quasars having the core resolved by the FIRST survey (J0812+2258, J0849+2757, J1239+3739, J1306+1725, J1411+5509, J1439+4550). There is a large difference in the fraction of BAL quasars between the FR II quasars with core and without core (Table 5.3). However, the findings of the core strongly depends on resolution and dynamics range of the observations. This difference could be biased. We do not discuss it further here.

■ 5.3.2 Radio Properties of FR II–BAL Quasars

Thanks to the large quasars sample from SDSS DR7, we have increased the number of FR II–BAL quasars. Then, we would like to make statistical comparisons of BAL and non-BAL quasars in the FR II sample. Figure 5.3 shows radio properties of the FR II quasars; number distributions of projected linear size, ℓ , opening angle, Φ , and lobe luminosities at 5 GHz, L_5 , are presented. Table 5.4 shows result of statistical tests for these values. In all cases, differences between BAL and non-BAL quasars in the FR II sample are not significant at 5% significance by a Kolmogorov-Smirnov (KS) test and a Wilcoxon rank sum (RS) test^a. In addition, Figure 5.5 shows number distributions of arm-length ratio, $R_D = D_2/D_1$, and

^asame with Mann-Whitney U test

Table 5.1. Optical Properties of FR II–BAL Quasars.

Object Name (1)	SDSS Name (SDSS J) (2)	Plate (3)	Fiber (4)	MJD (5)	z (6)	$\log M_{\text{BH}}/M_{\odot}$ (7)	$\log L_{\text{bol}}$ (erg s^{-1}) (8)	$\log \epsilon$ (9)	BI (km s^{-1}) (10)	BI_0 (km s^{-1}) (11)	v_{min} (km s^{-1}) (12)	v_{MAX} (km s^{-1}) (13)	Ref. (14)
J0043–0015	004323.43–001552.4	393	181	51794	2.798	10.2	47.18	–1.08	802.2	802.2	–9771	–15588	a,b,c,d,e
J0812+2258	081213.55+225846.9	1584	582	52943	2.546	8.1	46.22	0.01	0.0	96.8	–989	–3182	c
J0849+2757	084914.27+275729.7	1932	408	53350	1.728	9.7	46.75	–1.02	32.4	32.4	–6267	–8422	b,c,e
J1022+1234	102258.41+123429.7	1746	147	53062	1.728	9.5	46.97	–0.65	1120.3	1120.3	–4695	–9947	b,c,d,e
J1125–0016	112506.96–001647.6	281	225	51614	1.770	10.2	46.69	–1.61	0.0	148.2	–1454	–3780	a,c,e
J1239+3739	123954.15+373954.5	2000	181	53495	1.843	8.9	46.27	–0.76	2769.5	2795.6	–2949	–10773	b,c,e
J1306+1725	130637.16+172553.1	2603	154	54479	1.816	9.8	46.82	–1.07	0.0	324.7	–495	–3375	e
J1324+4639	132418.14+463928.6	1461	638	53062	1.844	10.1	46.54	–1.62	195.9	1373.3	–1419	–5716	c,e
J1411+5509	141151.97+550948.7	1324	582	53088	1.888	9.6	46.80	–0.92	0.0	73.8	–1036	–3775	b,e
J1439+4550	143932.67+455028.2	1675	317	53466	1.831	9.0	46.46	–0.63	1214.5	1214.5	–3559	–8094	c,d,e
J1447+5203	144707.40+520340.1	1328	369	52786	2.065	10.3	47.14	–1.25	489.5	489.5	–13101	–19433	a,e
J1604+4634	160415.02+463457.0	813	172	52354	1.749	9.7	46.60	–1.18	146.2	146.2	–4765	–7402	a

Note. — Column 1: object name in this Chapter. Column 2: object name in the SDSS DR7. Column 3: spectroscopic plate number. Column 4: spectroscopic fiber number. Column 5: MJD of spectroscopic observation. Column 6: redshift. Column 7: mass of black hole Column 8: bolometric luminosity. Column 9: Eddington ratio. Column 10: balmicity index. Column 11: modified balmicity index. Column 12: C IV minimum velocity. Column 13: C IV maximum velocity. Column 14: references where the BAL quasar appears in the literature.

References. — a: Trump et al. 2006, b: Gibson et al. 2009, c: Scaringi et al. 2009, d: Allen et al. 2011, e: Shen et al. 2011

Table 5.2. Radio Properties of FR II–BAL Quasars.

Object Name	z	l (kpc arcsec $^{-1}$)	Φ (deg)	D_1 (arcsec)	D_2 (arcsec)	ℓ (kpc)	S_1 (mJy)	S_2 (mJy)	$\log L_5$ (erg s $^{-1}$ Hz $^{-1}$)	Ref.
(1)	(2)	(3)	(4)	(5)	(6)	(7)	(8)	(9)	(10)	(11)
J0043–0015	2.798	8.1	167	7.4	7.4	119	43.7	114.4	34.5	a
J0812+2258	2.546	8.2	178	23.7	23.9	392	1.0	3.2	32.8	
J0849+2757	1.728	8.6	165	19.5	34.5	467	7.8	4.5	32.9	
J1022+1234	1.728	8.6	167	3.4	10.4	119	94.0	24.7	33.8	
J1125–0016	1.770	8.6	173	6.1	11.9	155	55.4	10.1	33.6	
J1239+3739	1.843	8.6	177	17.6	28.7	399	4.3	3.5	32.7	
J1306+1725	1.816	8.6	172	23.3	40.4	549	23.2	5.0	33.3	
J1324+4639	1.844	8.6	171	4.9	35.5	348	10.8	13.0	33.2	
J1411+5509	1.888	8.6	164	22.6	31.5	465	34.2	34.2	33.7	
J1439+4550	1.831	8.6	175	30.6	57.8	762	4.7	4.6	32.8	
J1447+5203	2.065	8.5	155	7.5	22.5	256	26.6	8.0	33.5	a
J1604+4634	1.749	8.6	146	3.0	13.5	143	25.0	8.1	33.3	

Note. — Column 1: object name in this Chapter. Column 2: redshift. Column 3: linear scale corresponding to 1 arcsec. Column 4: opening angles of between pair of radio lobes. Column 5, 6: distance between optical quasars and radio lobes. Column 7: projected linear size, where $\ell = (D_1 + D_2)/l$. Column 8, 9: flux densities of radio lobes at 1.4 GHz. Column 10: specific luminosity at 5 GHz assuming spectral index of $\alpha = -0.7$. Column 11: references where the FR II–BAL quasar appears in the literature.

References. — a: Gregg et al. 2006

Table 5.3. Fraction of BAL quasars from SDSS DR7.

Quasar Group	BAL / all	fraction (%)
Total quasars	7134 / 40972	17.4 ± 0.2
...radio detected	570 / 3019	18.9 ± 0.7
.....FR II	12 / 186	6.4 ± 1.8
.....without core	6 / 54	11.1 ± 4.3
.....with core	6 / 132	4.6 ± 1.8
.....non FR II with core	558 / 2833	19.7 ± 0.7
...not detected at radio	6564 / 37953	17.3 ± 0.2

flux density ratio, $R_S = S_2/S_1$, between BAL and non-BAL quasars, where D and S are core-lobe distance and flux density, respectively. As shown in Figure 5.4, the indices of 1 and 2 represent the near and the far lobes on the celestial sphere, respectively. Assuming intrinsic axisymmetry and constant velocity, β , of unabsorbed steep-spectrum lobes, both of the ratios reflect inclination of the jet axis to the line of sight, θ , as

$$R_D = \frac{1 + \beta \cos \theta}{1 - \beta \cos \theta}, \quad (5.2)$$

and

$$R_S = \left(\frac{1 + \beta \cos \theta}{1 - \beta \cos \theta} \right)^{3-\alpha}, \quad (5.3)$$

where α is spectral index of the lobes (Blandford & Konigl, 1979; Urry & Padovani, 1995). In both ratios, the KS test and the RS test do not suggest significant differences between BAL and non-BAL quasars in the FR II sample at 5% significance level (Figure 5.5 and Table 5.4). Moreover, we also do not find a significant difference in R_S/R_D between the two samples. This will be discussed in Section 5.4.2.

■ 5.3.3 Optical Properties of FR II–BAL Quasars

We made a statistical comparison of BAL and non-BAL quasars in the FR II sample also using the SDSS data provided by Shen et al. (2011). Figure 5.6 shows number distributions of optical bolometric luminosity, L_{bol} , black hole mass, M_{BH} , and Eddington ratio, ϵ , of the FR II sample. Of these physical parameters, we found a difference in M_{BH} by the KS test and the RS test in 5% significance level. Black hole mass of FR II–BAL quasars could be larger than that of FR-II non-BAL quasars. Moreover, Eddington ratio also shows a significant difference between the two samples by the RS test (but not by the KS test) at 5% significance. In contrast, the bolometric luminosity distributions are comparable. Here, we note that M_{BH} and ϵ are not independent of each other ($\epsilon \propto L_{\text{bol}}/M_{\text{BH}}$); one could be induced variable of the other.

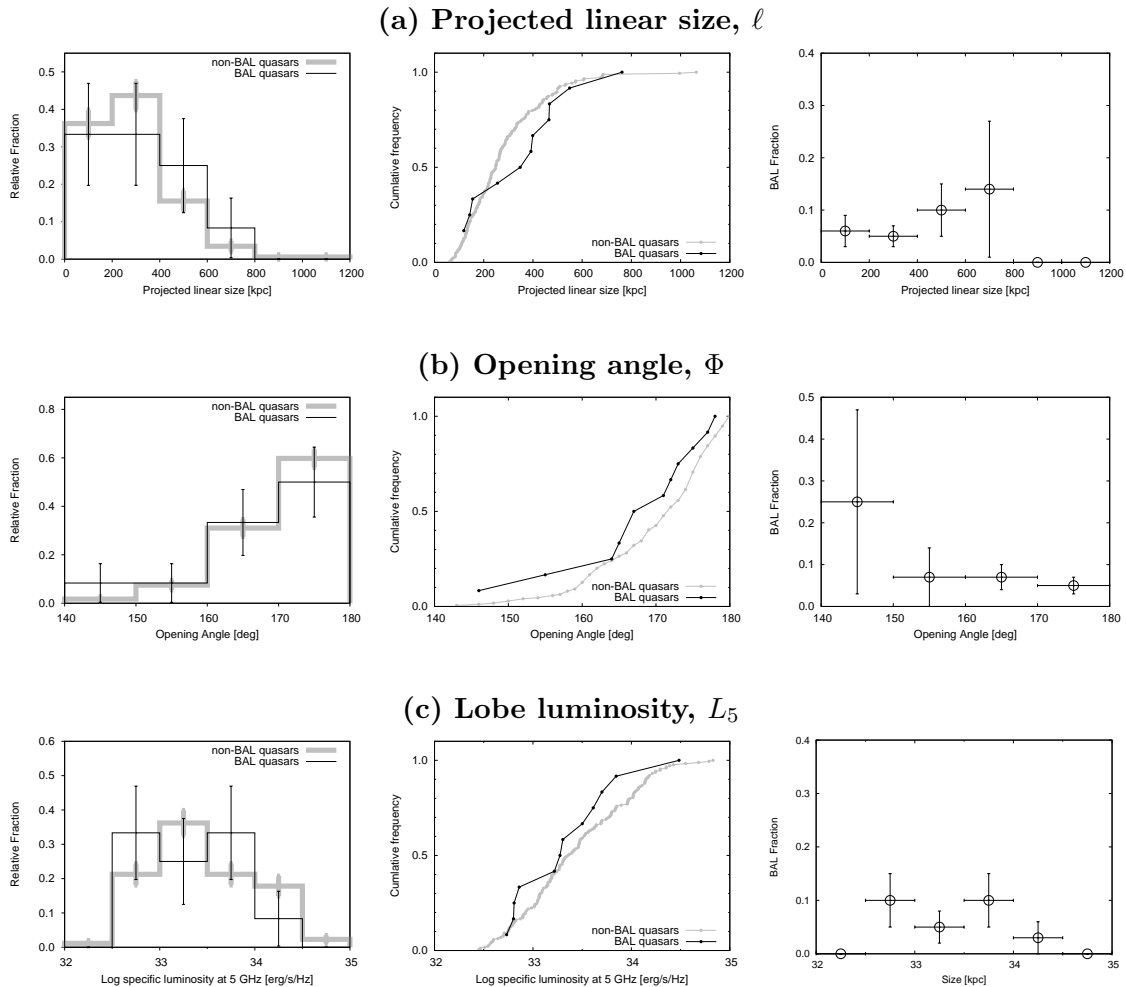


Figure 5.3 (a) Projected linear size, ℓ , (b), opening angle, Φ , and (c) radio luminosity, L_5 , distributions of BAL and non-BAL quasars in the FR II sample. On the left to right at each column, relative frequency, cumulative frequency, and fraction of BAL quasars as a function of each parameter are displayed. Error bars at each panel are given by 1σ uncertainty of the fraction assuming normal distribution. The KS test gives $D_{\text{KS}} = 0.319, 0.193,$ and 0.172 with a corresponding probability that the two distributions are from the same parent population of $p = 0.204, 0.800,$ and 0.892 for $\ell, \Phi,$ and L_5 , respectively. The RS test gives $Z_{\text{RS}} = 1260, 867,$ and 954 with a corresponding probability that the two distributions are from the same parent population of $P_{\text{RS}} = 0.233, 0.327,$ and 0.620 for $\ell, \Phi,$ and L_5 , respectively.

5.4 Discussion

5.4.1 How Rare are FR II–BAL Quasars?

In Section 5.3.1, we clarified that the number of BAL quasars in the FR II sample is roughly 2–3 times less common than that in the total SDSS sample (Table 5.3). The difference is consistent with Shankar et al. (2008) but smaller than Gregg et al. (2006). Assuming that appearances of C IV BAL in SDSS ($\sim 16\%$; Reichard et al. 2003) and large-sized FR II sources in the FIRST survey ($\sim 2.8\%$; de Vries et al. 2006) are independent and do no change

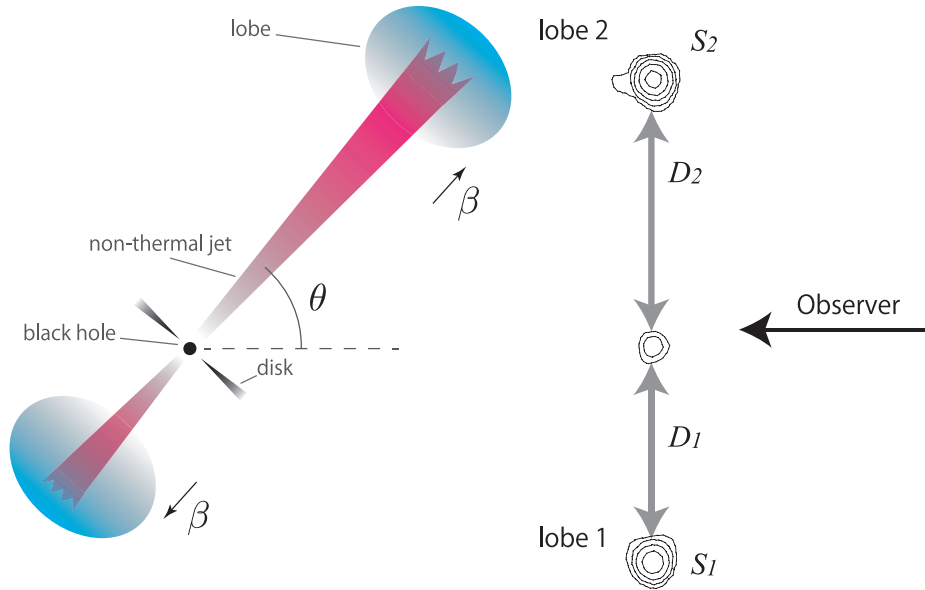


Figure 5.4 Definition of component's name and corresponding geometry under the ideal condition. To take arm-length ratio, $R_D = D_2/D_1$, and flux density ratio, $R_S = S_2/S_1$, we define the nearer and the further lobes on celestial sphere as lobe 1 and 2, respectively. Assuming intrinsic axisymmetry and constant-velocity, β , of unabsorbed steep-spectrum lobes, the lobe 1 and 2 are receding and approaching components. We define θ as the inclination of the jet axis with respect to the line of sight.

with redshift, Gregg et al. (2006) claimed that detection rate of the FR II–BAL quasars at $1.7 \leq z \leq 3.6$ is 10 times smaller than they expected. While at the moment no strong redshift dependence is found for the observed fraction of BAL quasars (e.g., Shen et al., 2008), detection of FR II sources however should strongly depend on redshift. Usually, the higher the redshift is, the more diffuse the steep-spectrum lobes are. This is because at high redshift we observe the lobes at high rest frequency. Thus, if we fix observed frequency and image noise level (1.4 GHz and ~ 0.15 mJy beam $^{-1}$ in the FIRST survey), detection rate of the radio lobes decreases with increasing redshift. The fraction of FR II quasars used in Gregg et al. (2006) is estimated with SDSS quasars at entire redshift range. This assumption should be overestimated at the high redshift where C IV BAL is detected. Therefore, our estimation limited to the high redshift is more accurate than that by Gregg et al. (2006).

As noted in Section 5.2.1, our identification of FR II quasars using Equation 5.1 might produce some bias related to radio morphology; bending sources can be missed. Now, our result is consistent with that of Shankar et al. (2008) who identified BAL quasars associated with multiple radio components within 30 arcsec. This method is not affected by opening angles of the radio sources. Thus, the similarity indicates our result was not biased by the bent of the sources.

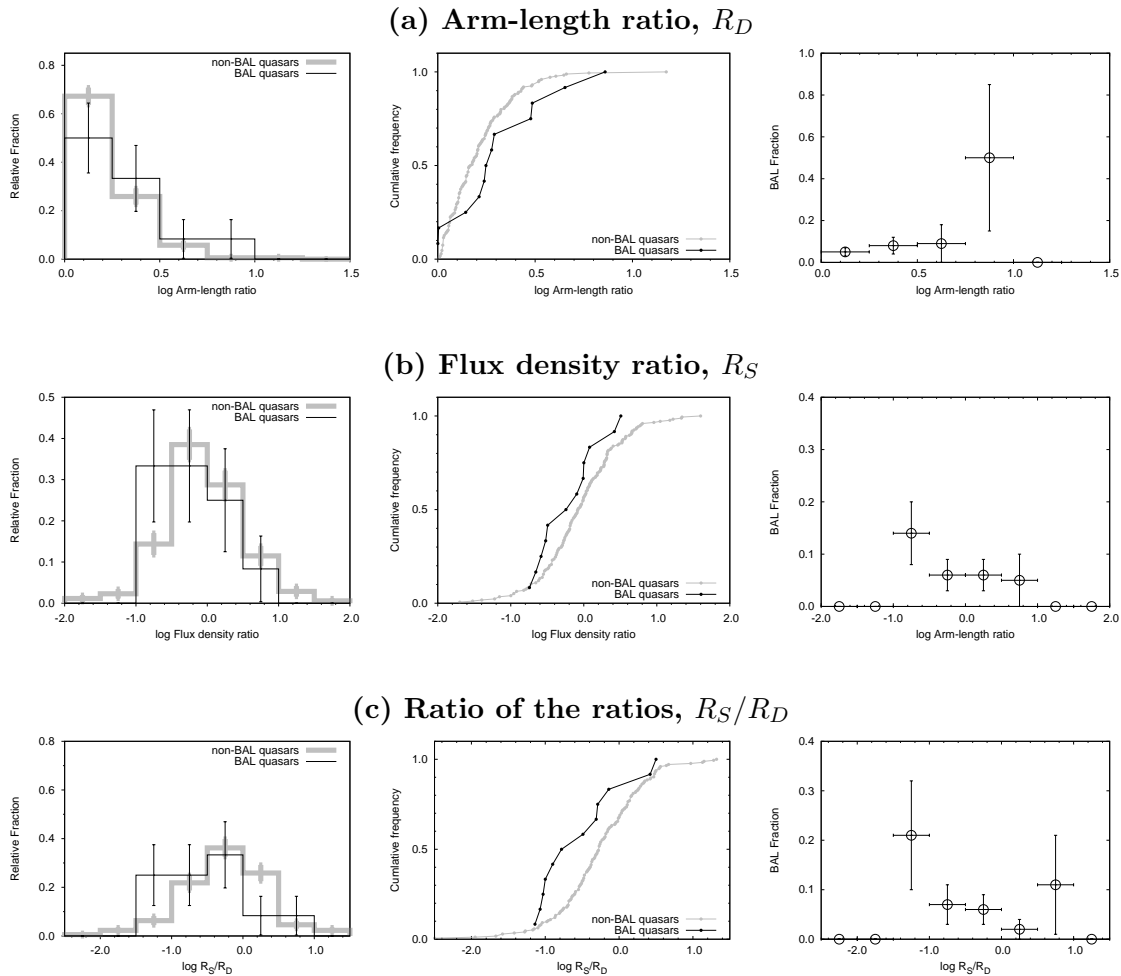


Figure 5.5 (a) Arm-length ratio, R_D , and (b) flux density ratio, R_S , distribution of BAL and non-BAL quasars in the FR II sample same as Figure 5.4. Error bars at each panel are given by 1σ uncertainty of the fraction assuming normal distribution. The KS test gives $D_{KS} = 0.353$, 0.233 , and 0.345 with a corresponding probability that the two distributions are from the same parent population of $P_{KS} = 0.121$ and 0.577 , and 0.139 for R_D , R_S , and R_S/R_D , respectively. The RS test gives $Z_{RS} = 1331$, 860 , and 747 with a corresponding probability that the two distributions are from the same parent population of $P_{RS} = 0.113$, 0.309 , and 0.100 for R_D , R_S , and R_S/R_D , respectively.

5.4.2 The Origin of the Rarity of FR II–BAL Quasars

We have confirmed that the rarity of FR II–BAL quasars mentioned by Gregg et al. (2006) itself is true. Since the rarity has been one of the bases for the evolution scheme, it is important to consider why it happens for understanding BAL quasars. Combined with the statistical data presented in Section 5.3.2 and 5.3.3, we would like to discuss the origin of the rarity and then the nature of BAL quasars.

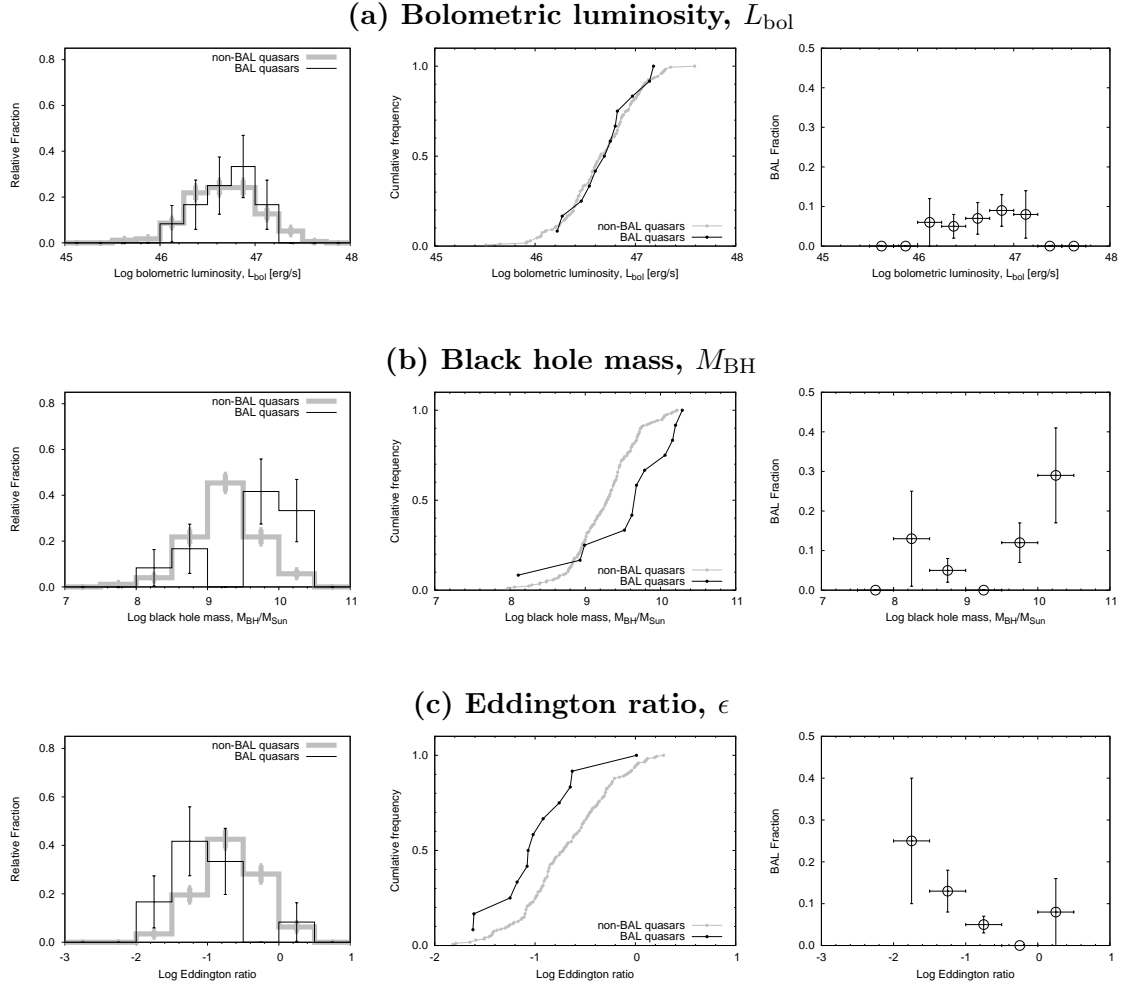


Figure 5.6 (a) Bolometric luminosity, L_{bol} , (b) black hole mass, M_{BH} , and (c) Eddington ratio, ϵ , distributions of the FR II sample same as Figure 5.4. Error bars at each panel are given by 1σ uncertainty of the fraction assuming normal distribution. The KS test gives $D_{\text{KS}} = 0.138, 0.480, \text{ and } 0.371$ with a corresponding probability that the two distributions are from the same parent population of $P_{\text{KS}} = 0.983, 0.011, \text{ and } 0.091$ for $L_{\text{bol}}, M_{\text{BH}}, \text{ and } \epsilon$, respectively. The RS test gives $Z_{\text{RS}} = 1104, 1487, \text{ and } 646$ with a corresponding probability that the two distributions are from the same parent population of $P_{\text{RS}} = 0.742, 0.014, \text{ and } 0.027$ for $L_{\text{bol}}, M_{\text{BH}}, \text{ and } \epsilon$, respectively.

Orientation effect

Our FR II sample is not selected by intrinsic linear size, L , but is based on projected linear size, ℓ . FR II quasars whose diameter is more than the resolution of the FIRST survey (~ 5 arcsec corresponding to $\ell \gtrsim 40$ kpc at $z \sim 2$) are selected. Now, number distribution of projected linear size depends on that of inclination of the sources. Therefore, our FR II sample could not be homogeneous in terms of the inclination. Here, we consider the possibility that the rarity is explained by this orientation effect.

First, we assume the geometry as in Figure 5.7, where inclination of the jet axis to the line of sight is θ . Here, maximum inclination of quasars is defined as $\theta = \theta_{\text{C}}$, and all of the

Table 5.4. Result of Statistical Comparison in the FR II Sample.

Measurement (1)	D_{KS} (2)	P_{KS} (3)	Z_{RS} (4)	P_{RS} (5)
ℓ	0.319	0.204	1260	0.233
Φ	0.193	0.800	867	0.327
L_5	0.172	0.892	954	0.620
R_D	0.353	0.121	1331	0.113
R_S	0.233	0.577	860	0.309
R_S/R_D	0.345	0.139	747	0.100
L_{bol}	0.138	0.983	1104	0.742
M_{BH}	0.480	0.011	1487	0.014
ϵ	0.371	0.091	646	0.027

Note. — Column 1: physical parameters to be compared. Column 2–3: the KS test statistic, D_{KS} , and the corresponding p -value, P_{KS} . Column 4–5: the RS test statistic, Z_{RS} , and the corresponding p -value, P_{RS} .

quasars viewed from inclination of $\theta_{\text{min}} \leq \theta \leq \theta_{\text{MAX}}$ are BAL quasars. In addition, showing FR II morphology and having the disk wind to show BAL are assumed to be independent. Assuming power-law distribution of L , number density of the FR II sources, d^2n , having specific values of L and θ , is given by

$$d^2n \propto \begin{cases} L^{-a} dL \sin \theta d\theta & (L \leq L_{\text{MAX}}) \\ 0 & (L > L_{\text{MAX}}), \end{cases} \quad (5.4)$$

where L_{MAX} and a are maximum value of L and a positive constant ($a > 0$), respectively. Substituting $\ell = L \sin \theta$, we get

$$d^2n \propto \begin{cases} \ell^{-a} d\ell \sin^a \theta d\theta & (\ell \leq L_{\text{MAX}} \sin \theta) \\ 0 & (\ell > L_{\text{MAX}} \sin \theta). \end{cases} \quad (5.5)$$

Now, the angular distribution of FR II sources based on projected linear size, $f(\theta)$, is defined by $\int_{\ell} d^2n = f(\theta) d\theta$. Then, we get

$$\begin{aligned} f(\theta) &\propto \sin^a \theta \int_{\ell_{\text{min}}}^{L_{\text{MAX}} \sin \theta} \ell^{-a} d\ell \\ &\propto \begin{cases} L_{\text{MAX}}^{1-a} \sin \theta - \ell_{\text{min}}^{1-a} \sin^a \theta & (a \neq 1) \\ \ln \frac{L_{\text{MAX}} \sin \theta}{\ell_{\text{min}}} \cdot \sin \theta & (a = 1), \end{cases} \end{aligned} \quad (5.6)$$

using equation 5.5, where ℓ_{min} is a minimum value of ℓ in the sample. We set a constant factor in $f(\theta)$ to satisfy

$$\int_{\ell=\ell_{\text{min}}}^{\ell=L_{\text{MAX}} \sin \theta} \int_{\theta=0}^{\theta=\theta_{\text{C}}} d^2n = \int_0^{\theta_{\text{C}}} f(\theta) d\theta = 1. \quad (5.7)$$

Then, we get the fraction of BAL quasars, n , whose inclination is in the range of $\theta_{\min} \leq \theta \leq \theta_{\max}$ as

$$n(\text{FR II}) = \int_{\theta_{\min}}^{\theta_{\max}} f(\theta) d\theta, \quad (5.8)$$

for the FR II sample and

$$n(\text{total}) = \int_{\theta_{\min}}^{\theta_{\max}} \sin \theta d\theta. \quad (5.9)$$

for the total quasars sample from SDSS DR7. Then, the rarity of BAL quasars in the FR II sample is given by

$$r = \frac{n(\text{FR II})}{n(\text{total})}. \quad (5.10)$$

Figure 5.8 shows $f(\theta)$ and r in the case of $\ell_{\min} = 50$ kpc and $L_{\max} = 2$ Mpc. Observationally, $n(\text{total}) = 0.17$ was obtained based on our identification of BAL (see Table 5.3). The case for $\theta_C = 90, 75, 60, 45$ deg and $a = 0.5, 1.0, 2.0, 3.0, 4.0, 5.0$ are shown. We note that θ_{\min} and θ_{\max} are not independent with each other because $n(\text{total}) = 0.17$ is assumed. The left panels of Figure 5.8 suggest that the sample is populated with relatively edge-on sources if a is large enough. Now, the orientation scenario is suspicious considering theoretical model of the disk wind. Using Equation 5.5, we get projected linear size distribution, $g(\ell)$, defined by $\int_{\theta} d^2n = g(\ell) d\ell$, as

$$g(\ell) \propto \begin{cases} \ell^{-a} \int_{\arcsin \ell/L_{\max}}^{\theta_C} \sin^a \theta d\theta & (\ell \leq L_{\max} \sin \theta_C) \\ 0 & (\ell > L_{\max} \sin \theta_C). \end{cases} \quad (5.11)$$

Figure 5.9 shows $\log[g(\ell)/\ell^{-a}]$, which suggests that, at large ℓ , slope of $g(\ell)$ becomes steeper than intrinsic linear size distribution. Then, from projected linear size distribution at the large size end in Figure 5.3, we obtained tentative value of $a \sim 2$. Based on numerical simulation of line-driven disk wind (Nomura et al., 2013), $\theta \sim 50$ deg is obtained for viewing angles of BAL quasars. Then, Figure 5.8 shows $r \gtrsim 1$ in any cases, which does not coincide with that observed ($r \sim 1/3$). Therefore, some modifications are expected in theoretical model of line-driven wind or the simple orientation scheme assumed here is not valid.

Environment

To explain the rarity of FR II–BAL quasars, an evolution scenario is proposed by Gregg et al. (2006): the BAL phenomenon occurs in an early phase before enveloping gas and dust around the quasar break out, and thus frustration by the obscuring material in the host galaxy is the main cause of the rarity (see also Becker et al., 2000). If the sources are in the dense environment, distorted or asymmetric morphology is expected to be observed

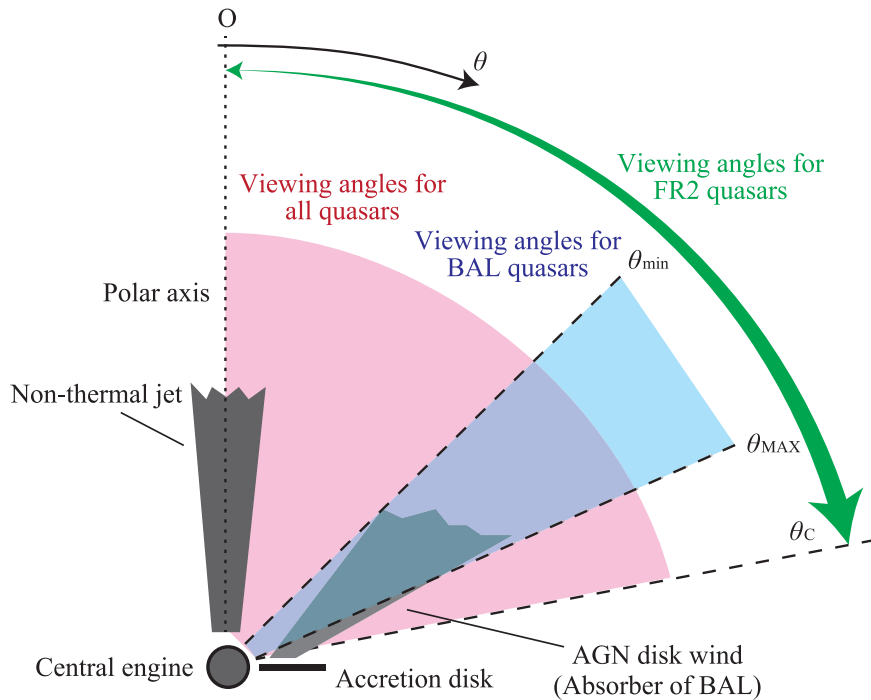


Figure 5.7 Schematic picture of the geometry assumed for the orientation scheme. We define θ as inclination of the jet. Maximum inclination of quasars is defined as $\theta = \theta_C$. All of the quasars viewed from inclination of $\theta_{\min} \leq \theta \leq \theta_{\max}$ are BAL quasars.

(Arshakian & Longair, 2000; Stanghellini et al., 2005; Dallacasa et al., 2013). Although all of the quasars in our sample are inter-galactic scale sources, effect of the galactic scale environment could also be confirmed because radio morphology is known to be continuous from small to large scales (Saikia et al., 2003; Stanghellini et al., 2005). In Section 5.3.2, we found no clear difference in Φ between the BAL and non-BAL quasars (Figure 5.3). This implies that the BAL and non-BAL quasars live in similar environments. Thus, we do not find the evidence for the evolution scheme.

The environment is also evaluated using flux density ratio, R_S , and arm-length ratio, R_D . Figure 5.10 shows the distributions of R_S as a function of R_D . As found from Equation 5.2 and 5.3, $R_S = R_D^{3-\alpha}$ is obtained assuming (i) constant advancing speed, (ii) no curvature in the spectrum (i.e., no absorption), and (iii) axisymmetry of the lobes. If all of the assumptions are valid, the sources should be ordered in a line on the R_S - R_D plane, but in reality they do not (Figure 5.10). This scatter suggests the interaction between the lobes and ambient medium (Dallacasa et al., 2013). In Section 5.3.2, we found no significant difference in R_D/R_S between the BAL and non-BAL quasars (Figure 5.5). The similarity also implies that the environment might be similar in both quasars in the FR II sample. This is consistent with consideration from the number distributions of Φ .

Because our analysis of radio morphology is focused on FR II quasars whose size is more

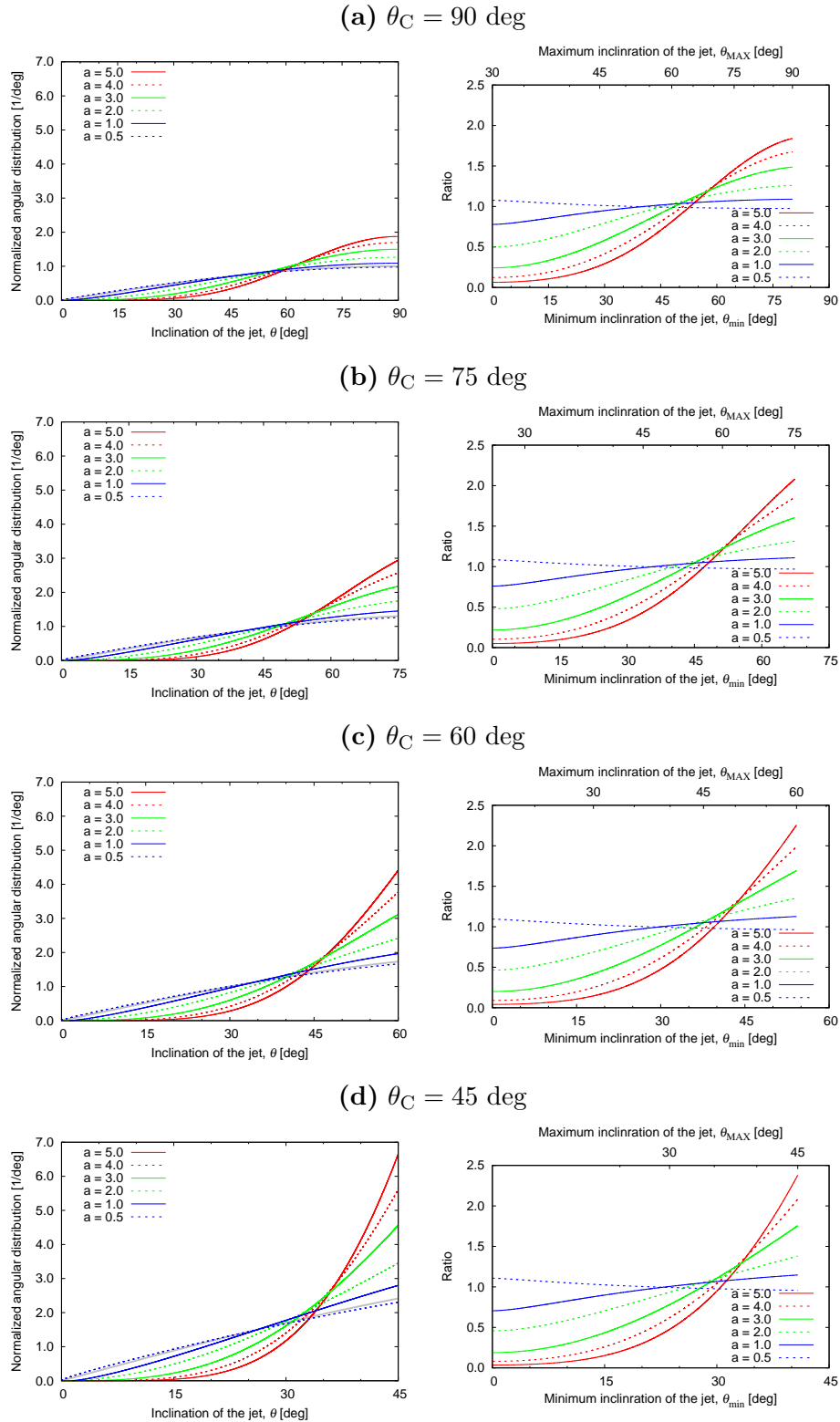


Figure 5.8 (right) Expected angular distribution of the FR II sample, $f(\theta)$, in case of $\ell_{\min} = 50$ kpc, $L_{\max} = 2$ Mpc. Gray lines indicate the isotropic angular distribution proportional to $\sin \theta$ in case that the selection by projected linear size is not made. (left) The rarity of FR II BAL quasars, r , same as the right panel. From top to bottom, the case of $\theta_C = 90, 75, 60,$ and 45 deg are shown.

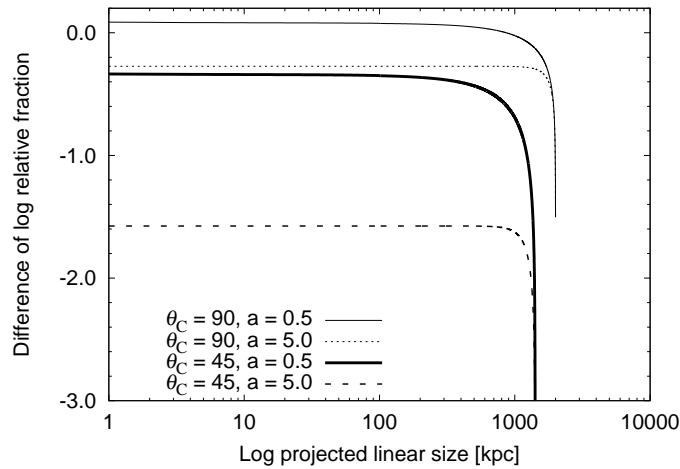


Figure 5.9 Expected projected linear size distribution of the FR II sample, $g(\ell)$, in case of $\ell_{\min} = 50$ kpc, $L_{\max} = 2$ Mpc. We plot difference in relative fraction between projected and intrinsic linear size, $\log g(\ell)/\ell^{-a}$, for $(\theta_C, a) = (90, 0.5)$, $(90, 5.0)$, $(45, 0.5)$, and $(90, 5.0)$. From the figure, we get $\log g(\ell)/\ell^{-a} < 0$ regardless of a and θ_C because dependency of $g(\ell)$ on these parameters is monotone.

than galactic scale (i.e. $\gtrsim 100$ kpc), the result also gives an insight into the large-scale environment. In general, radio galaxies with large bent (i.e., small Φ) are associated with clusters or groups (Blanton et al., 2000, 2001; Edwards et al., 2010). If BAL quasars live in a cluster, FR II–BAL quasars are expected to have distorted morphology (e.g., Hintzen & Scott, 1978), but in practice they do not. Now, Shen et al. (2008) suggested that clustering strengths of BAL and non-BAL quasars in SDSS are similar. Thus, our result is consistent with Shen et al. (2008).

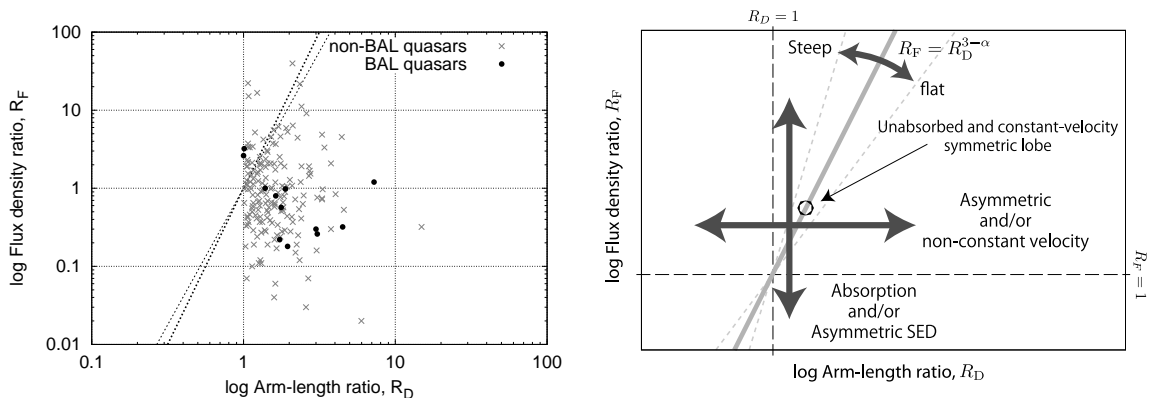


Figure 5.10 (left) Arm-length ratio, R_D , and flux-density ratio, R_S , distribution of FR II quasars. Black circles and gray crosses represent BAL and non-BAL quasars, respectively. Thin and thick dotted lines indicate the relation between R_D and R_S for unabsorbed and constant-velocity symmetric lobes ($R_S = R_D^{3-\alpha}$) of $\alpha = -0.5$ and $\alpha = -1.0$, respectively. (right) Schematic picture of how to interpret the distribution. In the ideal case, $R_S = R_D^{3-\alpha}$ is satisfied. However, if these condition disrupt, distribution of (R_S, R_D) is scattered.

Central engine

Observationally, correlation between the core and total radio power was confirmed. The correlation suggests that lobes are fueled by the core through collimated non-thermal jet (Giovannini et al., 1988, 1990, 2001). To evolve to large-sized radio sources, the core activity should continue for a long period ($\sim 10^7$ yrs for sources with ~ 100 kpc assuming an advance speed of ~ 0.1 ; e.g., Carilli et al. 1991). Thus, lobes power of FR II quasars is a good indicator of total activity of the core during its lifetime. Moreover, because Doppler beaming is not significant at the decelerated lobes, observed luminosity of the lobes is not affected by the orientation effect. In Section 5.3.2, we did not find the significant difference (Figure 5.3) in projected linear size, ℓ , and lobe luminosity, L_5 , between the BAL and non-BAL quasars in the FR II sample. This suggests that the central engine of BAL and non-BAL quasars can be similarly active in terms of the strength and period.

In contrast to the above argument, in Section 5.3.3 we have found the significant differences in the black hole mass and the Eddington ratio (Table 5.4 and Figure 5.6). BAL quasars in the FR II sample show larger black hole mass and lower Eddington ratio than the non-BAL quasars. The black hole mass and the Eddington ratio were obtained with line width of Mg II and C IV for the sources at $0.7 \leq z < 1.9$ and $1.9 \leq z$, respectively (Shen et al., 2011). Because measurement of the width can be affected by absorption feature like BAL, the difference in the black hole mass and the Eddington ratio might not be an intrinsic one. Moreover, to reduce black hole mass from the line width, it needs scaling factor depending on the assumed structure of the broad line region. If the structure is not isotropic and BAL quasars have restricted viewing angles, there could be a systematic difference in the scaling factor between BAL and non-BAL quasars (cf., Punsly & Zhang, 2010). Therefore, the difference might not be physically meaningful and further confirmation is required.

Though it needs further confirmation, the differences noted above could explain the rarity of the FR II–BAL quasars and the statistical properties of the FR II sample. Generally, the universe is populated by compact radio sources whose linear size is less than ~ 1 kpc (O’Dea et al., 1991; Readhead et al., 1996; O’Dea & Baum, 1997). They are progenitors of a large-sized radio source (Fanti et al., 1995). To explain the overabundance of these young radio sources, intermittent activity is proposed (Reynolds & Begelman, 1997), where most of the sources would terminate its activity during the course of the evolution (e.g., Parma et al., 2007; Orienti et al., 2010). Though nowadays the jet-disk connection in AGN is not well understood, the intermittency is thought to result from instability of the disk (e.g., Czerny et al., 2009). There are several kinds of the instability. For examples in AGN, ionization instability operates on a longer timescale ($\gtrsim 10^6$ yrs; Mineshige & Shields 1990), whereas radiation pressure instability works on a shorter timescale ($\lesssim 10^6$ yrs; Czerny et al.

2009). Because age of 10^7 – 10^8 years is inferred for typical radio galaxies whose linear size is ~ 100 kpc (see references in Kawakatu et al., 2008), the latter could make the young radio sources overpopulated (Czerny et al., 2009). Now, timescale and amplitude of the instability depend on black hole mass and Eddington ratio, which are also key parameters to launch the disk wind (Nomura et al., 2013). Thus, at the condition where the disk wind can be launched, radiation pressure instability might be strong and could not produce an appropriate timescale or amplitude needed to feed large-sized radio sources. In this case, once BAL quasars have strong and continuous activity, the same radio lobes as in non-BAL quasars are formed. This is consistent with what we have confirmed.

5.5 Conclusions

Rarity of large-sized FR II–BAL quasars has been contrary evidence for the simple orientation scheme. Meanwhile, there is still large ambiguity in the estimate. In this chapter, using SDSS DR7 and the FIRST survey, we constructed the FR II quasars catalog at $1.68 \leq z \leq 4.93$. Utilizing identified 12 FR II–BAL quasars, we presented its statistical properties including physical parameters as follows:

- Fraction of C IV BAL quasars in the FR II sample is 2.7 ± 0.7 times less than that in the total SDSS sample. This estimate is consistent with Shankar et al. (2008) while different from Gregg et al. (2006). The statistic in Gregg et al. (2006) was biased by redshift dependence of detection rate of steep spectral radio lobes. At this point, our estimate is more reasonable. Moreover, this rarity is not explained by the simple orientation scheme; differences in the source environment and/or the central engine are possible origin of the rarity.
- To investigate the origin of the rarity, we made statistical comparisons between BAL and non-BAL quasars in the FR II sample for the first time. If BAL quasars are in a dense environment as predicted in the evolution scheme, radio morphology of BAL quasars could be more distorted than non-BAL quasars. However, distributions of physical parameters representing radio morphology which are lobe opening angle, arm-length ratio, and flux density ratio are indistinguishable between the BAL and non-BAL quasars. Thus, we did not find the evidence for the confinement.
- In addition to the above, radio power and projected linear size are also similar between the two samples. This suggests that non-thermal jet of BAL quasars can be similarly powerful and large to non-BAL quasars. In contrast, we found significant differences in black hole mass and Eddington ratio between them. Though it needs further confirmation, some intrinsic differences related to these physical values (e.g., duty cycle of the jet activity) might rule the rarity.

6.1 Summaries

BAL is found in 10–30% of quasars in SDSS. The most widely discussed hypothesis to account for this fraction is the orientation scheme where BAL is detected in relatively edge-on AGN (Elvis, 2000). To test this scenario, one of the most direct ways is radio observation. Until now, lower flux density and steeper spectral index of BAL quasars have been attributed to the orientation effect (Shankar et al., 2008; DiPompeo et al., 2011). Thus, the orientation scheme should play a role in BAL phenomena at least in part. At the same time, there are also radio properties incompatible with the hypothesis (e.g., Becker et al., 2000; Gregg et al., 2006; Shankar et al., 2008). To explain these contrary evidence, several hypotheses have been proposed. One of them is the evolution scheme. There, BAL is observed in a relatively early phase before its emergence from a thick shroud, and non-thermal jet of BAL quasars is frustrated by the ambient medium (Becker et al., 2000).

Despite the above considerations, at the moment bases for each hypothesis are not solid. To investigate radio properties of BAL quasars and then to uncover its origin, we made several studies of the morphology and spectrum from mas- to arcsecond-scale resolution. Here, we summarize the conclusions of the thesis. First, radio properties described in the previous chapter are as follows:

Radio morphology and spectrum at mas-scale resolution (Chapter 3)

In Chapter 3, we performed multi-frequency polarimetric VLBI imaging of a radio-loud BAL quasar, J1159+0112, whose GPS was reported by Montenegro-Montes et al. (2008a).

- Genuine GPS sources which are dominated by absorbed lobes are sometimes misidentified as a flaring state of blazars. To discriminate the genuine GPS sources from the blazars, VLBI observation with high angular resolution is efficient. As a result,

the source shows characteristics typical of the genuine GPS sources associated with quasars. Thus, BAL quasars can host the genuine GPS sources.

- The VLBI observations also provided us direct measurement of the inclination of the source. Though a degeneracy between the jet velocity and orientation is not solved, we set constraints on the inclination of the jet axis with respect to the line of sight as $\theta > 73$ deg.

Radio spectrum at arcsecond-scale resolution (Chapter 4)

In Chapter 4, we made GMRT survey observations of BAL quasars at 322 MHz. The targets were selected from SDSS DR5 and the FIRST survey. This is the first systematic observation at the frequency in the world.

- Previous radio observations with arcsecond-scale resolution suggested many GPS/CSS sources are associated with BAL quasars (Montenegro-Montes et al., 2008a). As confirmed in Chapter 3, actually BAL quasars can host the genuine GPS sources. However, such a strong absorption of BAL quasars has not been understood well because most of previous studies were made in the gigahertz regime. The only way to detect the absorption is observation at low frequency. We revealed that approximately half of the targets suffer from the absorption. Moreover, a statistical comparison between the BAL and non-BAL samples suggests no significant difference in the spectral index distribution at the low frequency. Thus, the absorption between the two samples is comparable.

Radio morphology at arcsecond-scale resolution (Chapter 5)

In Chapter 5, using SDSS DR7 and the FIRST survey, we constructed the FR II quasars catalog at $1.68 \leq z \leq 4.93$. Combined with BAL quasars in SDSS DR7, we identified 12 FR II–BAL quasars and investigated their statistical properties.

- There has been still large ambiguity in rarity of large-sized FR II–BAL quasars. We found the fraction of BAL quasars in the FR II sample is 2.7 ± 0.7 times less than that in the total SDSS sample. This estimate is consistent with Shankar et al. (2008) while different from Gregg et al. (2006). Gregg et al. (2006) could be affected by bias in connection with redshift.
- We also investigated physical parameters related to environment of the sources, which are lobe opening angle, arm-length ratio, and flux density ratio. We did not find the significant difference in these parameters. This suggests the environment of the FR II sample is similar between BAL and non-BAL quasars.

- We found projected linear size and lobe luminosity are indistinguishable between the two subsamples. In general, to evolve to large-sized radio sources, a certain amount of intense core activity has to continue for a long period. Therefore, the result indicates radio activity of BAL quasars can be similarly active in non-BAL quasars in terms of the strength and period.
- Though it needs further confirmation, there is a significant difference in the black hole mass and Eddington ratio. This implies an intrinsic differences between BAL and non-BAL quasars.

Consequently, these findings provide several suggestions for the origin of BAL quasars:

Confirmation of (in)validity of the orientation scheme

Again, previous studies suggested BAL phenomena should be controlled by the orientation effect at least in part. The inclination of J1159+0112 measured with VLBI (Chapter 3) does not compete with this. In contrast, the rarity of FR II–BAL quasars (Chapter 5) is incompatible with the orientation model. As discussed by many authors, the simple orientation scheme cannot explain the entire BAL phenomena.

DiPompeo et al. (2011) reported that BAL quasars show wide range of radio spectral index similar to non-BAL quasars. Because spectral index is a statistical indicator of the viewing angles, they concluded that, though edge-on viewing is preferred for BAL quasars, pole-on BAL quasars also exist as in non-BAL quasars (DiPompeo et al., 2012). However, we found BAL quasars suffering from strong absorption (Chapter 4). These sources show flat or inverted spectrum regardless of the inclination. Therefore, the spectral index distribution presented by DiPompeo et al. (2011) itself could not suggest incompleteness of the orientation scheme.

Findings of counter-evidence for the evolution scheme

Based on the above discussion, the orientation effect is considered to work together with another factor. Here, one of the candidates is the evolution scheme where quasars show BAL before its emergence from merger-produced ultraluminous infrared galaxies (Voit et al., 1993) and the radio emission of BAL quasars might be frustrated to small scales by the dense environment (Becker et al., 2000). A large number of GPS/CSS sources reported by Montenegro-Montes et al. (2008a) has been a basis for this evolution scenario. In Chapter 4, we confirmed BAL quasars can host the genuine GPS source. However, statistically we did not find evidence for the stronger frustration of BAL quasars than non-BAL quasars. First, extent of low-frequency absorption is indistinguishable between BAL and non-BAL quasars (Chapter 4). Second, asymmetry of the large-sized FR II quasars are also similar

between the two quasar subgroup (Chapter 5). These findings are contrary evidence of the confinement of BAL quasars. Then, the evolution scheme might not be the case.

Implication for an intrinsic difference in the central engine

Since the orientation scheme is not complete, another hypothesis (except the evolution scheme) is still needed to explain the entire BAL phenomena. In Chapter 5, we found hints of an intrinsic difference between the two subgroups. BAL and non-BAL quasars can be similarly active with respect to the strength and period of radio activity, but emergence of such an activity is less common in BAL quasars. Duty cycle of jet activity in BAL quasars is distinct from that in non-BAL quasars. In addition, though further confirmation is required, the black hole mass and Eddington ratio are different between BAL and non-BAL quasars in the FR II sample. This implies dependence of the duty cycle on the accretion process could be different between the two AGN classes. This might be the reason why BAL quasars show radio properties not explained by the orientation effect.

6.2 Future Prospects

Although we provided the new insights into radio properties of BAL quasars, there still remain unresolved issues. Here, we suggest the future prospects needed to uncover the orientation, environment, and intrinsic properties of BAL quasars.

Quest for the orientation

Because of difficulty in measuring the apparent jet velocity of high- z BAL quasars, morphological studies for individual sources can only provide mild constraints even with VLBI (Chapter 3). To make further test of the orientation scheme, a different approach would be required. Generally, observed power of decelerated lobes does not depend on the inclination of the sources while observed core power is strongly affected by the orientation effect. Assuming equipartition, there should be a correlation between lobes and intrinsic core power, which was observationally confirmed by Giovannini et al. (2001). Therefore, in case that Doppler beaming factor of BAL quasars is different from non-BAL quasars, a correlation between the observed power of the lobes and core should differ between these two AGN subclasses. Utilizing this, we can test the orientation scheme statistically. As noted in Chapter 4, both quasars suffer from significant absorption. To restore the intrinsic radio power, it is important to make low-frequency observation at multi frequency.

Quest for the environment

Though our GMRT survey observation in Chapter 4 has provided a large number of BAL quasars suffering from absorption, the origin of the absorption is not uncovered yet. To discriminate between synchrotron self-absorption and free-free absorption, multi-frequency

observations with higher sensitivity are required. In addition, optical depth obtained by the observations will provide information about the ambient medium. Then, we can compare the environment of the sources more precisely. Moreover, polarization properties also give us hints about the ambient medium considering rotation measure.

Quest for the intrinsic difference

In Chapter 5, we found similarity in the lobe luminosity and projected linear size between BAL and non-BAL quasars with large-sized FR II morphology. This is important basis for the difference in the duty cycle. However, identification of the lobes is just based on images on the celestial sphere. To confirm that the selected components are true lobes, multi-frequency observations are required. In contrast to these large-sized sources, the similarity might not be appropriate to the sources unresolved by the FIRST survey. Comparisons of lobe power is also needed for the compact sources. Although we made low-frequency survey observations for the unresolved sources, the sample size is still small to uncover the intrinsic nature (see Chapter 4). To investigate whether flux density at the frequency is dominated by decelerated lobes and then to test the difference in the lobe luminosity, extensive survey with a larger sample is expected.

We also found the significant difference in the black hole mass and the Eddington ratio measured by broad emission lines. However, these results might be biased by BAL feature in the optical spectrum. To test the difference, we have to observe another emission line free from absorption features like BAL. Near-infrared spectroscopy to aim broad $H\beta$ emission would be a realistic way for high- z BAL quasars. If the difference is real, dependence of the duty cycle on the accretion process could differ between the two subgroup. In this case, a comparison with transition between low and hard states of stellar mass black hole binaries (Fender et al., 2004, 2009) is interesting (e.g., Maccarone et al., 2003).

Investigation with future observing system

In future, extensive low-frequency arrays such as the LOw Frequency ARray (LOFAR) and the Square Kilometre Array (SKA) will come. These telescopes will grow our understanding of BAL quasars utilizing the non-thermal emission from the decelerated lobes.

Now, difficulties in unveiling the origin of the BAL phenomena lie in the fact that the absorption lines appear in rest ultraviolet. Because BAL quasars are not found in the nearby universe, we cannot look at the sources with high spatial resolution. Meanwhile, recently ultra-fast outflow (UFO) has been found which is absorption trough at soft X-ray wavelength and whose origin is also considered to be the disk wind (Tombesi et al., 2010a,b, 2011, 2013). As in BAL quasars, the relation between UFO and the unified model of AGN has been also discussed there. Although UFO is only found at low redshift at present,

future X-ray observatory like ASTRO-H would give us keys to unify the nearby UFO and the high-redshift BAL. This will improve our understanding of BAL.

Radio-interferometer Polarimetry

A

A.1 Stokes Parameters

Figure A.1 show oscillating plane of the electric vector. The direction of the wave is out of the page, towards the observer. In the x - y coordinate system, the electric vector is given by

$$\mathbf{E} = \begin{pmatrix} \tilde{E}_x \\ \tilde{E}_y \end{pmatrix} \cdot \begin{pmatrix} \mathbf{e}_x \\ \mathbf{e}_y \end{pmatrix}, \quad (\text{A.1})$$

where \tilde{E}_x and \tilde{E}_y are complex amplitude whose real part are given by

$$\begin{aligned} \text{Re}\tilde{E}_x &= E_x \cos(\omega t - \phi_x) \\ \text{Re}\tilde{E}_y &= E_y \cos(\omega t - \phi_y). \end{aligned} \quad (\text{A.2})$$

Generally, these equations indicate elliptically polarized radiation.

The elliptically polarized radiation can be also written under x' - y' coordinate system in Figure A.1 whose axes are parallel to the direction of the ellipse. The electric vector is written as

$$\mathbf{E} = \begin{pmatrix} \tilde{E}'_x \\ \tilde{E}'_y \end{pmatrix} \cdot \begin{pmatrix} \mathbf{e}'_x \\ \mathbf{e}'_y \end{pmatrix}, \quad (\text{A.3})$$

where \tilde{E}'_x and \tilde{E}'_y are complex amplitude whose real part are given by

$$\begin{aligned} \text{Re}\tilde{E}'_x &= E'_x \cos \omega t \\ \text{Re}\tilde{E}'_y &= E'_y \sin \omega t. \end{aligned} \quad (\text{A.4})$$

Here, we define eccentricity of the ellipse as $\sqrt{1 - \tan^{\pm 2} \beta}$, where the domain of β is $-\pi/2 \leq \beta \leq \pi/2$. Then, minor and major axes of the ellipse are given by $E'_x = E_0 \cos \beta$ or $E'_y = E_0 \sin \beta$.

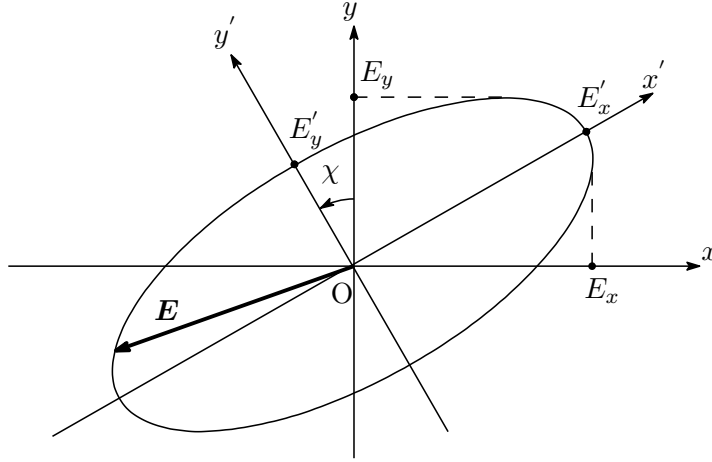


Figure A.1 Oscillating plane of the electric vector. x and y axis are fixed on space, and x' and y' axis are parallel to the direction of the ellipse. The direction of the wave is out of the page, towards the observer.

The coordinates used above are related by transformation of the bases, that is

$$\begin{pmatrix} \mathbf{e}'_x \\ \mathbf{e}'_y \end{pmatrix} = \begin{pmatrix} \cos \chi & \sin \chi \\ -\sin \chi & \cos \chi \end{pmatrix} \begin{pmatrix} \mathbf{e}_x \\ \mathbf{e}_y \end{pmatrix}. \quad (\text{A.5})$$

Substitution of this for Equation A.3 yields

$$\mathbf{E} = E_0 \begin{pmatrix} \cos \beta \cos \chi \cos \omega t - \sin \beta \sin \chi \sin \omega t \\ \cos \beta \sin \chi \cos \omega t + \sin \beta \cos \chi \sin \omega t \end{pmatrix} \cdot \begin{pmatrix} \mathbf{e}_x \\ \mathbf{e}_y \end{pmatrix}. \quad (\text{A.6})$$

Comparing Equation A.1 with Equation A.6, then we get

$$\begin{pmatrix} E_x \cos(\omega t - \phi_x) \\ E_y \cos(\omega t - \phi_y) \end{pmatrix} = E_0 \begin{pmatrix} \cos \beta \cos \chi \cos \omega t - \sin \beta \sin \chi \sin \omega t \\ \cos \beta \sin \chi \cos \omega t + \sin \beta \cos \chi \sin \omega t \end{pmatrix}. \quad (\text{A.7})$$

Because of $\cos(\omega t - \phi_x) = \cos \omega t \cos \phi_x + \sin \omega t \sin \phi_x$ and $\cos(\omega t - \phi_y) = \cos \omega t \cos \phi_y + \sin \omega t \sin \phi_y$, we get

$$\begin{aligned} E_x \cos \phi_x &= E_0 \cos \beta \cos \chi \\ E_x \sin \phi_x &= -E_0 \sin \beta \sin \chi \\ E_y \cos \phi_y &= E_0 \cos \beta \sin \chi \\ E_y \sin \phi_y &= E_0 \sin \beta \cos \chi. \end{aligned} \quad (\text{A.8})$$

As a result, amplitude of the electric vector is written in terms of E_0 , β , and χ instead of E_x , ϕ_x , E_y , and ϕ_y .

It is useful to describe polarized radiation by Stokes parameters of I , Q , U , and V (Rybicki & Lightman, 1979). In case of monochromatic wave, Stokes parameters are given

by

$$\begin{pmatrix} I \\ Q \\ U \\ V \end{pmatrix} \equiv \begin{pmatrix} E_x^2 + E_y^2 \\ 2E_x E_y \cos(\phi_x - \phi_y) \\ E_x^2 - E_y^2 \\ 2E_x E_y \sin(\phi_x + \phi_y) \end{pmatrix} = \begin{pmatrix} E_0^2 \\ E_0^2 \cos 2\beta \cos 2\chi \\ E_0^2 \cos 2\beta \sin 2\chi \\ E_0^2 \sin 2\beta \end{pmatrix}, \quad (\text{A.9})$$

where I means total power of the radiation, Q and U mean power of linearly polarized radiation, and V means power of circularly polarized radiation. Specific case of $\beta = 0$ (namely, the eccentricity is zero) suggests completely linearly-polarized radiation. In this case, using Equation A.9, we get a polarization angle as

$$\chi = \frac{1}{2} \arctan \frac{U}{Q}. \quad (\text{A.10})$$

■ A.2 Stokes Parameters and Visibilities

In the case of right-hand circular polarization (RHCP) and left-hand circular polarization (LHCP) receiver, the relation between Stokes parameters and visibilities is given by

$$\begin{pmatrix} I \\ Q \\ U \\ V \end{pmatrix} = \frac{1}{2} \begin{pmatrix} 1 & 1 & 0 & 0 \\ 0 & 0 & 1 & 1 \\ 0 & 0 & -i & -i \\ 1 & -1 & 0 & 0 \end{pmatrix} \begin{pmatrix} R_i R_j^* \\ L_i L_j^* \\ R_i L_j^* \\ L_i R_j^* \end{pmatrix}, \quad (\text{A.11})$$

under the perfect feeds and the perfectly calibrated data (Roberts et al., 1994). Here R_i and L_i are power of RHCP and LHCP obtained by i -th antenna, respectively. Asterisk in index means conjugation.

■ A.3 D -term Approximation

There are no ideal feed that receives intended signal only. In first order approximation, the power at i -th antenna induced in the feeds for RHCP, R'_i , and LHCP, L'_i , is expressed as

$$\begin{aligned} L'_i &= L_i + D_{Ri} R_i \\ R'_i &= R_i + D_{Li} L_i \end{aligned} \quad (\text{A.12})$$

where R_i and L_i are power of the propagated radiation of RHCP and LHCP, respectively. The first term in each equation is the response of the intended polarization and the second term (D -term) is that of orthogonally polarized radiation (instrumental polarizations). This is called linear feed model or D -term approximation.

Taking correlation between the power obtained at i -th antenna and j -th antenna, we get each "parallel-hands" term and "cross-hands" term as

$$\begin{pmatrix} R'_i R'_j{}^* \\ L'_i L'_j{}^* \\ R'_i L'_j{}^* \\ L'_i R'_j{}^* \end{pmatrix} = \begin{pmatrix} R_i R_j{}^* \\ L_i L_j{}^* \\ R_i L_j{}^* \\ L_i R_j{}^* \end{pmatrix} + \begin{pmatrix} 0 & D_{Ri} D_{Rj}^* & D_{Rj}^* & D_{Ri} \\ D_{Li} D_{Lj}^* & 0 & D_{Li} & D_{Lj}^* \\ D_{Lj}^* & D_{Ri} & 0 & D_{Ri} D_{Lj}^* \\ D_{Ri} & D_{Lj}^* & D_{Li} D_{Rj}^* & 0 \end{pmatrix} \begin{pmatrix} R_i R_j{}^* \\ L_i L_j{}^* \\ R_i L_j{}^* \\ L_i R_j{}^* \end{pmatrix}. \quad (\text{A.13})$$

Supposing that D -terms are sufficiently small, that is $D \ll 1$, we are able to ignore the second-order terms of D . Then, we get

$$\begin{pmatrix} R'_i R'_j{}^* \\ L'_i L'_j{}^* \\ R'_i L'_j{}^* \\ L'_i R'_j{}^* \end{pmatrix} = \begin{pmatrix} R_i R_j{}^* \\ L_i L_j{}^* \\ R_i L_j{}^* \\ L_i R_j{}^* \end{pmatrix} + \begin{pmatrix} 0 & 0 & D_{Rj}^* & D_{Ri} \\ 0 & 0 & D_{Li} & D_{Lj}^* \\ D_{Lj}^* & D_{Ri} & 0 & 0 \\ D_{Ri} & D_{Lj}^* & 0 & 0 \end{pmatrix} \begin{pmatrix} R_i R_j{}^* \\ L_i L_j{}^* \\ R_i L_j{}^* \\ L_i R_j{}^* \end{pmatrix}. \quad (\text{A.14})$$

Equation A.14 suggests that parallel-hands terms are contaminated by cross-hands terms and vice versa. According to Equation A.11, if circularly polarization is negligible, parallel hands terms and cross-hands terms reflect the power of total intensity and linearly polarized radiation, respectively. As a result, D -terms make total intensity and polarized radiation contaminated by each other. We have to solve for D to obtain the response of the intended polarization.

In the specific case of completely unpolarized sources, we have $Q = U = V = 0$. Then, using Equations A.11 and A.14, we obtain

$$\frac{R'_i L'_j{}^*}{R'_i R'_j{}^*} = \frac{L'_i R'_j{}^*}{R'_i R'_j{}^*} = D_{Ri} + D_{Lj}^*. \quad (\text{A.15})$$

FR II quasars catalog | B

In Chapter 5, we constructed the FR II quasars catalog at $1.68 \leq z \leq 4.93$ based on the method introduced by de Vries et al. (2006). As a result, we identified 186 FR II quasars. Images of the FR II quasars are shown in Figure B.1. We also present their radio properties in Table B.1. In addition, Figure B.2 displays non-FR II quasars which are once identified as candidates for FR II sources but excluded by our visual inspection.

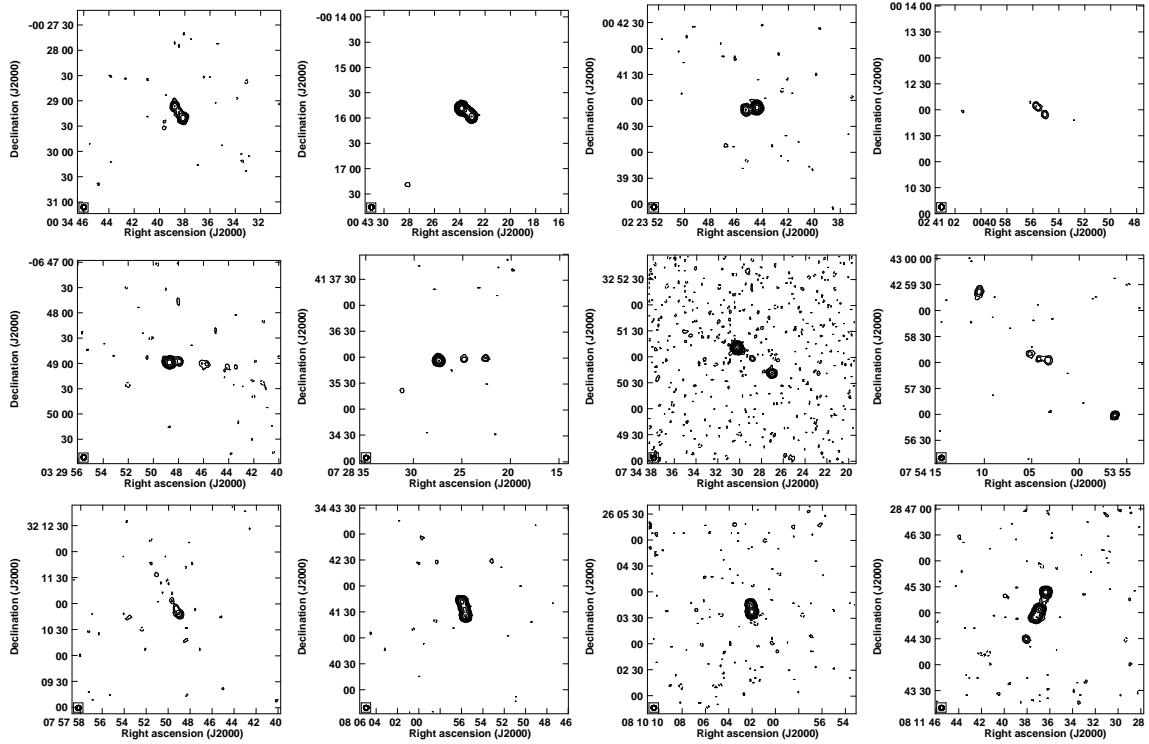
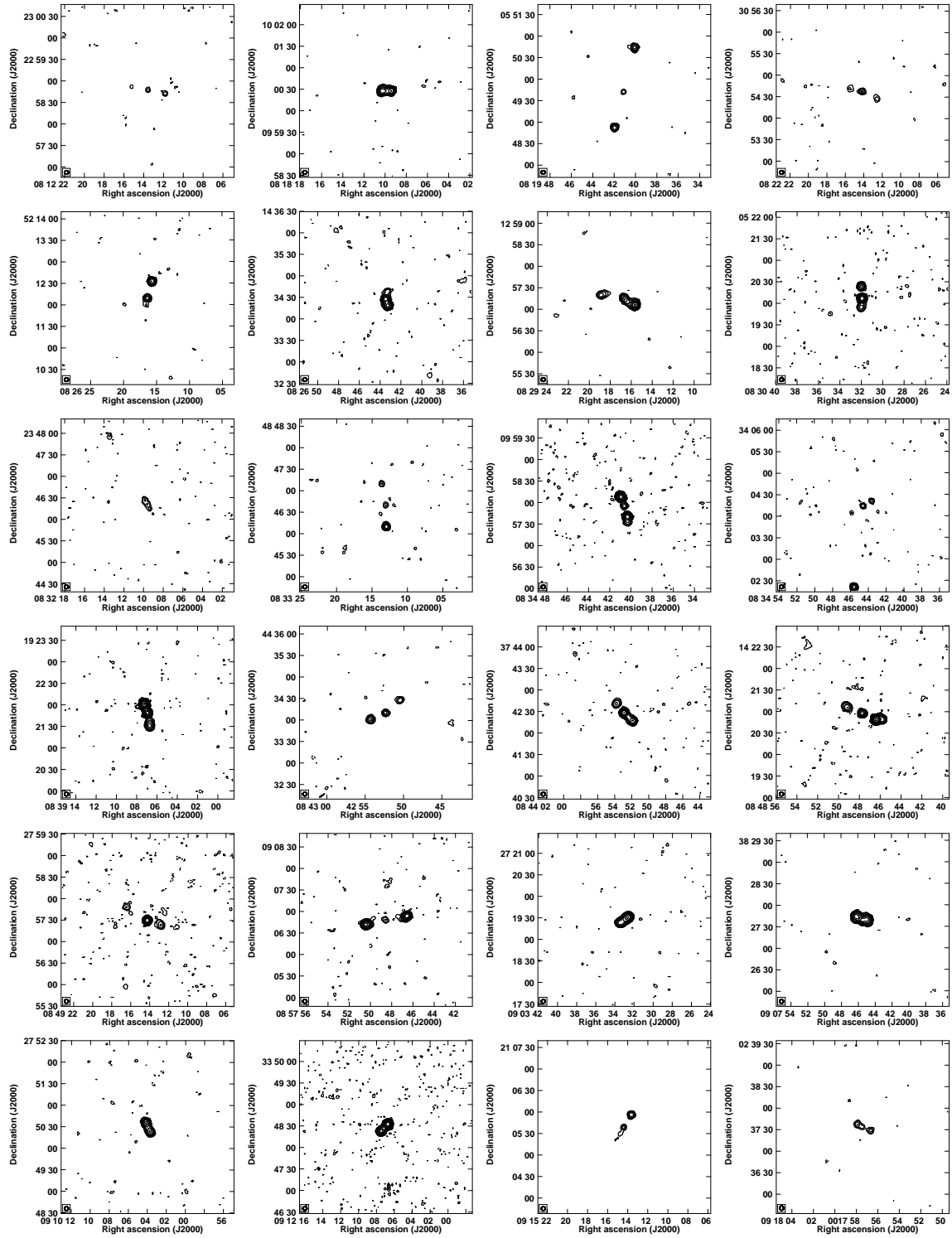
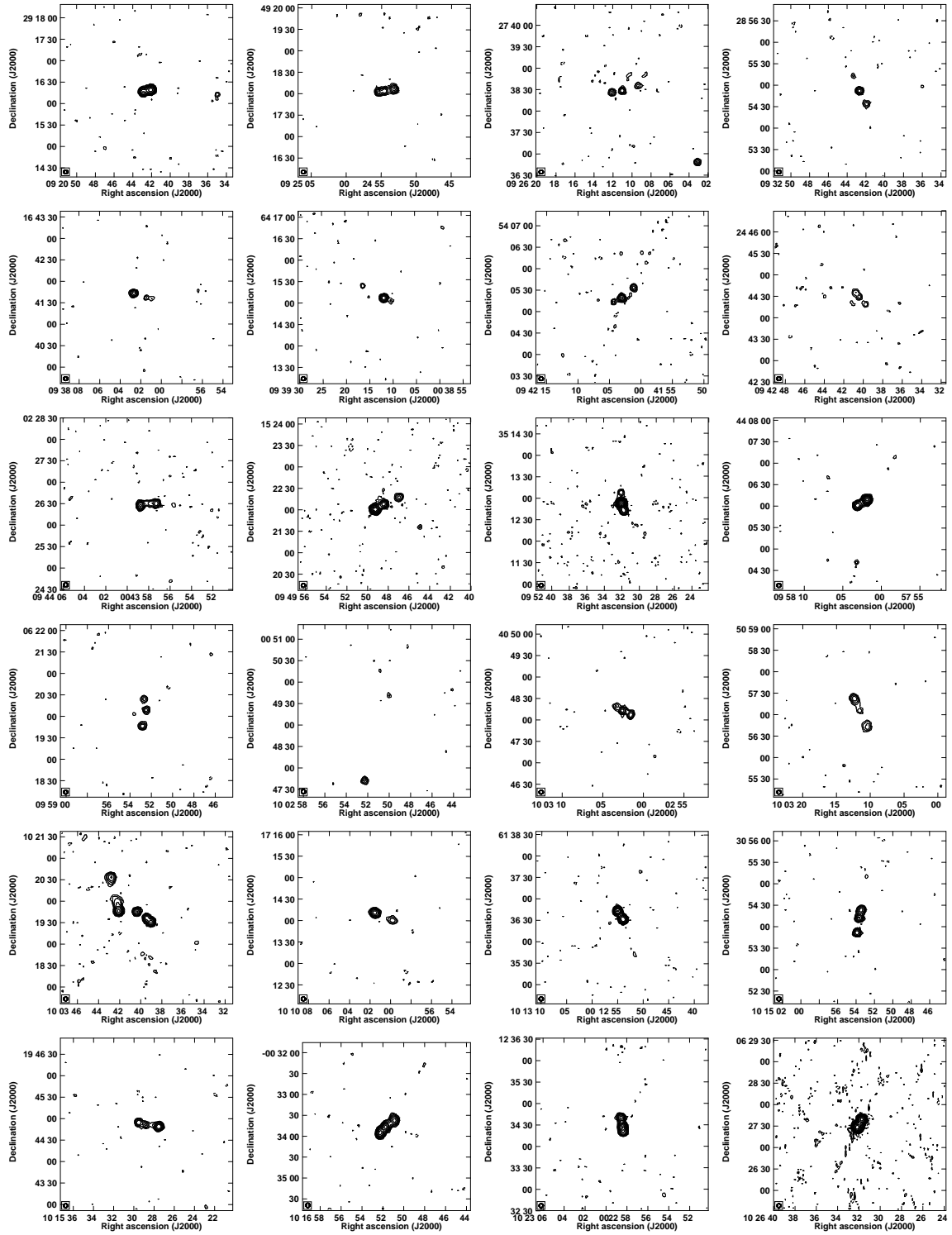
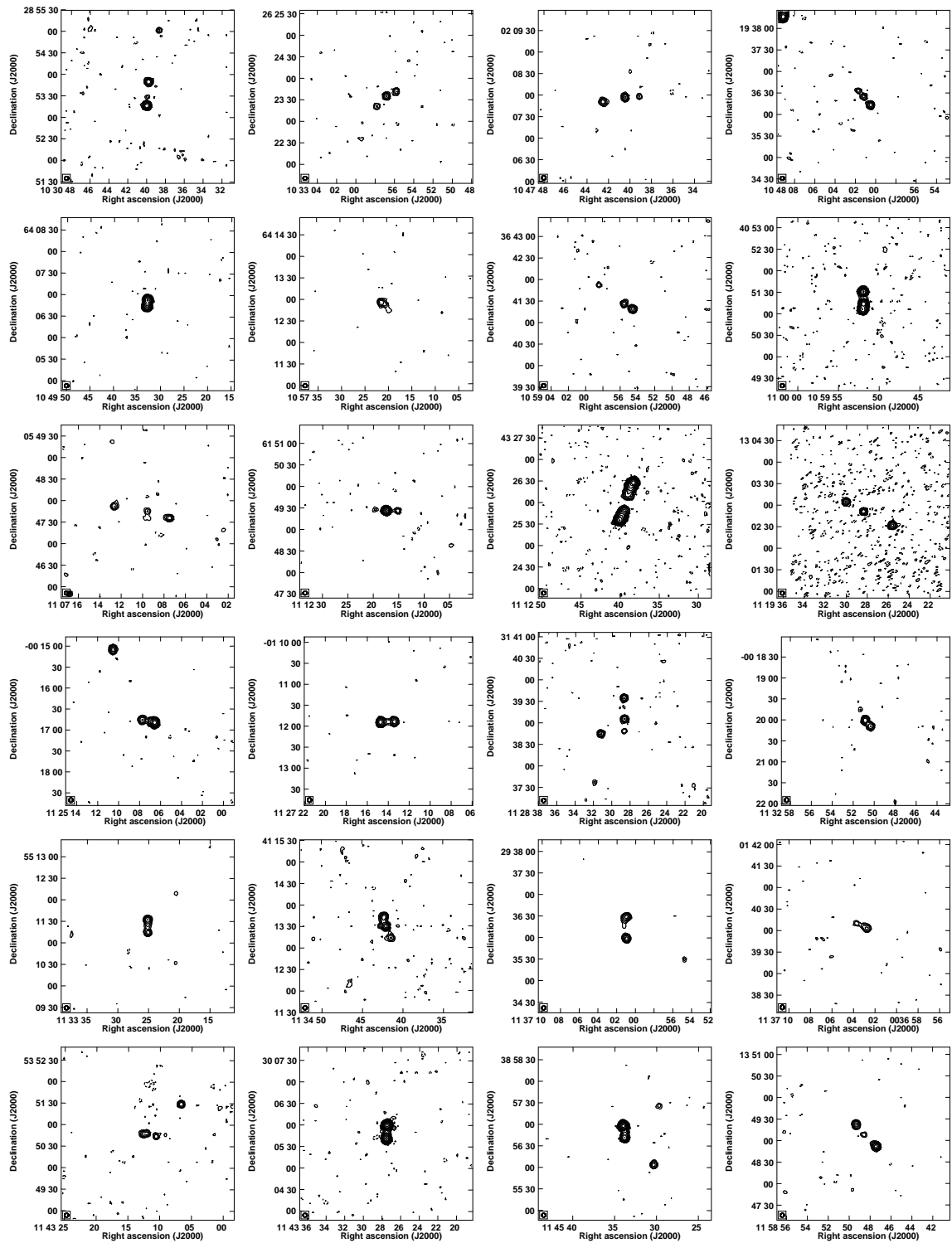
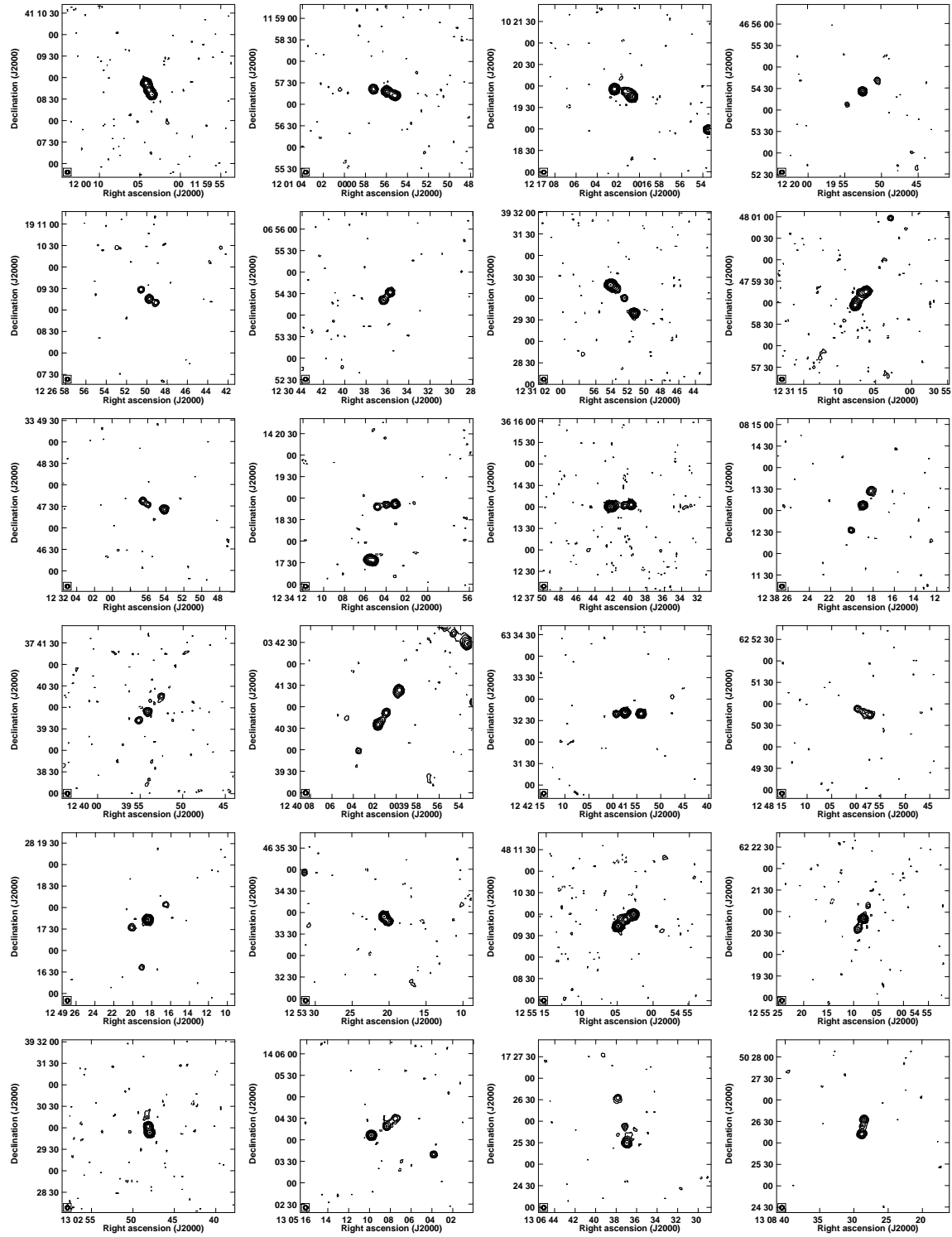


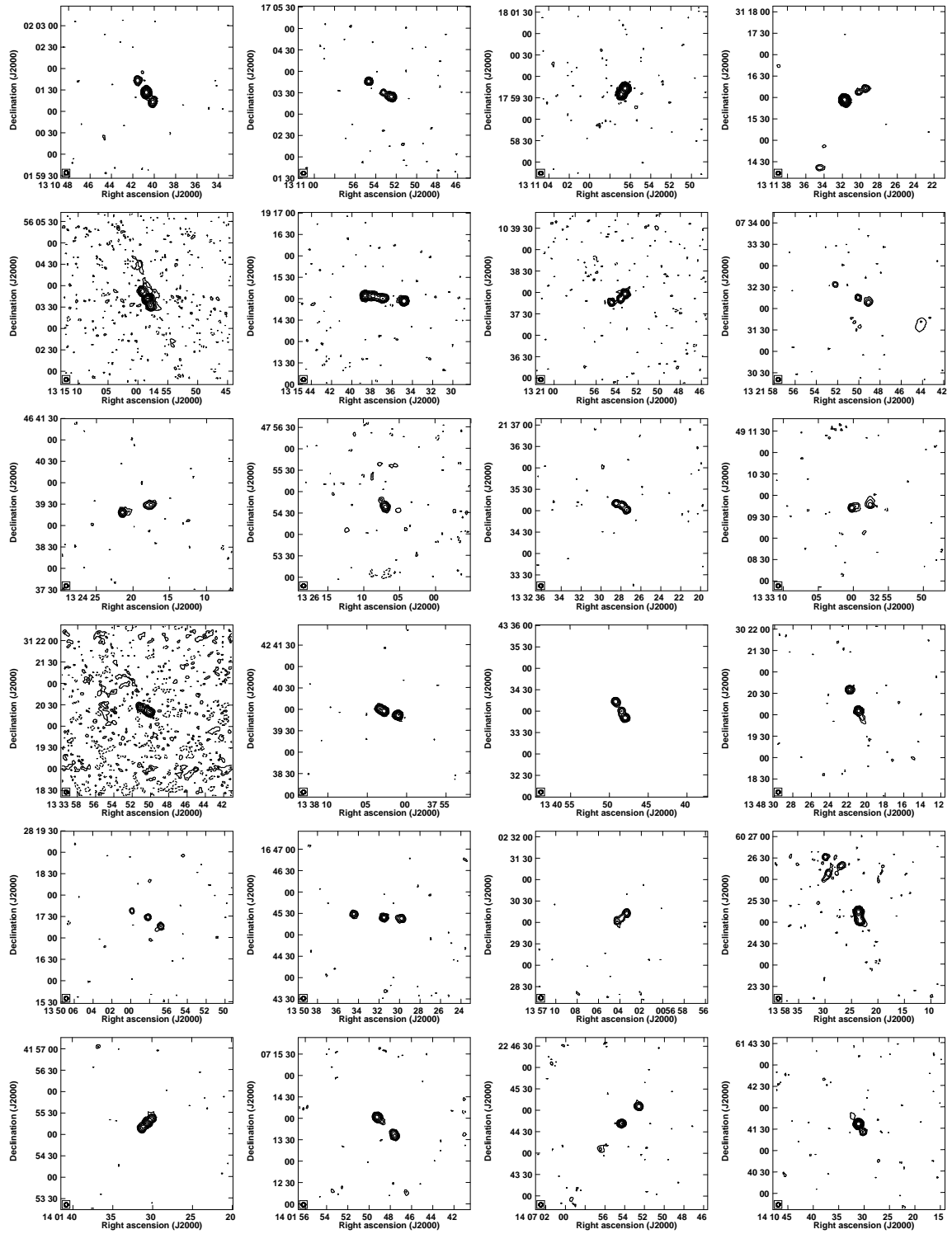
Figure B.1 1.4-GHz FIRST images of FR II quasars. The contours are in successive powers of 2 times the base contour level that is typical 3σ noise level of $0.45 \text{ mJy beam}^{-1}$. Restoring beam is represented in each map. The optical quasars position corresponds to the map center.

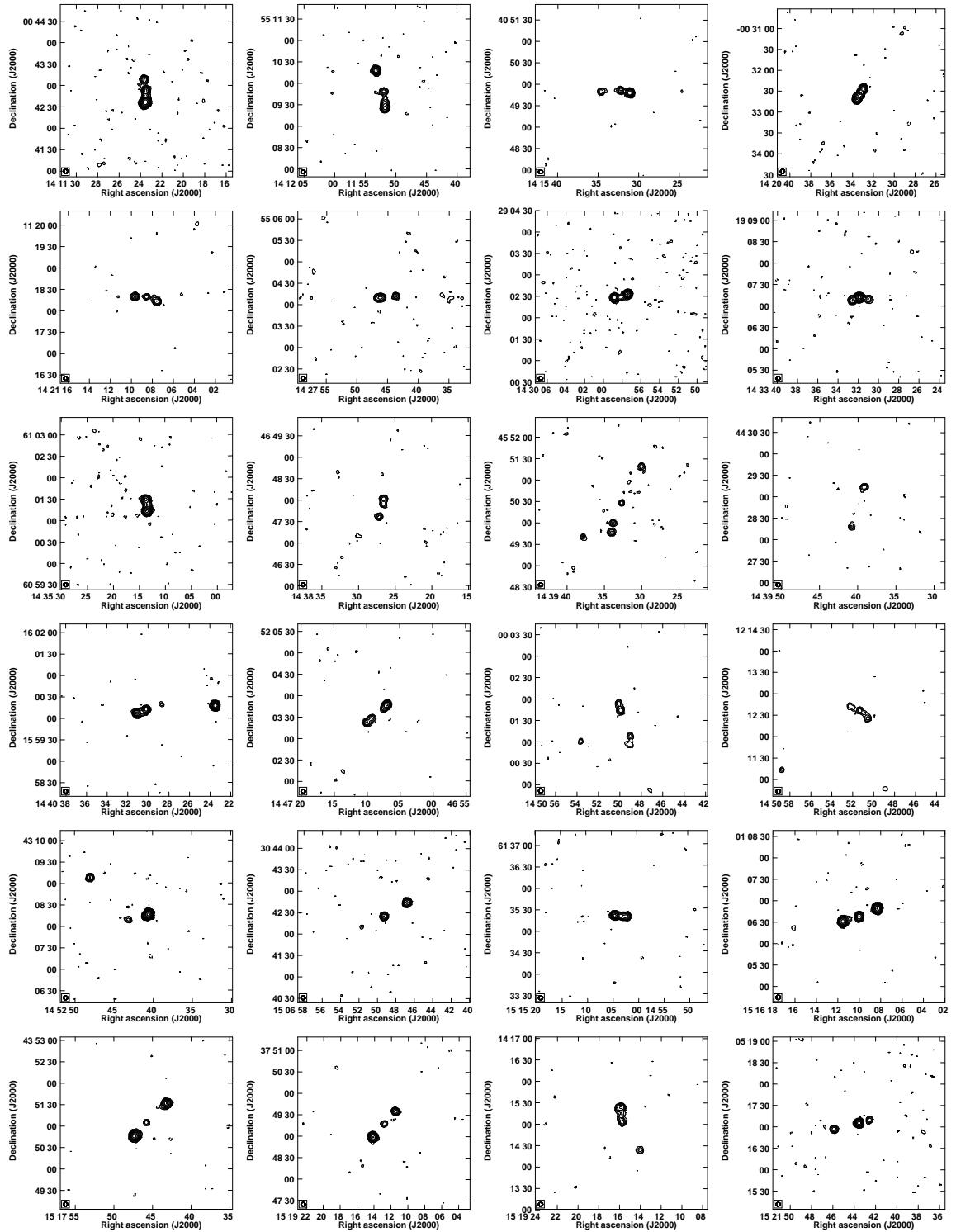
Figure B.1 *Continued*

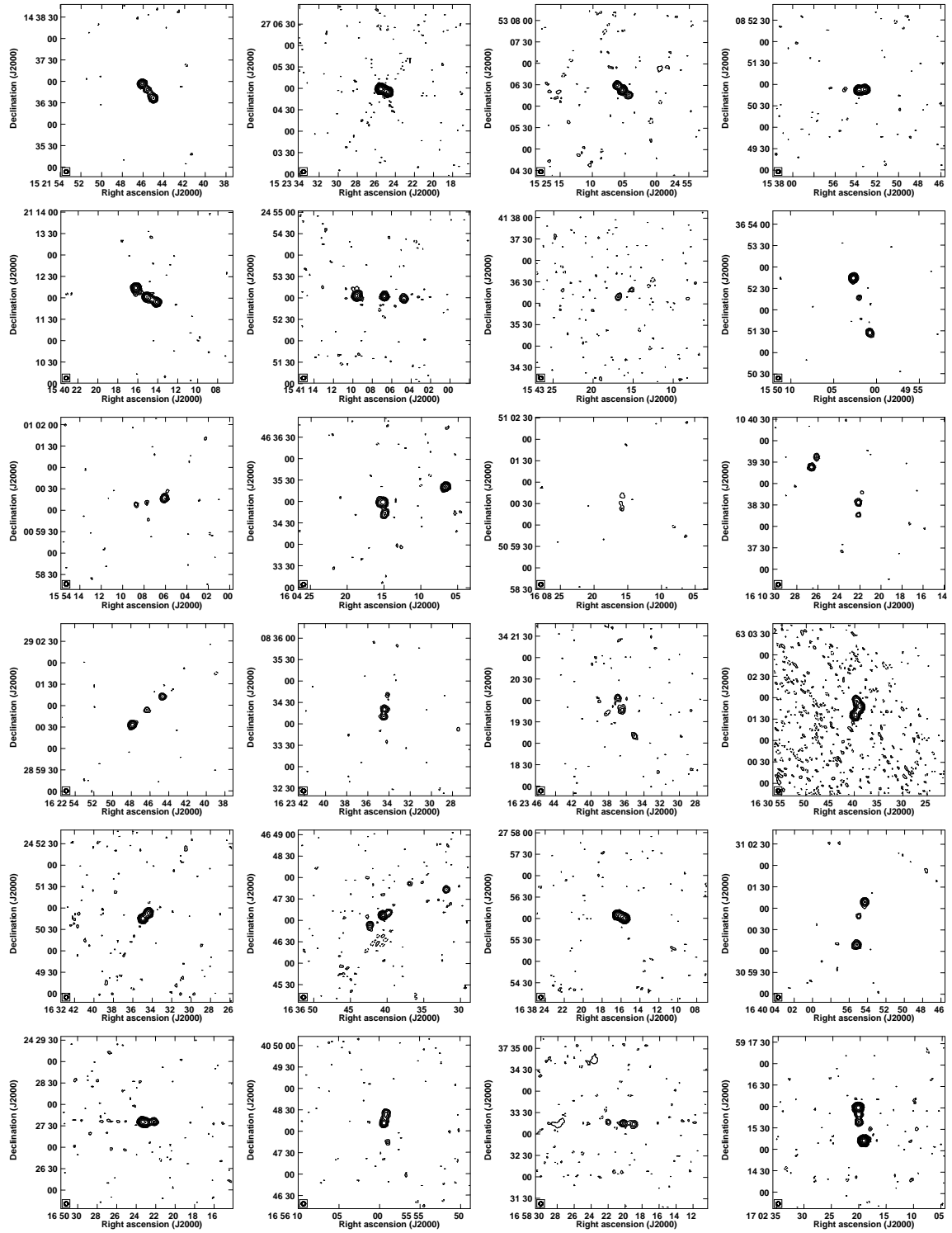
Figure B.1 *Continued*

Figure B.1 *Continued*

Figure B.1 *Continued*

Figure B.1 *Continued*

Figure B.1 *Continued*

Figure B.1 *Continued*

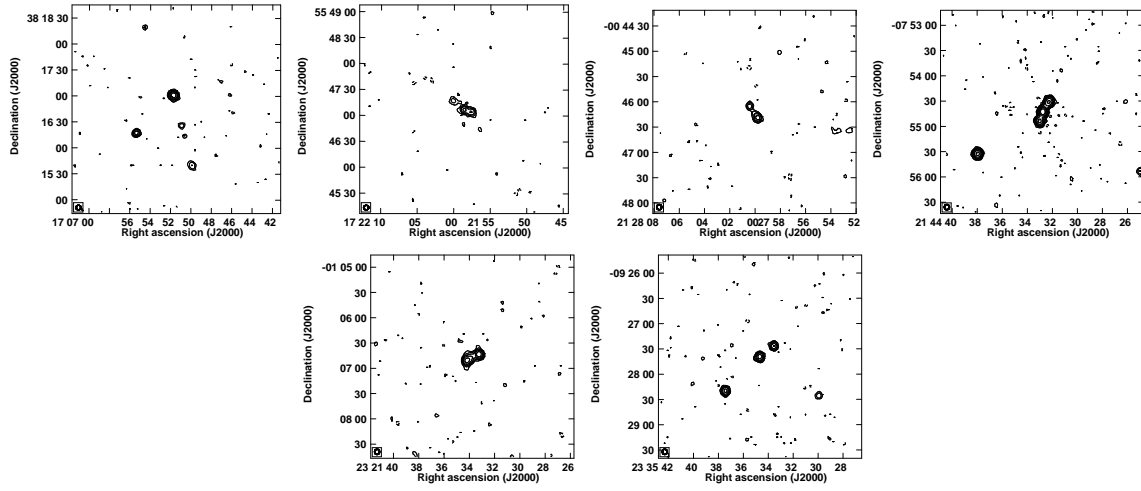
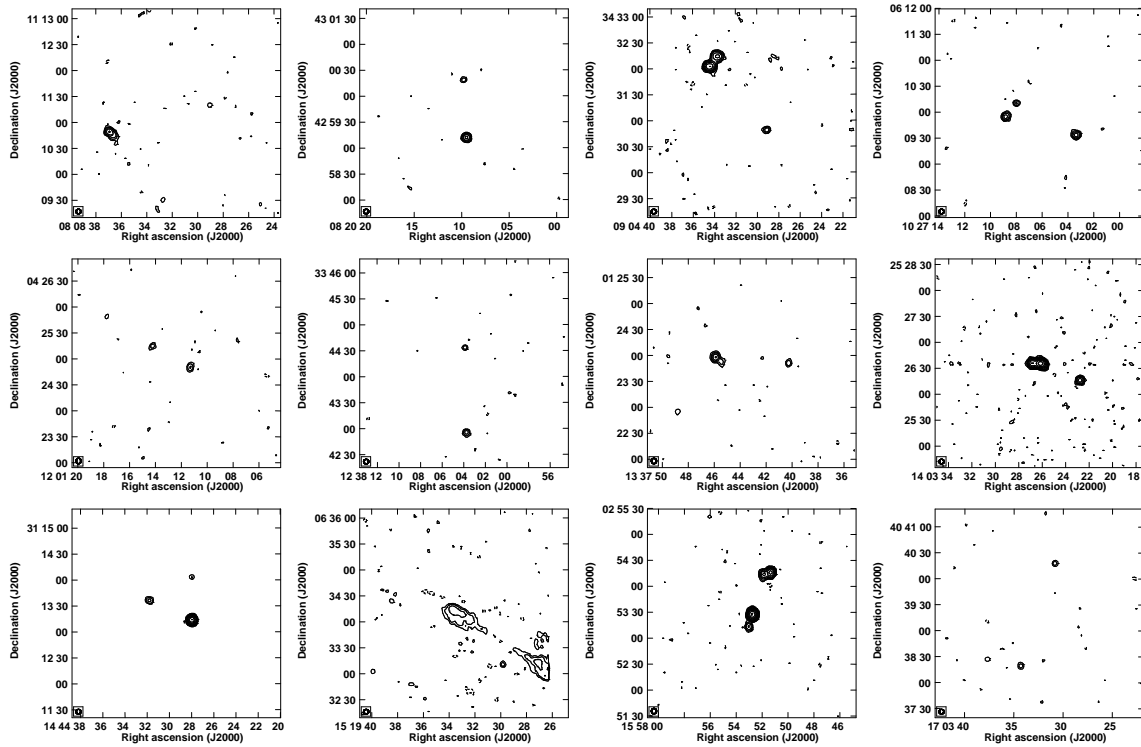
Figure B.1 *Continued*

Figure B.2 1.4-GHz FIRST images of non FR II quasars which are once identified as FR II based on the statistical method described in Chapter 5 but excluded from the catalog by our visual inspection. Same as Figure B.1

Table B.1. Radio Properties of FR II Quasars.

SDSS Name (SDSS J) (1)	z (2)	Φ (deg) (3)	D_1 (arcsec) (4)	D_2 (arcsec) (5)	L (kpc) (6)	S_1 (mJy) (7)	S_2 (mJy) (8)	$\log L_5$ ($\text{erg s}^{-1} \text{Hz}^{-1}$) (9)	Ref. (10)
003438.46-002913.7	1.997	179	7.9	8.0	136	16.8	11.0	33.4	na
004323.43-001552.4	2.798	167	7.4	7.4	119	43.7	114.4	34.5	1
022344.80+004049.7	2.987	165	6.0	7.0	103	52.4	9.8	34.1	na
024055.55+001201.2	2.363	169	3.2	9.8	109	2.9	2.2	32.8	0
032947.92-064857.8	1.754	169	12.0	32.0	380	32.2	2.3	33.4	0
072824.79+413558.4	2.214	180	24.3	29.8	457	2.3	38.2	33.7	na
073428.87+325058.4	1.805	180	22.1	28.6	437	84.4	10.0	33.8	0
075404.23+425804.3	1.726	160	10.1	11.7	188	4.0	2.6	32.6	1
075749.26+321053.1	2.120	177	4.8	11.0	134	7.0	1.8	32.9	na
080555.66+344132.3	1.743	163	7.0	10.1	148	39.3	27.3	33.6	0
081002.05+260340.5	2.266	167	3.4	4.9	70	118.5	22.9	34.2	0
081136.89+284503.5	1.890	172	9.0	21.4	262	27.1	32.5	33.7	1
081213.55+225846.9	2.546	178	23.7	23.9	392	1.0	3.2	32.8	na
081809.95+100027.0	2.182	167	4.1	7.6	99	48.0	38.1	34.0	na
081941.12+054942.6	1.701	180	51.7	63.5	996	8.0	12.3	33.1	na
082214.18+305437.7	1.714	166	16.9	22.5	341	2.6	3.0	32.5	0
082616.34+521209.3	1.843	178	9.3	24.2	289	2.0	17.8	33.2	0
082643.45+143427.6	2.312	152	9.2	10.5	165	51.7	5.3	33.8	na
082916.69+125715.6	1.724	156	18.1	31.6	430	46.1	10.9	33.6	na
083031.93+052006.7	2.217	171	12.1	16.9	245	9.3	22.2	33.6	1
083209.57+234620.2	2.389	169	5.2	7.3	104	2.5	3.5	32.9	na
083313.05+484639.7	2.273	170	29.8	30.7	509	13.6	2.5	33.3	0
083440.61+095754.9	1.762	176	13.7	15.8	255	106.7	62.8	34.1	na
083444.60+340414.4	2.171	175	14.3	18.4	277	2.5	1.1	32.6	0
083906.94+192148.7	1.695	169	13.4	17.5	267	314.8	34.4	34.3	na
084252.40+443410.6	1.780	165	22.5	27.0	427	11.4	5.1	33.1	0
084352.86+374228.2	1.740	175	15.7	16.3	276	26.5	8.6	33.4	0
084847.74+142057.7	1.693	177	21.6	22.7	383	173.6	13.0	34.1	na
084914.27+275729.7	1.728	165	19.5	34.5	467	7.8	4.5	32.9	na
085748.56+090648.1	1.687	179	28.4	30.0	505	57.8	64.9	33.9	na
090333.01+271927.7	1.721	176	3.8	7.1	94	128.2	37.4	34.0	na
090745.46+382739.0	1.743	143	6.2	9.9	139	71.2	41.4	33.9	1
091003.97+275028.8	1.693	169	5.9	7.6	117	28.0	47.7	33.7	na
091207.02+334829.0	1.873	177	5.0	8.0	112	223.5	49.0	34.3	na
091514.41+210538.9	1.775	175	10.7	20.4	268	1.4	8.3	32.8	na
091757.42+023733.9	1.766	175	8.3	12.5	180	2.8	2.8	32.6	1
092042.52+291618.2	1.916	171	4.6	5.7	89	39.6	64.0	33.9	na
092454.55+491804.2	1.943	180	8.2	13.3	185	11.6	13.8	33.3	1
092611.02+273828.2	1.910	171	14.5	23.3	325	5.5	3.4	32.9	na
093242.68+285452.3	1.984	176	21.0	22.5	373	4.0	1.4	32.7	na
093801.43+164137.0	2.020	169	7.9	19.0	230	1.1	12.4	33.1	na
093911.79+641505.9	2.356	171	10.4	34.2	373	2.2	1.6	32.7	na
094203.04+540518.9	2.346	164	12.7	22.0	291	2.4	5.9	33.0	0
094240.41+244429.1	1.715	180	8.2	13.1	184	3.8	2.4	32.6	na
094358.22+022630.5	2.030	158	7.7	8.8	141	9.5	20.1	33.4	1
094948.42+152208.0	1.968	179	10.1	23.4	287	14.0	7.5	33.3	na

Table B.1—*Continued*

SDSS Name (SDSS J) (1)	z (2)	Φ (deg) (3)	D_1 (arcsec) (4)	D_2 (arcsec) (5)	L (kpc) (6)	S_1 (mJy) (7)	S_2 (mJy) (8)	$\log L_5$ (erg s ⁻¹ Hz ⁻¹) (9)	Ref. (10)
095232.02+351252.5	1.878	163	10.6	14.8	219	16.1	4.5	33.2	na
095802.82+440603.7	2.191	175	3.5	11.5	127	36.2	176.1	34.4	0
095852.48+062008.5	2.062	157	15.8	22.7	329	4.0	8.3	33.1	0
100250.44+004919.6	1.877	179	22.7	100.9	1064	1.0	4.5	32.6	0
100302.60+404813.1	2.368	175	10.3	13.2	197	3.5	8.7	33.2	na
100311.56+505705.1	1.838	177	18.7	23.8	366	12.2	8.4	33.2	1
100339.43+101936.7	1.846	168	7.9	16.4	209	49.2	21.1	33.7	na
101000.64+171404.5	1.957	171	12.2	14.5	229	6.4	33.3	33.5	na
101254.24+613634.6	2.054	178	3.1	10.3	114	72.0	69.7	34.1	0
101453.63+305412.3	2.115	177	11.1	20.9	272	16.6	14.9	33.5	na
101528.79+194451.7	1.790	172	10.9	17.8	248	9.6	35.5	33.5	na
101651.73-003347.0	1.828	173	11.0	15.7	230	59.0	30.7	33.8	1
102258.41+123429.7	1.728	167	3.4	10.4	119	94.0	24.7	33.9	na
102631.95+062733.0	1.711	174	5.5	6.8	106	457.9	376.6	34.7	0
103039.88+285328.1	2.965	175	11.8	21.5	264	31.6	16.3	34.0	na
103256.84+262334.9	2.180	160	15.4	19.3	294	4.5	3.0	32.9	na
104740.47+020757.2	1.758	171	20.1	31.3	444	1.9	7.2	32.8	1
104801.18+193624.7	2.375	178	11.1	15.0	218	3.0	12.5	33.3	na
104932.92+640648.4	2.037	175	4.2	4.7	76	84.1	83.3	34.2	na
105720.43+641251.5	2.052	148	6.2	7.6	118	11.2	2.7	33.1	na
105855.54+364126.2	1.949	175	14.4	43.6	498	12.4	2.0	33.1	na
105951.90+405114.2	1.751	169	8.5	16.5	216	74.0	77.8	34.0	na
110709.50+054744.7	1.799	173	31.2	47.7	681	8.2	5.4	33.0	1
111217.48+614926.5	2.233	176	15.1	16.1	263	1.8	3.9	32.8	0
111239.39+432546.7	1.680	161	12.9	42.4	478	704.6	522.8	34.9	na
111928.37+130251.0	2.394	175	28.0	44.5	605	10.4	21.4	33.6	na
112506.96-001647.6	1.770	173	6.1	11.9	155	55.4	10.1	33.6	0
112714.00-011153.3	1.803	174	8.6	11.0	169	15.0	30.0	33.5	0
112828.63+313905.7	2.908	178	16.8	29.4	369	1.9	8.8	33.3	na
113250.84-002001.0	2.432	162	10.8	17.8	238	8.6	1.5	33.1	0
113325.14+551124.4	1.736	180	7.7	9.4	148	19.6	8.0	33.3	1
113442.06+411329.8	1.685	171	12.3	17.0	253	21.7	6.3	33.2	na
113701.18+293615.8	1.826	160	13.2	17.1	261	15.4	13.9	33.3	na
113703.08+014006.2	1.700	170	4.8	9.8	126	7.8	2.2	32.8	1
114312.04+535048.2	1.989	154	5.4	13.3	160	5.8	3.7	32.9	0
114327.55+300548.1	2.271	177	6.6	11.6	153	171.4	357.1	34.8	na
114533.75+385647.1	2.284	156	4.9	11.1	135	41.9	186.2	34.4	na
115848.59+134908.6	1.942	173	18.1	23.7	359	12.6	25.6	33.5	na
120003.89+410842.3	1.860	165	7.7	10.8	159	34.5	64.5	33.9	na
120055.99+115718.4	2.019	161	12.4	18.6	265	41.2	16.0	33.7	na
121701.37+101952.9	1.881	167	4.4	15.0	167	19.8	65.9	33.8	1
121952.54+465425.7	1.850	176	25.6	28.2	463	2.9	1.3	32.5	na
122649.77+190915.9	2.927	164	11.0	16.9	222	3.8	3.8	33.2	na
123036.15+065424.1	1.767	172	4.8	9.7	125	12.2	15.6	33.3	na
123052.56+393000.7	2.228	167	25.2	26.9	440	43.3	162.0	34.4	na
123106.80+475907.7	1.827	159	8.8	14.9	204	72.9	64.4	34.0	na

Table B.1—*Continued*

SDSS Name (SDSS J) (1)	z (2)	Φ (deg) (3)	D_1 (arcsec) (4)	D_2 (arcsec) (5)	L (kpc) (6)	S_1 (mJy) (7)	S_2 (mJy) (8)	$\log L_5$ (erg s ⁻¹ Hz ⁻¹) (9)	Ref. (10)
123155.99+334732.3	1.753	162	8.8	23.8	282	6.2	11.9	33.1	na
123403.95+141851.3	1.771	168	11.6	13.4	216	17.6	5.1	33.2	na
123740.56+361401.5	1.779	177	9.3	19.6	249	26.3	167.4	34.1	na
123818.95+081307.2	1.818	176	22.9	38.5	530	8.9	3.0	32.9	na
123954.15+373954.5	1.843	177	17.6	28.7	399	4.3	3.5	32.8	na
124000.93+034051.7	1.882	175	19.8	36.1	481	27.9	18.3	33.6	1
124157.54+633241.6	2.625	165	11.8	23.0	285	5.5	29.0	33.8	1
124758.52+625049.2	1.712	180	9.5	10.1	169	3.9	7.6	32.9	0
124918.41+281743.6	1.709	166	25.3	32.5	500	4.1	2.4	32.6	na
125320.41+463350.0	2.463	162	3.4	4.9	69	24.6	71.9	34.1	na
125503.87+480952.9	1.719	172	13.1	13.8	232	82.2	155.0	34.2	na
125508.09+622050.3	1.981	170	15.0	19.6	297	8.0	2.2	32.9	0
130248.13+393002.3	2.444	179	9.2	14.6	198	71.5	3.0	34.0	na
130508.36+140418.6	2.386	169	15.5	24.5	334	7.4	41.2	33.8	na
130637.16+172553.1	1.816	172	23.3	40.4	549	23.2	5.0	33.3	na
130828.73+502623.2	1.729	173	9.7	11.0	179	10.6	15.7	33.2	1
131040.74+020126.9	1.827	177	16.3	20.3	316	14.4	7.7	33.2	1
131053.25+170330.8	1.825	175	13.1	25.4	332	30.5	13.5	33.5	na
131056.77+175937.7	1.682	172	3.2	6.7	86	214.0	230.8	34.4	na
131130.18+311606.9	1.836	175	10.8	22.7	289	6.3	249.7	34.3	na
131458.40+560342.5	1.749	167	10.8	12.0	197	28.6	34.5	33.6	0
131536.75+191459.9	1.809	174	16.9	27.3	381	20.0	34.7	33.6	na
132053.63+103751.5	3.433	152	8.7	14.4	175	29.1	7.4	34.0	na
132150.05+073215.4	1.762	174	15.5	37.2	455	5.7	2.3	32.7	na
132418.14+463928.6	1.844	171	4.9	35.5	348	10.8	13.0	33.2	na
132607.15+475441.5	2.173	176	3.4	3.9	62	4.4	15.1	33.3	0
133227.95+213508.4	2.739	150	7.6	10.6	148	7.5	8.1	33.5	na
133259.16+490946.9	1.995	159	10.9	15.4	225	9.2	7.6	33.2	0
133350.44+312022.3	2.664	177	5.8	10.4	132	18.7	10.2	33.7	na
133802.80+423957.0	2.238	167	7.4	20.2	233	19.8	33.3	33.8	1
134048.37+433359.8	2.069	174	10.6	15.6	224	17.2	9.7	33.4	1
134820.88+302005.6	1.868	178	8.6	32.4	353	5.8	12.1	33.1	na
134958.17+281728.6	1.953	166	22.5	23.9	398	4.5	1.9	32.7	na
135031.51+164524.0	1.932	176	24.3	42.5	574	8.6	6.6	33.1	na
135703.83+023007.1	2.200	178	8.3	8.9	146	4.2	6.5	33.1	0
135823.50+602507.2	2.341	172	4.5	6.8	95	30.6	63.6	34.1	0
140130.68+415515.2	1.945	180	10.0	10.2	173	11.9	11.7	33.3	1
140148.64+071352.4	1.703	179	12.8	22.6	306	31.4	16.1	33.5	na
140654.32+224441.5	1.820	174	34.1	45.3	685	9.2	3.5	33.0	na
141030.99+614136.9	2.247	172	13.0	14.0	228	4.9	1.8	32.9	0
141123.51+004252.9	2.267	170	15.2	16.4	266	9.5	143.7	34.3	1
141151.97+550948.7	1.888	164	22.6	31.5	465	34.2	34.2	33.7	na
141532.19+404951.6	1.934	160	12.7	27.9	349	33.6	5.0	33.5	0
142033.25-003233.3	2.704	179	7.4	8.6	130	22.7	38.5	34.0	1
142108.55+111819.2	1.701	161	15.1	16.1	270	11.5	11.2	33.1	na
142745.71+550410.2	3.158	176	4.7	17.7	174	18.7	5.6	33.8	1

Table B.1—*Continued*

SDSS Name (SDSS J) (1)	z (2)	Φ (deg) (3)	D_1 (arcsec) (4)	D_2 (arcsec) (5)	L (kpc) (6)	S_1 (mJy) (7)	S_2 (mJy) (8)	$\log L_5$ (erg s ⁻¹ Hz ⁻¹) (9)	Ref. (10)
142958.10+290228.8	2.854	158	9.4	9.9	155	29.7	37.7	34.1	na
143331.87+190711.6	2.357	150	10.9	12.4	195	10.4	5.8	33.3	na
143513.49+610123.2	2.477	164	6.7	10.2	140	19.1	87.2	34.2	0
143826.57+464754.0	1.941	161	7.5	18.7	225	7.8	6.3	33.1	na
143932.67+455028.2	1.831	175	30.6	57.8	762	4.7	4.6	32.8	na
143939.94+442850.9	1.696	177	24.1	33.8	500	5.4	3.4	32.7	0
144030.18+160012.3	1.999	178	13.9	22.5	312	24.4	1.5	33.4	na
144707.40+520340.1	2.065	155	7.5	22.5	256	26.6	8.0	33.5	0
145049.93+000144.3	1.958	175	9.6	38.8	415	3.9	3.2	32.8	1
145051.37+121236.8	1.778	161	12.8	16.0	249	3.9	4.9	32.8	na
145240.91+430814.3	1.703	160	4.2	25.1	253	191.0	3.6	34.1	1
150649.28+304225.0	2.207	174	34.8	37.1	608	1.0	22.1	33.4	na
151503.21+613520.2	2.404	178	5.0	9.3	119	23.7	45.0	34.0	1
151609.98+010637.1	2.221	169	24.0	27.9	439	54.9	72.4	34.2	0
151745.77+435104.8	1.893	176	25.6	39.3	558	117.3	42.7	34.1	na
151912.81+374918.4	2.170	175	22.9	25.2	408	12.3	40.9	33.8	na
151915.77+141502.4	1.817	160	3.1	46.2	425	13.2	4.2	33.1	na
152143.53+051705.1	2.503	176	15.0	36.2	424	4.4	8.4	33.3	na
152145.61+143648.5	1.728	175	10.8	14.5	219	23.0	21.5	33.5	na
152325.20+270457.3	2.182	176	4.2	6.0	86	239.2	100.6	34.6	na
152505.36+530622.8	1.725	174	10.0	11.4	185	11.7	5.9	33.0	0
153753.72+085051.9	2.220	171	8.0	20.6	242	44.6	1.3	33.7	na
154015.12+211201.6	2.234	169	15.3	19.7	296	26.4	56.0	34.0	na
154106.73+245302.1	1.893	174	27.4	39.1	572	9.8	29.8	33.5	na
154316.52+413609.5	1.711	146	3.8	17.4	183	3.2	1.7	32.5	1
155002.00+365216.7	2.061	180	28.7	51.3	683	31.4	8.8	33.6	na
155407.74+010010.1	2.607	173	15.1	25.6	334	1.3	8.2	33.2	0
160415.02+463457.0	1.749	146	3.0	13.5	143	25.0	8.1	33.3	0
160815.94+510029.6	2.371	163	5.8	10.8	139	2.2	2.3	32.8	na
161022.15+103832.8	3.162	162	15.6	16.6	251	0.7	1.7	32.8	na
162246.26+290054.1	2.148	176	28.0	29.9	492	4.2	14.2	33.3	na
162334.40+083420.0	2.516	178	9.7	20.5	250	4.8	1.8	33.0	na
162336.45+341946.4	1.992	174	18.3	40.1	500	3.6	2.6	32.7	0
163039.12+630143.0	2.381	162	5.6	7.6	110	40.6	39.6	34.0	na
163234.65+245048.8	3.010	171	5.3	5.5	85	28.0	31.7	34.1	na
163640.55+464707.1	2.526	173	8.6	23.2	263	4.1	5.9	33.2	1
163815.90+275603.0	2.182	162	4.0	5.8	83	103.8	51.0	34.2	na
163955.00+310048.6	1.719	161	22.1	39.7	534	10.4	11.0	33.1	0
165022.92+242734.6	1.976	167	4.4	10.3	126	76.8	9.4	33.9	na
165559.40+404811.0	1.832	158	12.0	26.9	335	11.0	2.1	33.0	0
165820.35+373315.5	1.711	179	15.6	19.9	307	4.9	1.8	32.6	1
170220.06+591538.6	1.798	168	11.2	26.3	324	9.9	214.5	34.2	0
170651.42+381645.3	1.747	176	16.0	20.2	313	16.3	1.7	33.1	1
172158.60+554707.4	1.722	163	8.3	15.2	203	6.5	3.7	32.8	1
212800.10-004612.1	2.669	179	7.9	8.4	133	7.4	3.3	33.3	na
214432.75-075442.7	1.811	168	11.5	13.3	214	23.7	26.8	33.6	1

Table B.1—*Continued*

SDSS Name (SDSS J) (1)	z (2)	Φ (deg) (3)	D_1 (arcsec) (4)	D_2 (arcsec) (5)	L (kpc) (6)	S_1 (mJy) (7)	S_2 (mJy) (8)	$\log L_5$ ($\text{erg s}^{-1} \text{Hz}^{-1}$) (9)	Ref. (10)
232133.76–010645.9	1.974	161	7.1	8.2	131	19.7	16.1	33.5	1
233534.68–092739.2	1.813	172	20.8	57.5	675	7.3	11.2	33.1	1

Note. — Column 1: source name in SDSS DR7 Column 2: redshift. Column 3: opening angles of between pair of radio lobes. Column 4, 5: distance between optical quasars and radio lobes. Column 6: linear size, where $L = (D_1 + D_2)l$. Column 7, 8: flux densities of radio lobes at 1.4 GHz. Column 9: specific luminosity at 5 GHz assuming spectral index of $\alpha = -0.7$. Column 10: Appearance in de Vries et al. (2006): 1 = the source is identified as a FR II quasar. 0 = the source is not identified as a FR II quasar. na = the source is not appeared in SDSS DR3 and thus de Vries et al. (2006).

Radio Properties and Definition of BAL

C

C.1 Definition of BAL

As suggested in Hall et al. (2002), BI (Equation 2.2) can identify BAL objectively but a large number of (i) broad absorption features at lower outflow velocities, (ii) broad but shallow troughs, and (iii) high-velocity but narrow absorption troughs called "mini-BAL" are missed. In order to avoid this problem and select "true BAL" completely, they proposed AI (Equation 2.3). By definition, AI is less strict criterion than BI to judge whether absorption trough is BAL or not. In addition, Gibson et al. (2009) introduced BI_0 (Equation 2.4) which is stricter than AI but less strict than BI.

Knigge et al. (2008) reported that number distribution of AI is bimodal and sources having large AI are preferentially populated by BI based BAL quasars (but not completely). Thus, they concluded that fraction of BAL quasars estimated from AI-based sample is overestimated (see also Ganguly et al., 2007). AI based but not BI based BAL quasars could not be true BAL quasars. This is also implied by radio study. Shankar et al. (2008) reported that highest radio luminosities are preferentially found in AI- but not BI-based BAL quasars. These quasars might be a different class of quasars from the BI-based BAL quasars.

C.2 Radio Morphology and Definition of BAL

In Chapter 5, we constructed FR II quasars catalog at $1.68 \leq z \leq 4.93$ based on the statistical method introduced by de Vries et al. (2006). We compared fraction of BAL quasars in different quasars groups, and then confirmed that the fraction in FR II quasars is less than the other quasars groups. Now, as suggested by Shankar et al. (2008), radio properties could be related to the definitions of BAL. Here, we made cross identification using the FR II quasars catalog and presently published BAL quasars catalog from SDSS

Table C.1. Fraction of BAL quasars in SDSS DR7.

Quasar Group	Our identification		Shen et al.	
	BAL / all	fraction (%)	BAL / all	fraction (%)
Total quasars	7134 / 40972	17.4 ± 0.2	5148 / 41637	12.4 ± 0.2
...radio detected	570 / 3019	18.9 ± 0.7	396 / 3099	12.8 ± 0.6
.....FR II	12 / 186	6.5 ± 1.8	12 / 186	6.5 ± 1.8
.....without core	6 / 54	11.1 ± 4.3	6 / 54	11.1 ± 4.3
.....with core	6 / 132	4.6 ± 1.8	6 / 132	4.6 ± 1.8
.....non FR II with core	558 / 2833	19.7 ± 0.7	384 / 2913	13.2 ± 0.6
...not detected at radio	6564 / 37953	17.3 ± 0.2	4752 / 38538	12.3 ± 0.2

DR3 (Trump et al., 2006), DR5 (Gibson et al., 2009; Scaringi et al., 2009), DR6 (Allen et al., 2011), and DR7 (our identification in Chapter 5; Shen et al., 2011). Because these catalogs adopted different metrics to identify BAL, we can test the relation between radio morphology and the definitions of BAL

Table C.1 shows a comparison of the BAL fraction between our BAL identification and that of Shen et al. (2011). Here, "core" indicates a radio counter part detected by the FIRST survey (Becker et al., 1995) within 3 arcsec of optical position of a quasar. Though both identifications adopted BI_0 to identify BAL, there is a relatively large difference in the fraction between them. However, the rarity of FR-II BAL quasars is significant in both identifications. Table C.2–C.4 show the fraction of BAL estimated by using the literatures in the same manner. To identify BAL, Allen et al. (2011) and Gibson et al. (2009) adopted BI and BI_0 , respectively. Scaringi et al. (2009) used BI and their original learning algorithm. Trump et al. (2006) adopted AI and also calculated BI for all of the AI-selected sources. The rarity of the FR-II BAL quasars is confirmed in the BAL quasars catalog constructed by Allen et al. (2011), Gibson et al. (2009), and Scaringi et al. (2009). In contrast, the identification by Trump et al. (2006) shows different trend. While the BI selected BAL quasars show the rarity, AI but not BI selected sources do not. The result is similar with that in radio luminosity (Shankar et al., 2008). AI but not BI selected BAL quasars show different radio properties from the others both in luminosity and morphology. This implies that as suggested in Ganguly et al. (2007) and Knigge et al. (2008) AI could overestimate the presence of BAL.

Table C.2. Fraction of BAL quasars in SDSS DR6.

Quasar Group	Allen et al.	
	BAL / all	fraction (%)
Total quasars	3585/38399	9.3 ± 0.1
...radio detected	210/ 2659	7.9 ± 0.5
.....FR II	3/ 152	1.9 ± 1.1
.....without core	2/ 43	4.4 ± 3.1
.....with core	1/ 109	0.9 ± 0.9
.....non FR II with core	207/ 2507	8.3 ± 0.5
...not detected at radio	3375/35740	9.4 ± 0.2

Table C.3. Fraction of BAL quasars in SDSS DR5.

Quasar Group	Scaringi et al.		Gibson et al.	
	BAL / all	fraction (%)	BAL / all	fraction (%)
Total quasars	3543/28349	12.5 ± 0.2	3543/29724	11.9 ± 0.2
...radio detected	295/ 2131	13.8 ± 0.7	293/ 2208	13.3 ± 0.7
.....FR II	12/ 127	9.4 ± 2.6	5/ 133	3.7 ± 1.6
.....without core	6/ 38	15.4 ± 5.9	2/ 42	4.7 ± 3.2
.....with core	6/ 89	6.7 ± 2.7	3/ 91	3.3 ± 1.9
.....non FR II with core	283/ 2004	14.1 ± 0.8	288/ 2075	13.9 ± 0.8
...not detected at radio	3248/26218	12.4 ± 0.2	3250/27516	11.8 ± 0.2

Table C.4. Fraction of BAL quasars in SDSS DR3.

Quasar Group	Trump et al. (BI)		Trump et al. (AI but not BI)		Trump et al. (all AI)	
	BAL / all	fraction (%)	BAL / all	fraction (%)	BAL / all	fraction (%)
Total quasars	1794 /17562	10.2 ± 0.2	2691 /17562	15.3 ± 0.3	2691 /17562	15.3 ± 0.3
...radio detected	119 / 1347	8.8 ± 0.8	249 / 1347	18.5 ± 1.1	368 / 1347	27.3 ± 1.2
.....FR II	3 / 78	3.8 ± 2.2	14 / 78	17.7 ± 4.3	17 / 78	21.5 ± 4.7
.....without core	2 / 26	7.4 ± 5.1	5 / 26	18.5 ± 7.6	7 / 26	25.9 ± 8.6
.....with core	1 / 52	1.9 ± 1.9	9 / 52	17.3 ± 5.2	10 / 52	19.2 ± 5.5
.....non FR II with core	116 / 1269	9.1 ± 0.8	235 / 1269	18.5 ± 1.1	351 / 1269	27.7 ± 1.3
...not detected at radio	1675 /16215	10.3 ± 0.2	2442 /16215	15.1 ± 0.3	4117 /16215	25.4 ± 0.3

References

- Aaron, S. E. 1997, EVN Document No. 78
- Abazajian, K., et al. 2005, *AJ*, 129, 1755
- Abazajian, K. N., et al. 2009, *ApJS*, 182, 543
- Abramowicz, M. A., Czerny, B., Lasota, J. P., & Szuszkiewicz, E. 1988, *ApJ*, 332, 646
- Adelman-McCarthy, J. K., et al. 2007, *ApJS*, 172, 634
- Allen, J. T., Hewett, P. C., Maddox, N., Richards, G. T., & Belokurov, V. 2011, *MNRAS*, 410, 860
- Antonucci, R. 1993, *ARA&A*, 31, 473
- Antonucci, R. R. J., & Miller, J. S. 1985, *ApJ*, 297, 621
- Arshakian, T. G., & Longair, M. S. 2000, *MNRAS*, 311, 846
- Baars, J. W. M., Genzel, R., Pauliny-Toth, I. I. K., & Witzel, A. 1977, *A&A*, 61, 99
- Barthel, P. D. 1989, *ApJ*, 336, 606
- Becker, R. H., Gregg, M. D., Hook, I. M., McMahon, R. G., White, R. L., & Helfand, D. J. 1997, *ApJ*, 479, L93+
- Becker, R. H., White, R. L., Gregg, M. D., Brotherton, M. S., Laurent-Muehleisen, S. A., & Arav, N. 2000, *ApJ*, 538, 72
- Becker, R. H., White, R. L., & Helfand, D. J. 1995, *ApJ*, 450, 559
- Becker, R. H., et al. 2001, *ApJS*, 135, 227
- Begelman, M. C. 1996, *Baby Cygnus A's*, ed. Carilli, C. L. & Harris, D. E., 209–+
- Bicknell, G. V., Dopita, M. A., & O’Dea, C. P. O. 1997, *ApJ*, 485, 112
- Blandford, R. D., & Konigl, A. 1979, *ApJ*, 232, 34
- Blandford, R. D., & McKee, C. F. 1982, *ApJ*, 255, 419
- Blandford, R. D., & Rees, M. J. 1974, *MNRAS*, 169, 395
- Blanton, E. L., Gregg, M. D., Helfand, D. J., Becker, R. H., & Leighly, K. M. 2001, *AJ*, 121, 2915
- Blanton, E. L., Gregg, M. D., Helfand, D. J., Becker, R. H., & White, R. L. 2000, *ApJ*, 531, 118
- Borguet, B. C. J., Arav, N., Edmonds, D., Chamberlain, C., & Benn, C. 2013, *ApJ*, 762, 49

- Bridle, A. H., Hough, D. H., Lonsdale, C. J., Burns, J. O., & Laing, R. A. 1994, *AJ*, 108, 766
- Briggs, F. H., Turnshek, D. A., & Wolfe, A. M. 1984, *ApJ*, 287, 549
- Bruni, G., Dallacasa, D., Mack, K.-H., Montenegro-Montes, F. M., González-Serrano, J. I., Holt, J., & Jiménez-Luján, F. 2013, *A&A*, 554, A94
- Bruni, G., et al. 2012, *A&A*, 542, A13
- Cao Orjales, J. M., et al. 2012, *MNRAS*, 427, 1209
- Carilli, C. L., Perley, R. A., Dreher, J. W., & Leahy, J. P. 1991, *ApJ*, 383, 554
- Carvalho, J. C. 1985, *MNRAS*, 215, 463
- Chandra, P., Ray, A., & Bhatnagar, S. 2004, *ApJ*, 612, 974
- Ciotti, L., Ostriker, J. P., & Proga, D. 2009, *ApJ*, 699, 89
- Cohen, A. S., Lane, W. M., Cotton, W. D., Kassim, N. E., Lazio, T. J. W., Perley, R. A., Condon, J. J., & Erickson, W. C. 2007, *AJ*, 134, 1245
- Cohen, M. H., Ogle, P. M., Tran, H. D., Vermeulen, R. C., Miller, J. S., Goodrich, R. W., & Martel, A. R. 1995, *ApJ*, 448, L77+
- Condon, J. J., Cotton, W. D., Greisen, E. W., Yin, Q. F., Perley, R. A., Taylor, G. B., & Broderick, J. J. 1998, *AJ*, 115, 1693
- Conway, J. E. 2002, *NewAR*, 46, 263
- Croton, D. J., et al. 2006, *MNRAS*, 365, 11
- Czerny, B., Siemiginowska, A., Janiuk, A., Nikiel-Wroczyński, B., & Stawarz, L. 2009, *ApJ*, 698, 840
- Dallacasa, D., Orienti, M., Fanti, C., Fanti, R., & Stanghellini, C. 2013, *MNRAS*, 433, 147
- de Vries, W. H., Becker, R. H., & White, R. L. 2006, *AJ*, 131, 666
- DiPompeo, M. A., Brotherton, M. S., & De Breuck, C. 2012, *ApJ*, 752, 6
- DiPompeo, M. A., Brotherton, M. S., De Breuck, C., & Laurent-Muehleisen, S. 2011, *ApJ*, 743, 71
- Doeleman, S. S., et al. 2008, *Nature*, 455, 78
- Doi, A., et al. 2009, *PASJ*, 61, 1389
- Douglas, J. N., Bash, F. N., Bozyan, F. A., Torrence, G. W., & Wolfe, C. 1996, *AJ*, 111, 1945
- Dreher, J. W. 1981, *AJ*, 86, 833
- Drew, J. E., & Boksenberg, A. 1984, *MNRAS*, 211, 813
- Edwards, L. O. V., Fadda, D., & Frayer, D. T. 2010, *ApJ*, 724, L143
- Elvis, M. 2000, *ApJ*, 545, 63
- Fanaroff, B. L., & Riley, J. M. 1974, *MNRAS*, 167, 31P
- Fanti, C., Fanti, R., Dallacasa, D., Schilizzi, R. T., Spencer, R. E., & Stanghellini, C. 1995, *A&A*, 302, 317
- Fanti, C., Fanti, R., Parma, P., Schilizzi, R. T., & van Breugel, W. J. M. 1985, *A&A*, 143, 292
- Fanti, R., Fanti, C., Schilizzi, R. T., Spencer, R. E., Nan Rendong, Parma, P., van Breugel, W. J. M., & Venturi, T. 1990, *A&A*, 231, 333
- Fender, R. P., Belloni, T. M., & Gallo, E. 2004, *MNRAS*, 355, 1105
- Fender, R. P., Homan, J., & Belloni, T. M. 2009, *MNRAS*, 396, 1370

- Fine, S., Jarvis, M. J., & Mauch, T. 2011, *MNRAS*, 412, 213
- Fujisawa, K. 2008, in *The role of VLBI in the Golden Age for Radio Astronomy*
- Ganguly, R., Brotherton, M. S., Cales, S., Scoggins, B., Shang, Z., & Vestergaard, M. 2007, *ApJ*, 665, 990
- Gawronski, M. P., & Kunert-Bajraszewska, M. 2011, *ArXiv e-prints*
- Ghosh, K. K., & Punsly, B. 2007, *ApJ*, 661, L139
- Gibson, R. R., Brandt, W. N., Schneider, D. P., & Gallagher, S. C. 2008, *ApJ*, 675, 985
- Gibson, R. R., et al. 2009, *ApJ*, 692, 758
- Giovannini, G., Cotton, W. D., Feretti, L., Lara, L., & Venturi, T. 2001, *ApJ*, 552, 508
- Giovannini, G., Feretti, L., & Comoretto, G. 1990, *ApJ*, 358, 159
- Giovannini, G., Feretti, L., Gregorini, L., & Parma, P. 1988, *A&A*, 199, 73
- Goodrich, R. W., & Miller, J. S. 1995, *ApJ*, 448, L73+
- Gopal-Krishna, Patnaik, A. R., & Steppe, H. 1983, *A&A*, 123, 107
- Gregg, M. D., Becker, R. H., Brotherton, M. S., Laurent-Muehleisen, S. A., Lacy, M., & White, R. L. 2000, *ApJ*, 544, 142
- Gregg, M. D., Becker, R. H., & de Vries, W. 2006, *ApJ*, 641, 210
- Gregg, M. D., Becker, R. H., White, R. L., Helfand, D. J., McMahon, R. G., & Hook, I. M. 1996, *AJ*, 112, 407
- Greisen, E. W. 2003, *Information Handling in Astronomy - Historical Vistas*, 285, 109
- Gugliucci, N. E., Taylor, G. B., Peck, A. B., & Giroletti, M. 2005, *ApJ*, 622, 136
- Hall, P. B., et al. 2002, *ApJS*, 141, 267
- Hamilton, A. J. S., & Tegmark, M. 2004, *MNRAS*, 349, 115
- Hayashi, T. J., Doi, A., & Nagai, H. 2013, *ApJ*, 772, 4
- Hintzen, P., & Scott, J. S. 1978, *ApJ*, 224, L47
- Hovatta, T., Nieppola, E., Tornikoski, M., Valtaoja, E., Aller, M. F., & Aller, H. D. 2008, *A&A*, 485, 51
- Hovatta, T., Tornikoski, M., Lainela, M., Lehto, H. J., Valtaoja, E., Tornainen, I., Aller, M. F., & Aller, H. D. 2007, *A&A*, 469, 899
- Ichimaru, S. 1977, *ApJ*, 214, 840
- Jiang, D. R., & Wang, T. G. 2003, *A&A*, 397, L13
- Kameno, S., Horiuchi, S., Shen, Z., Inoue, M., Kobayashi, H., Hirabayashi, H., & Murata, Y. 2000, *PASJ*, 52, 209
- Kameno, S., Inoue, M., Wajima, K., Sawada-Satoh, S., & Shen, Z. 2003, *PASA*, 20, 213
- Kanekar, N., Lane, W. M., Momjian, E., Briggs, F. H., & Chengalur, J. N. 2009, *MNRAS*, 394, L61
- Kawaguchi, N. 2008, in *The role of VLBI in the Golden Age for Radio Astronomy*
- Kawakatu, N., Nagai, H., & Kino, M. 2008, *ApJ*, 687, 141
- King, A. 2003, *ApJ*, 596, L27
- Knigge, C., Scaringi, S., Goad, M. R., & Cottis, C. E. 2008, *MNRAS*, 386, 1426
- Komatsu, E., et al. 2011, *ApJS*, 192, 18
- Konar, C., Saikia, D. J., Jamrozy, M., & Machalski, J. 2006, *MNRAS*, 372, 693

- Korista, K. T., et al. 1995, *ApJS*, 97, 285
- Kunert-Bajraszewska, M., Janiuk, A., Gawroński, M. P., & Siemiginowska, A. 2010, *ApJ*, 718, 1345
- Laing, R. A. 1980, *MNRAS*, 193, 439
- Laor, A., & Brandt, W. N. 2002, *ApJ*, 569, 641
- Lavalley, M., Isobe, T., & Feigelson, E. 1992, in *Astronomical Society of the Pacific Conference Series*, Vol. 25, *Astronomical Data Analysis Software and Systems I*, ed. D. M. Worrall, C. Biemesderfer, & J. Barnes, 245
- Lípari, S. L., & Terlevich, R. J. 2006, *MNRAS*, 368, 1001
- Liu, Y., Jiang, D. R., Wang, T. G., & Xie, F. G. 2008, *MNRAS*, 391, 246
- Lynds, C. R. 1967, *ApJ*, 147, 396
- Maccarone, T. J., Gallo, E., & Fender, R. 2003, *MNRAS*, 345, L19
- Machalski, J., Koziel-Wierzbowska, D., Jamrozy, M., & Saikia, D. J. 2008, *ApJ*, 679, 149
- Magorrian, J., et al. 1998, *AJ*, 115, 2285
- Marecki, A., Thomasson, P., Mack, K.-H., & Kunert-Bajraszewska, M. 2006, *A&A*, 448, 479
- Massaro, F., Giroletti, M., Paggi, A., D’Abrusco, R., Tosti, G., & Funk, S. 2013, *ApJS*, 208, 15
- Mauch, T., Klöckner, H.-R., Rawlings, S., Jarvis, M., Hardcastle, M. J., Obreschkow, D., Saikia, D. J., & Thompson, M. A. 2013, *MNRAS*
- Mineshige, S., & Shields, G. A. 1990, *ApJ*, 351, 47
- Miyoshi, M., Moran, J., Herrnstein, J., Greenhill, L., Nakai, N., Diamond, P., & Inoue, M. 1995, *Nature*, 373, 127
- Montenegro-Montes, F. M., Mack, K., Vigotti, M., Benn, C. R., Carballo, R., González-Serrano, J. I., Holt, J., & Jiménez-Luján, F. 2008a, *MNRAS*, 388, 1853
- Montenegro-Montes, F. M., Mack, K. H., Benn, C. R., Carballo, R., Dallacasa, D., González-Serrano, J. I., Holt, J., & Jiménez-Luján, F. 2008b, in *The role of VLBI in the Golden Age for Radio Astronomy*
- Murgia, M., Fanti, C., Fanti, R., Gregorini, L., Klein, U., Mack, K.-H., & Vigotti, M. 1999, *A&A*, 345, 769
- Murray, N., Chiang, J., Grossman, S. A., & Voit, G. M. 1995, *ApJ*, 451, 498
- Nagai, H., Inoue, M., Asada, K., Kamenno, S., & Doi, A. 2006, *ApJ*, 648, 148
- Narayan, R., & Yi, I. 1994, *ApJ*, 428, L13
- Nomura, M., Ohsuga, K., Wada, K., Susa, H., & Misawa, T. 2013, *PASJ*, 65, 40
- O’Dea, C. P. 1998, *PASP*, 110, 493
- O’Dea, C. P., & Baum, S. A. 1997, *AJ*, 113, 148
- O’Dea, C. P., Baum, S. A., & Stanghellini, C. 1991, *ApJ*, 380, 66
- Ohsuga, K., & Mineshige, S. 2011, *ApJ*, 736, 2
- Ohsuga, K., Mineshige, S., Mori, M., & Kato, Y. 2009, *PASJ*, 61, L7+
- Orienti, M., & Dallacasa, D. 2008, *A&A*, 487, 885
- Orienti, M., Dallacasa, D., & Stanghellini, C. 2007, *A&A*, 475, 813
- Orienti, M., Murgia, M., & Dallacasa, D. 2010, *MNRAS*, 402, 1892
- Parma, P., Murgia, M., de Ruiter, H. R., Fanti, R., Mack, K.-H., & Govoni, F. 2007, *A&A*,

- 470, 875
- Pei, Y. C. 1992, *ApJ*, 395, 130
- Peterson, B. M. 1997, *An Introduction to Active Galactic Nuclei*, ed. Gómez de Castro, A. I. & Franqueira, M.
- Phillips, R. B., & Mutel, R. L. 1982, *A&A*, 106, 21
- Priddey, R. S., Gallagher, S. C., Isaak, K. G., Sharp, R. G., McMahon, R. G., & Butner, H. M. 2007, *MNRAS*, 374, 867
- Proga, D., Stone, J. M., & Drew, J. E. 1998, *MNRAS*, 295, 595
- Proga, D., Stone, J. M., & Kallman, T. R. 2000, *ApJ*, 543, 686
- Punsly, B., & Zhang, S. 2010, *ApJ*, 725, 1928
- Readhead, A. C. S. 1995, *Proceedings of the National Academy of Science*, 92, 11447
- Readhead, A. C. S., Taylor, G. B., Xu, W., Pearson, T. J., Wilkinson, P. N., & Polatidis, A. G. 1996, *ApJ*, 460, 612
- Reichard, T. A., et al. 2003, *AJ*, 125, 1711
- Rengelink, R. B., Tang, Y., de Bruyn, A. G., Miley, G. K., Bremer, M. N., Roettgering, H. J. A., & Bremer, M. A. R. 1997, *A&AS*, 124, 259
- Reynolds, C., Punsly, B., Kharb, P., O'Dea, C. P., & Wrobel, J. 2009, *ApJ*, 706, 851
- Reynolds, C. S., & Begelman, M. C. 1997, *ApJ*, 487, L135
- Roberts, D. H., Wardle, J. F. C., & Brown, L. F. 1994, *ApJ*, 427, 718
- Rybicki, G. B., & Lightman, A. P. 1979, *Radiative processes in astrophysics*, ed. Rybicki, G. B. & Lightman, A. P.
- Saikia, D. J., Jeyakumar, S., Mantovani, F., Salter, C. J., Spencer, R. E., Thomasson, P., & Wiita, P. J. 2003, *PASA*, 20, 50
- Scaringi, S., Cottis, C. E., Knigge, C., & Goad, M. R. 2009, *MNRAS*, 399, 2231
- Scheuer, P. A. G. 1974, *MNRAS*, 166, 513
- Schlegel, D. J., Finkbeiner, D. P., & Davis, M. 1998, *ApJ*, 500, 525
- Schneider, D. P., et al. 2007, *AJ*, 134, 102
- . 2010, *AJ*, 139, 2360
- Schoenmakers, A. P., de Bruyn, A. G., Röttgering, H. J. A., van der Laan, H., & Kaiser, C. R. 2000, *MNRAS*, 315, 371
- Shakura, N. I., & Sunyaev, R. A. 1973, *A&A*, 24, 337
- Shankar, F., Dai, X., & Sivakoff, G. R. 2008, *ApJ*, 687, 859
- Shen, Y., Strauss, M. A., Hall, P. B., Schneider, D. P., York, D. G., & Bahcall, N. A. 2008, *ApJ*, 677, 858
- Shen, Y., et al. 2011, *ApJS*, 194, 45
- Shepherd, M. C. 1997, in *Astronomical Society of the Pacific Conference Series*, Vol. 125, *Astronomical Data Analysis Software and Systems VI*, ed. G. Hunt & H. Payne, 77–+
- Shlosman, I., Vitello, P. A., & Shaviv, G. 1985, *ApJ*, 294, 96
- Snellen, I. A. G., Schilizzi, R. T., Miley, G. K., de Bruyn, A. G., Bremer, M. N., & Röttgering, H. J. A. 2000, *MNRAS*, 319, 445
- Spergel, D. N., et al. 2003, *ApJS*, 148, 175
- Spoelstra, T. A. T., Patnaik, A. R., & Gopal-Krishna. 1985, *A&A*, 152, 38

- Sramek, R. A., & Weedman, D. W. 1980, *ApJ*, 238, 435
- Stanghellini, C., O'Dea, C. P., Dallacasa, D., Cassaro, P., Baum, S. A., Fanti, R., & Fanti, C. 2005, *A&A*, 443, 891
- Stoche, J. T., Morris, S. L., Weymann, R. J., & Foltz, C. B. 1992, *ApJ*, 396, 487
- Tinti, S., Dallacasa, D., de Zotti, G., Celotti, A., & Stanghellini, C. 2005, *A&A*, 432, 31
- Tombesi, F., Cappi, M., Reeves, J. N., Nemmen, R. S., Braito, V., Gaspari, M., & Reynolds, C. S. 2013, *MNRAS*, 430, 1102
- Tombesi, F., Cappi, M., Reeves, J. N., Palumbo, G. G. C., Braito, V., & Dadina, M. 2011, *ApJ*, 742, 44
- Tombesi, F., Cappi, M., Reeves, J. N., Palumbo, G. G. C., Yaqoob, T., Braito, V., & Dadina, M. 2010a, *A&A*, 521, A57
- Tombesi, F., Sambruna, R. M., Reeves, J. N., Braito, V., Ballo, L., Gofford, J., Cappi, M., & Mushotzky, R. F. 2010b, *ApJ*, 719, 700
- Torniainen, I., Tornikoski, M., Lähteenmäki, A., Aller, M. F., Aller, H. D., & Mingaliyev, M. G. 2007, *A&A*, 469, 451
- Torniainen, I., Tornikoski, M., Teräsraanta, H., Aller, M. F., & Aller, H. D. 2005, *A&A*, 435, 839
- Trump, J. R., et al. 2006, *ApJS*, 165, 1
- Tsien, S. C. 1982, *MNRAS*, 200, 377
- Tzioumis, A. K., et al. 1989, *AJ*, 98, 36
- Urry, C. M., & Padovani, P. 1995, *PASP*, 107, 803
- van Breugel, W., Miley, G., & Heckman, T. 1984, *AJ*, 89, 5
- Vitello, P. A. J., & Shlosman, I. 1988, *ApJ*, 327, 680
- Voit, G. M., Weymann, R. J., & Korista, K. T. 1993, *ApJ*, 413, 95
- Weymann, R. J., Morris, S. L., Foltz, C. B., & Hewett, P. C. 1991, *ApJ*, 373, 23
- Wilkinson, P. N., Polatidis, A. G., Readhead, A. C. S., Xu, W., & Pearson, T. J. 1994, *ApJ*, 432, L87
- Willott, C. J., Rawlings, S., Archibald, E. N., & Dunlop, J. S. 2002, *MNRAS*, 331, 435
- Willott, C. J., Rawlings, S., & Grimes, J. A. 2003, *ApJ*, 598, 909
- Yang, J., Wu, F., Paragi, Z., & An, T. 2012, *MNRAS*, 419, L74
- York, D. G., et al. 2000, *AJ*, 120, 1579
- Zhou, H., Wang, T., Wang, H., Wang, J., Yuan, W., & Lu, Y. 2006, *ApJ*, 639, 716

Correspondence

Takayuki HAYASHI

Mizusawa VLBI Observatory, National Astronomical Observatory of Japan
2-21-1 Osawa, Mitaka, Tokyo 181-8588
e-mail: t.hayashi@nao.ac.jp